



UNIVERSITÀ
DEGLI STUDI
FIRENZE

SCUOLA DI SCIENZE MATEMATICHE,
FISICHE E NATURALI

CORSO DI LAUREA MAGISTRALE
IN FISICA

Studio sperimentale di nanocristalli
di perovskite $CsPbBr_3$ come emetti-
tori di fotoni singoli

Experimental study of $CsPbBr_3$
perovskite nanocrystals as single photon
emitters

Candidate

Marianna D'Amato (ID number 6039112)

Thesis Advisor

Prof. Alberto Bramati

Academic Year 2019/2020

Studio sperimentale di nanocristalli di perovskite $CsPbBr_3$ come emettitori di fotoni singoli

Tesi di Laurea Magistrale. University of Florence

© 2020 Marianna D'Amato. All rights reserved

This thesis has been typeset by L^AT_EX and the UniFiTh class.

Version: 31/08/2020

Author's email: marianna.damato@stud.unifi.it

Contents

Introduction	v
1 Single photon sources based on single nanoemitters	1
1.1 A toolbox for single-mode quantum optics	1
1.2 How to generate single photons beams	4
1.3 Statistical classification of sources	5
1.4 The second order autocorrelation function	6
1.5 The Hanbury-Brown and Twiss (HBT) interferometer	8
1.6 The ideal single-photon source	9
1.7 Blinking and bleaching	10
1.8 Main single photon sources	11
2 CsPbX₃ perovskites	15
2.1 Chemical composition and structural landscapes	15
2.2 Electronic and optical properties	19
2.3 <i>CsBrX₃</i> perovskites as single photon emitter: the state of the art	22
2.4 Synthesis, main issues and surface passivation approaches	22
3 Experimental setup and methods	25
3.1 Standard fluorescence microscopy techniques	25
3.2 Polarization microscopy	29
3.3 Photoluminescence as a function of the excitation power	32
3.4 Time-correlated single photon counting technique	35
3.5 Noise sources and noise cleaning on $g^2(\tau)$ measurements	37
3.6 Synthesis and deposition methods	37
4 Experimental study of <i>CsPbBr₃</i> nanocrystals	43
4.1 Emission spectra	43
4.2 Saturation measurement	45
4.3 Effect of the sample dilution on the photobleaching	46
4.4 Blinking characterization	49
4.5 Polarization measurement	57
4.6 Quantum properties	58

5	Nanofiber integration	61
5.1	Optical nanofibers	61
5.2	Light propagation in an optical fiber	62
5.2.1	Nanofiber electromagnetic modes	62
5.2.2	Electric field of the HE_{11} mode	66
5.2.3	Longitudinal component of the fundamental mode	66
5.2.4	Choice of the nanofiber's diameter	68
5.3	Producing optical nanofibers	69
5.4	Deposition technique	71
5.5	Antibunching measurement	71
A	Noise cleaning of the second order autocorrelation function	77
B	Synthesis recipe	79

Introduction

Over the last two decades, the generation of single photons on demand has become a field of huge interest for potential applications. A major driver of the current research into single-photon sources is the significant advance in quantum-information science [1], including quantum communication [2] [3] [4] and cryptography [5] [6] [7], quantum simulation and computing [8] [9] and quantum metrology [10] [11]. Quantum communication is focused on the transfer of the quantum information and involves the generation and the use of quantum states for communication protocols, proposing new techniques for secure communication. The most important examples are the protocols built on quantum random number generators (QRNG) for secret keys and Quantum Key Distribution (QKD), which has already reached commercial availability and offers a way to exchange cryptographic keys with absolute protection from eavesdroppers. In quantum simulation well-controlled quantum systems allow to reproduce the evolution of other less accessible systems and quantum communication employs quantum effect to enormously speed up certain calculations, solving hard problems for classical computation. Furthermore, quantum metrology aims at using quantum resources, like non-classical correlations of different quantum states, to beat the classic limit of precision measurement.

Single photons soon proved to be interesting qubits for such applications, that cannot be achieved with classical light. They have different degrees of freedom into which the information can be encoded, they can be easily manipulated and detected and they are also highly immune to external disturbances: these properties make them an interesting option as flying qubits for long distance quantum information transfer [12].

An ideal single photon source would be one for which: a single photon can be emitted on demand, the probability of emitting a single photon is 100% and the probability of multiple photon emission is 0%, subsequent emitted photons are indistinguishable and the repetition rate is arbitrarily fast. However, deviations from these characteristics are always present in real-world sources. There are different systems that have been investigated for use as on-demand sources of single photons, such as single atoms [13] [14] [15], single ions [16] [17] [18], single molecules [19] [20] [21], color centers [22] [23] [24] and semiconductors quantum dots [25] [26] [27] [28].

In the last few years the interest in perovskite nanocrystals - originally studied for solar-cell application - is rapidly raising in the quantum optics community. It has been demonstrated that quantum confined perovskite nanocrystals can behave as

very efficient single photon emitters at low and room temperature, as indicated by a strong antibunching detected in photoluminescence measurements [29]. This observation is explained by the presence of fast non radiative Auger recombination which suppresses emission from biexcitons and other higher-order multiexcitons. Moreover, perovskite nanocrystals are versatile emitters for the possibility to tune their emission wavelength playing on their size and composition[30]. In addition to this, they are easily synthesized by low-cost, well mastered wet chemistry techniques, unlike other single photon sources - as single defects in nanodiamond and epitaxial quantum dots - which require heavy fabrication facilities. Despite these interesting features, their use is limited by different instabilities as they usually bleach after few minutes under illumination and present fluctuations (blinking) on the photoluminescence intensity. Overcoming these instabilities is a key challenge for the future development of this material.

In this thesis I will present a full analysis of the optical and quantum properties of highly efficient $CsPbBr_3$ perovskite nanocubes which exhibit reduced blinking together with a strong photon antibunching of the emission. These nanocubes are synthesized in collaboration with the Institute des Nanoscience de Paris (INSP) with a method, used for the first time for this purpose, that allows us to obtain higher stable samples which can be excited under optical excitation for more than one hour. Finally, for the first time with such kind of emitters, we achieve the coupling of a single perovskite nanocrystals with a tapered optical nanofiber. As shown in the case of atoms[31] [32] and solid state emitters[33] [34] [35], this technique is of considerable importance for quantum technology's applications and it is a promising step towards the realization of a compact, integrated, single photon source.

The experiments presented in this thesis have been carried out at the Laboratoire Kastler Brossel (LKB) of the Sorbonne Université of Paris. I would like to thank Prof. Francesco Marin for encouraging this experience abroad and Prof. Alberto Bramati and all the members of the Quantum Optics group - in particular Stefano Pierini - for having guided every step of my work with great attention and enthusiasm.

This manuscript is organized as follow.

The **first chapter** reviews the theoretical background for the study of a single photon source, introducing the key factors to understand their physics and performance and concluding with a brief overview of the state of art of single photon sources. In the **second chapter** I will explain the main structural and optical characteristics of cesium lead halide perovskites, giving space to the main synthesis techniques and finally focusing on the state of the art of these perovskite nanocrystals as single photon emitters. In the **third chapter** I will detail the experimental setup, the information we can acquire from the different measurements together with the method to process the data. The **fourth chapter** will be devoted to the experimental characterization of the $CsPbBr_3$ nanocrystals, presenting a full analysis of their optical and quantum properties. Finally, the **fifth chapter** will describe the coupling of a $CsPbBr_3$ nanocube with a sub-wavelength optical nanofiber. I will explain the properties of the light that nanofibers can guide, the fabrication method and the results of the performed antibunching measurements .

Chapter 1

Single photon sources based on single nanoemitters

The idea of manipulating single photons required a long gestation process which began in 1900 when Planck introduced the quantization of the electromagnetic energy to explain the spectrum of black-body radiation. Five years later, in 1905, Einstein used the concept of photons to explain the photoelectric effect. However, in this new semi-classical frame where matter is quantized, light remains a classical wave. Only after a few decades researchers began to look for specific quantum properties of light that could not be understood in a classical frame. The Hanbury-Brown and Twiss interferometry experiment in 1956 to study the coherence properties of light and the discovery of the laser in the 1960s fueled this interest. A deep analysis of the quantum properties of light and a reformulation of the theoretical framework started at this period [36].

1.1 A toolbox for single-mode quantum optics

A mode of the electromagnetic field in a cubic region of space of side L can be directly quantized, with a procedure analogue to that used for a harmonic oscillator: it is possible to define the operators $\hat{a}_{\vec{k},\vec{\epsilon}}$ and $\hat{a}_{\vec{k},\vec{\epsilon}}^\dagger$ that respectively annihilate and create one photon of energy $\hbar\omega_{\vec{k}}$ in the electromagnetic field's mode characterized by a wave vector \vec{k} and a polarization $\vec{\epsilon}$ perpendicular to \vec{k} :

$$\begin{aligned}\hat{a}_{\vec{k},\vec{\epsilon}}|n_{\vec{k},\vec{\epsilon}}\rangle &= \sqrt{n_{\vec{k},\vec{\epsilon}}}|n_{\vec{k},\vec{\epsilon}}-1\rangle \\ \hat{a}_{\vec{k},\vec{\epsilon}}^\dagger|n_{\vec{k},\vec{\epsilon}}\rangle &= \sqrt{n_{\vec{k},\vec{\epsilon}}+1}|n_{\vec{k},\vec{\epsilon}}+1\rangle\end{aligned}\tag{1.1}$$

The eigenstate $|n\rangle_{\vec{k},\vec{\epsilon}}$ relative to the number operator $\hat{n}_{\vec{k},\vec{\epsilon}} = \hat{a}_{\vec{k},\vec{\epsilon}}^\dagger \hat{a}_{\vec{k},\vec{\epsilon}}$, whose eigenvalue counts the number of excitations in the selected mode, is called *photon-number state* or *Fock state*. The single photon state, characterized by the presence of a single excitation in the selected mode, is described by the state $|n\rangle_{\vec{k},\vec{\epsilon}} = |1\rangle$.

In the Heisenberg representation, the electric field operator at position \vec{r} could

be written as the sum of two contributions:

$$\hat{E}(\vec{r}, t) = \hat{E}^+(\vec{r}, t) + \hat{E}^-(\vec{r}, t) \quad (1.2)$$

where

$$\begin{aligned} \hat{E}^+(\vec{r}, t) &= \sum_{\vec{k}} \sum_{\vec{\epsilon}} \vec{e}_{\vec{k}\vec{\epsilon}} \sqrt{\frac{\hbar\omega_{\vec{k}}}{2\epsilon_0 V}} \hat{a}_{\vec{k}\vec{\epsilon}} e^{-i\chi_{\vec{k}}(\vec{r}, t)} \\ \hat{E}^-(\vec{r}, t) &= \sum_{\vec{k}} \sum_{\vec{\epsilon}} \vec{e}_{\vec{k}\vec{\epsilon}} \sqrt{\frac{\hbar\omega_{\vec{k}}}{2\epsilon_0 V}} \hat{a}_{\vec{k}\vec{\epsilon}}^\dagger e^{i\chi_{\vec{k}}(\vec{r}, t)} \end{aligned} \quad (1.3)$$

are the *positive and negative frequency parts* of the electric field operator and $\chi_{\vec{k}}(\vec{r}, t)$ is a phase term defined as

$$\chi_{\vec{k}}(\vec{r}, t) = \omega_{\vec{k}} t - \vec{k} \cdot \vec{r} - \frac{\pi}{2} \quad (1.4)$$

As in the case of the harmonic oscillator, $\hat{a}_{\vec{k},\vec{\epsilon}}$ and $\hat{a}_{\vec{k},\vec{\epsilon}}^\dagger$ are not Hermitian operators and they cannot represent observables, according to the general principles of quantum mechanics, even if they have simple properties and are extremely useful in calculations. It is sometimes more convenient to work with the quadrature operators defined by:

$$\hat{X} = \frac{1}{2}(\hat{a}^\dagger + \hat{a}) \quad \hat{Y} = \frac{1}{2}i(\hat{a}^\dagger - \hat{a}) \quad (1.5)$$

that satisfy the Hermitian operator condition¹[36].

The field can be expressed in terms of the two quadrature operators and the equation 1.3 can be further simplified removing the square-root factor²:

$$\hat{E} = \hat{E}^+(\chi) + \hat{E}^-(\chi) = \hat{X} \cos \chi + \hat{Y} \sin \chi \quad (1.6)$$

It can be observed that the number state $|n\rangle$ is a state of well-defined energy but not with a well-defined electric field [37].

In fact the average field is zero as can be observed from:

$$\langle n | \hat{X} | n \rangle = 0 = \langle n | \hat{Y} | n \rangle \quad (1.7)$$

but the mean of the square of this field is not zero and for both quadratures it is easy to derive that:

$$\langle n | \hat{X}^2 | n \rangle = \frac{1}{2}(n + \frac{1}{2}) = \langle n | \hat{Y}^2 | n \rangle \quad (1.8)$$

The variances of the quadrature operators are defined by:

$$(\Delta X)^2 = \langle \hat{X}^2 \rangle - \langle \hat{X} \rangle^2 \quad (\Delta Y)^2 = \langle \hat{Y}^2 \rangle - \langle \hat{Y} \rangle^2 \quad (1.9)$$

¹Being schematized by a harmonic oscillator, an electromagnetic mode can be described by a pair of conjugate non-commuting operators similarly to position and momentum for a one-dimensional particle. In a classical wave representation, these complementary operators can be chosen as amplitude and phase. Heisenberg's uncertainty principle requires that the fluctuations on these conjugate variables cannot both be arbitrarily small.

²The convention is that the electric field is measured in units of $2\sqrt{\frac{\hbar\omega_{\vec{k}}}{2\epsilon_0 V}}$.

The variances obtained for the number states are therefore:

$$(\Delta X)^2 = \frac{1}{2}(n + \frac{1}{2}) = (\Delta Y)^2 \quad (1.10)$$

In particular, this uncertainty is minimized in the case of vacuum state ($n = 0$):

$$(\Delta X)_{vac}^2 = \frac{1}{4} = (\Delta Y)_{vac}^2 \quad (1.11)$$

However a state with n photons cannot describe an electromagnetic wave, since the *measurable* electric and magnetic fields have a non-zero expectation value. In order to satisfy this request, we introduce the *coherent states*[38] [39] $|\alpha\rangle$ which can be written in the basis of Fock States according to:

$$|\alpha\rangle = \exp(-|\alpha|^2/2) \sum_{n=0}^{\infty} \frac{\alpha^n}{(n!)^{1/2}} |n\rangle \quad (1.12)$$

In particular $|\alpha\rangle$ is eigenstate of the annihilation operator \hat{a} with eigenvalue α , such that

$$\hat{a} |\alpha\rangle = \alpha |\alpha\rangle \quad (1.13)$$

The property 1.13 allows us to find out the expectation value of the number operator and the variance of photon number when the system is described by a coherent state, respectively:

$$\begin{aligned} \langle n \rangle &= |\alpha|^2 \\ (\Delta n)^2 &= \langle n^2 \rangle - \langle n \rangle^2 = \langle n \rangle \end{aligned} \quad (1.14)$$

From 1.14 it is possible to deduce that the number of photons follows a Poisson distribution. The probability of finding n photons in the mode considered is given by:

$$P(n) = |\langle n|\alpha\rangle|^2 = \exp(-|\alpha|^2) \frac{|\alpha|^{2n}}{n!} \quad (1.15)$$

Using the property 1.13 it is also possible to obtain the coherent-state expectation value of the quadrature operators:

$$\langle \alpha | \hat{X} | \alpha \rangle = \frac{1}{2} \langle \alpha | (\hat{a}^\dagger + \hat{a}) | \alpha \rangle = \frac{1}{2}(\alpha^* + \alpha) = \text{Re}(\alpha) = |\alpha| \cos \theta \quad (1.16)$$

and in a similar way

$$\langle \alpha | \hat{Y} | \alpha \rangle = \text{Im}(\alpha) = |\alpha| \sin \theta \quad (1.17)$$

where we have put $\alpha = |\alpha|e^{i\theta}$. After calculating the expectation values of the squares of the quadrature operators, it is possible to derive the quadrature variances:

$$(\Delta \hat{X})^2 = \frac{1}{4} = (\Delta \hat{Y})^2 \quad (1.18)$$

Thus the coherent state is a near-classical state because it not only yields from eq. 1.16 and 1.17 the correct form for the field expectation values but contains only

the noise of the vacuum in eq. 1.11. However, in spite of these properties, they are still quantum states [37]. In principle, it is possible to generate states in which fluctuations (i.e. photon number fluctuations) are reduced below the coherent state condition 1.18 in one quadrature component. Of course, the fluctuations in the other quadrature must be enhanced (i.e phase noise), such that the Heisenberg uncertainty principle is not violated. Such states of the radiation are called *squeezed states* and they have attractive applications in optical communication, photon detection technique and gravitational wave detection[40].

1.2 How to generate single photons beams

The simplest way to approximate single photon Fock states is to attenuate a pulsed laser beam. For a laser beam with an average intensity of μ photons, the probability of having n photons for each pulse is given by:

$$p(n, \mu) = \frac{\mu^n e^{-\mu}}{n!} \quad (1.19)$$

and the probability that weak coherent pulses contain more than one photon is given by [5]:

$$P_{1+} = P(n > 1 | n > 0, \mu) = \frac{1 - P(0, \mu) - P(1, \mu)}{1 - P(0, \mu)} = \frac{1 - e^{-\mu}(1 + \mu)}{1 - e^{-\mu}} \simeq \frac{\mu}{2} \quad (1.20)$$

This probability can be made arbitrary small by reducing the mean number of photons in each laser pulse, but choosing $\mu \rightarrow 0$ increases the probability that a pulse does not contain any photon at all. Although these *faint laser* are much easier to built and operate than single photon sources and are used in some quantum cryptography applications [41], they do not allow to obtain an effective single photon generation. In fact, faint laser pulses deliver Poisson distributions of photons, from which multi-photon events can never be entirely suppressed even for very weak pulses [42].

An efficient way to generate a single photon flux consists in using the fluorescence between two energy levels of a *quantum emitter*. In general, an emitter has a complex scheme of energy levels; by using a monochromatic laser radiation, at resonance with only one of the system's optical transitions, it is possible to couple two levels according to the electric dipole selection's rules. The remaining levels can be neglected because, far from the resonance condition, they interact only weakly with the light. Such two-levels system, as showed in figure 1.1, is initially in its ground state $|0\rangle$ and it can be excited in the state $|1\rangle$; it remains in such state up to the spontaneous relaxation toward the state $|0\rangle$, resulting in the emission of a photon. Let us make some hypotheses:

- the duration of the excitation pulse is shorter than the lifetime of the excited level τ_{10} in order to avoid more than one absorption-emission cycle;
- the period of the laser pulses is longer than τ_{10} ;
- the excitation pulse intensity is high enough to stimulate the transition $|0\rangle \rightarrow |1\rangle$;

- the spontaneous relaxation $|1\rangle \rightarrow |0\rangle$ is purely radiative.

In this way is not possible to have the emission of more than one photon and the probability in equation 1.20 goes to zero [43].

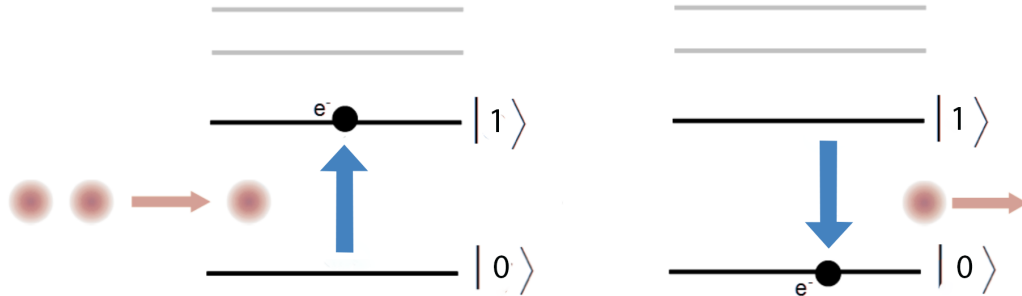


Figure 1.1. Scheme of a quantum emitter excited by a resonant monochromatic radiation with the electronic transition $|0\rangle \rightarrow |1\rangle$.

1.3 Statistical classification of sources

As seen, the statistical properties of coherent light are described by a Poisson distribution with photon number fluctuations given by $\Delta n = \sqrt{\langle n \rangle}$. This property provides a benchmark for classifying other types of light according to the standard deviation of their photon number distributions [44]. In general, we can distinguish the three following cases, illustrated in table 1.1.

Table 1.1. Classification of light according to the photon statistics.

Photon statistics	Δn	Classical equivalents
Super-Poissonian	$> \sqrt{\langle n \rangle}$	Thermal light, chaotic light
Poissonian	$\sqrt{\langle n \rangle}$	Coherent light
Sub-Poissonian	$< \sqrt{\langle n \rangle}$	None

Super-Poissonian and sub-Poissonian light distributions are, respectively, broader and narrower than Poissonian distribution, as showed in figure 1.2.

Super-Poissonian statistic characterizes all classical light beams with time-varying light intensities, like thermal light from a black-body source or partially coherent light from a discharge lamp. For example, thermal light's statistic follows the Planck distribution characteristic of the black-body radiation at the thermodynamic equilibrium:

$$P_{th} = \frac{\langle n \rangle^n}{(1 + \langle n \rangle)^{n+1}} \quad (1.21)$$

whose variance is given by $(\Delta n)^2 = \langle n \rangle + \langle n \rangle^2$ ³.

³The average value of photons per mode is given by Planck's formula: $\langle n \rangle = \frac{1}{\exp(\hbar\omega/k_bT) - 1}$.

Sub-Poissonian light, instead, has no classical counterpart. Therefore, the observation of sub-Poissonian statistics is a clear signature of the quantum nature of light. Thus, since $\Delta n = 0$ for Fock's states, these are the purest form sub-poissonian light. As we will see, a single-photon source can match this distribution by delivering single photons at regular time intervals.

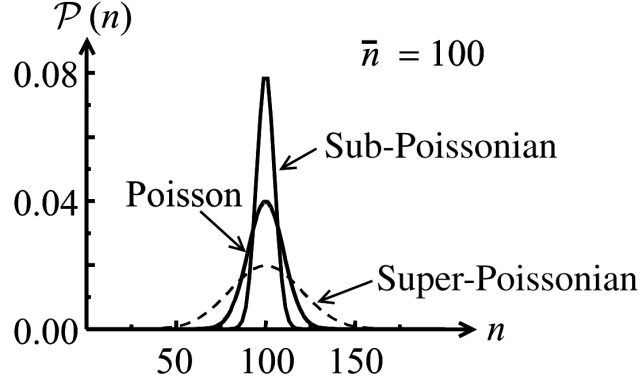


Figure 1.2. Photon statistics comparison for light with Poisson, sub-Poissonian and super-Poissonian distribution, with the same mean photon number. Picture taken from reference [44].

1.4 The second order autocorrelation function

In section 1.3 we have seen how light beams can be classified according to their photon statistics, now we shall look at a different way of quantifying light monitoring the photons detected at two different time instants t and $t + \tau$. Let us consider the three following functions of time [42]:

(I) the *instantaneous intensity*:

$$I(t) = 2\epsilon_0 c \langle E^-(t)E^+(t) \rangle \quad (1.22)$$

(II) the *first-order correlation function*:

$$g^{(1)}(\tau) = \frac{\langle E^-(t+\tau)E^+(t) \rangle}{\langle E^-(t)E^+(t) \rangle} \quad (1.23)$$

where the average is supposed to be taken over a stationary state of light;

(III) the *second-order correlation function*, classically written as:

$$g^{(2)}(\tau) = \frac{\langle I(t+\tau)I(t) \rangle}{\langle I(t) \rangle^2} \quad (1.24)$$

with the quantum-mechanical expression:

$$g^{(2)}(\tau) = \frac{\langle E^-(t)E^-(t+\tau)E^+(t+\tau)E^+(t) \rangle}{\langle E^-(t)E^+(t) \rangle^2} \quad (1.25)$$

Rewriting 1.25 for a single mode of the field, as seen in section 1.1, and for $\tau = 0$ we have:

$$g^{(2)}(0) = \frac{\langle \hat{a}^\dagger \hat{a}^\dagger \hat{a} \hat{a} \rangle}{\langle \hat{a}^\dagger \hat{a} \rangle^2} = \frac{\langle n(n-1) \rangle}{\langle n \rangle^2} = \frac{\langle n^2 \rangle - \langle n \rangle}{\langle n \rangle^2} = 1 + \frac{(\Delta n)^2 - \langle n \rangle}{\langle n \rangle^2} \quad (1.26)$$

The quantity in eq 1.26, called *second-order autocorrelation function*, allows thus a threefold classification linked with the statistics seen in section 1.3:

- **Bunched light:** $g^{(2)}(0) > 1$
 There is a bigger probability of detecting a second photon at shorter time intervals, rather than at larger delays. This is the case of super-Poissonian sources like black-body radiation.
- **Coherent light:** $g^{(2)}(0) = 1$
 The probability of detecting two photons is the same for any time interval τ , resulting in random time intervals between two photons. The statistic is Poissonian.
- **Antibunched light:** $g^{(2)}(0) < 1$
 The probability of detecting a second photon is negligible for small time intervals, but increases with τ ; this case corresponds to a sub-Poissonian statistics.

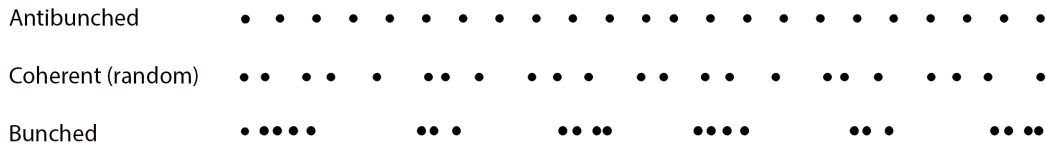


Figure 1.3. Comparison of the photon streams for antibunched light, coherent light and bunched light. The Poissonian photon statistics in the case of coherent light correspond to random time intervals between the photons.

As we have already seen in section 1.3, bunched and coherent light are compatible with classical results, instead anti-bunched light has no classical counterpart and it is a purely quantum optical phenomenon. This is the case of an ideal photon source.

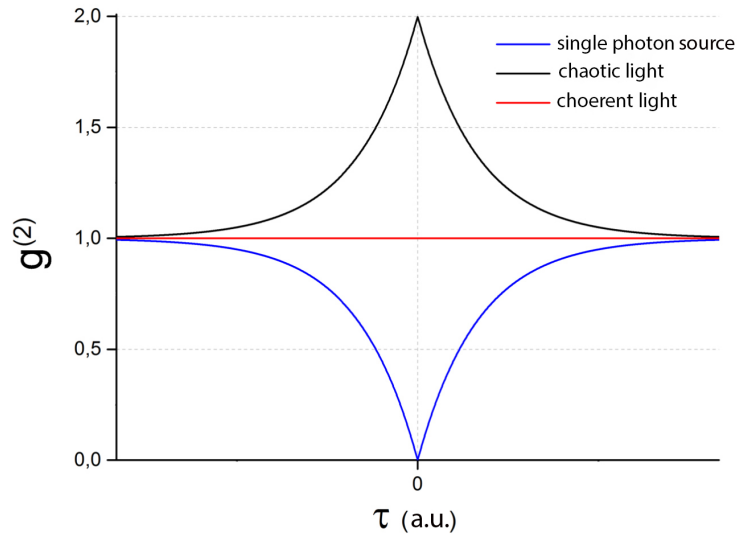


Figure 1.4. Simulation of the second order field autocorrelation functions, calculated for a single photon source (blue), coherent light (red) and chaotic light (black). For single photon source, the characteristic profile of the antibunching dynamics is observed at $\tau = 0$.

1.5 The Hanbury-Brown and Twiss (HBT) interferometer

The second-order correlation function was conceptually introduced by the experimental work of Hanbury-Brown and Twiss in 1950s, when they developed an intensity interferometer to measure the angular diameter of stars [45] [46]. A schematic illustration of the HBT interferometer is shown in figure 1.5. A stream of photons is incident on a 50 : 50 beam splitter that equally divides it between the two outputs on the detectors $D1$ and $D2$; the resulting output beams are fed into an electronic unit that records the time elapsed between counts from $D1$ and $D2$ and counts the number of pulses at each input [44]. Since the number of counts on a photon-counting detector is proportional to the intensity, it is possible to rewrite the classical second order correlation function in eq. 1.4:

$$g^{(2)}(\tau) = \frac{\langle n_1(t)n_2(t+\tau) \rangle}{\langle n_1(t) \rangle \langle n_2(t+\tau) \rangle} \quad (1.27)$$

where $n_1(t)$ and $n_2(t)$ are respectively the number of counts on detectors $D1$ and $D2$ at time t . This quantity gives the conditional probability of detecting a second photon at time $t+\tau$, given the detection of a photon at t . By varying the time delay between the detection events, $g^{(2)}(\tau)$ can be measured. Thus we can deduce that, if photons arrive in bunches, half of the photons are split towards $D1$ and the other half towards $D2$, with a high probability that both detectors register simultaneously a detection event. If instead we consider single photons with long time intervals between them, following the same procedure, we therefore would expect no events at $\tau = 0$, but some events for larger values of τ .

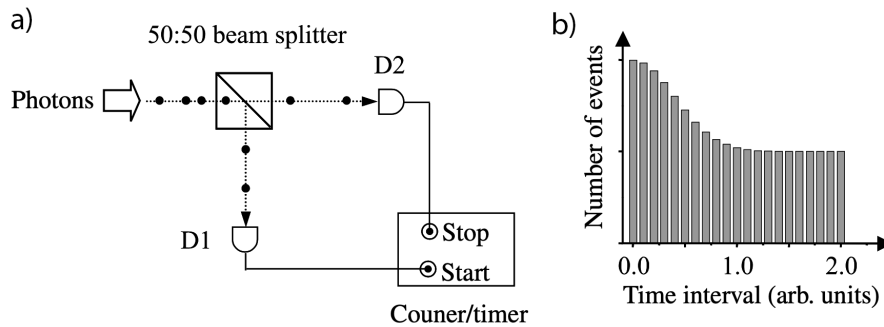


Figure 1.5. a) Hanbury-Brown and Twiss (HBT) experiment. A photon stream is incident on the beam splitter. The pulses from the single-photon counting detectors D1 and D2 are fed into an electronic counter/timer which counts the number of pulses from each detector and records the time that elapses between the pulses at the start and stop inputs. b) Histogram showing the number of events recorded in a particular time interval for a bunched photon stream. Figure taken from reference [44].

1.6 The ideal single-photon source

A single-photon source should produce light pulses with no more than one photon, in a pure quantum state and as efficiently as possible. To describe these features, we can define the following properties:

- **Single-photon purity:** this property is measured by the second-order auto-correlation function, described in section 1.4. We have seen that a light field with no more than one photon leads in principle to $g^{(2)}(0) = 0$. However there are many factors that can affect the purity of a source. Imperfections in the measuring apparatus can in fact lead to the simultaneous detection of several photons: there may be an inefficient collection or a high background noise due to the dark counts of the detectors. A high single-photon purity is required in quantum communications, quantum computation and simulation [47].
- **Indistinguishability:** in order to be indistinguishable, two photons must be in exactly the same spatial mode and described by the same coherent wavepacket⁴. The indistinguishability is therefore characterized by the mean photon wavepacket overlap M , commonly assessed by interferometric measurements through the Hong-Ou-Mandel experiment [48]. Perfect indistinguishability is characterized by $M = 1$. Poor spectral, temporal or spatial mode overlaps as well as non-matching polarization states lead to a strong corruption of this value [49].
- **Brightness:** the brightness of a single-photon source may have different definitions. A commonly used definition is the probability B that each light pulse contains a single photon, without vacuum component $|0\rangle$. For a deterministic single-photon source $B = 1$, but this value is strongly affected by any optical loss. The brightness is one of the factors that determines the speed of quantum communications or computation protocols [47].

⁴It is the case of single-photon source with a Fourier-transform-limited spectrum.

- **Quantum Yield:** this quantity, which is not independent from brightness, is defined as [50]:

$$QY = \frac{\Gamma_R}{\Gamma} \quad (1.28)$$

where $\Gamma = \Gamma_R + \Gamma_{NR}$ is the sum of all the decay rates in the channels available for spontaneous emission, respectively radiative and non-radiative decay rates. In an ideal single photon source, photons are generated by decays along a single radiative channel. However, real emitters, once excited, can decay towards an intermediate state from which they relax in a non-radiative way, or emitting photons with a frequency different from the desired one.

1.7 Blinking and bleaching

The emitter's quantum efficiency can be undermined by different undesired phenomena, such as *blinking* and *photon-bleaching* [50].

The fluorescence blinking, also referred as fluorescence intermittency, has been observed for a wide range of single emitters, including quantum dots [51] [52], color centers in diamonds [53] [54] and single molecules [55] [56]. It consists in strong fluctuations in the photoluminescence of a single emitter under excitation: the emitter's photoluminescence switches on and off on time scales spanning from microseconds to hundreds of seconds. This effect can be easily observed in the *luminescence time-trace*, that is a graph of the luminescence's intensity as a function of time. A typical trace is reported in figure 1.6, showing clearly strong fluctuations in the emission intensity between high and low intensity states.

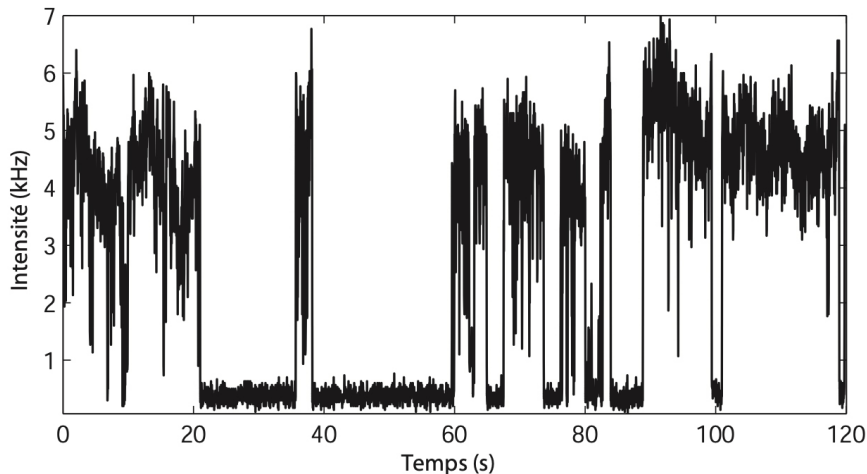


Figure 1.6. CdSe/ZnS nanocrystal photoluminescence time-trace. Succession of high and low emission periods are clearly observed. Figure taken from [57].

It was observed that the distributions of ON and OFF periods are governed by a par-

ticular type of statistics, called *Levy statistics*[58], which is characterized by nonstandard statistical properties such as statistical aging and ergodicity breaking[59][60].

Since the initial observation[61], the blinking has been studied extensively [62] [63] [64]. The details of the underlying mechanism responsible for blinking are still debated, although it is generally agreed that non-fluorescence periods during blinking are directly result of charge carrier trapping, as I will describe in chapter 4.

In the photo-bleaching of the emitter, differently, the efficiency drops irreversibly and not resumes, resulting in a permanent *off* state. This phenomenon is caused by an irreversible process, for example by a photo-induced chemical reaction. To distinguish between blinking and bleaching it's therefore necessary to check if the luminescence is resumed or not, although bleaching often takes place at longer timescales than blinking.

It is clear that these phenomena deeply undermine the possible applications of a single photons source and many efforts are being made to suppress or at least reduce them.

1.8 Main single photon sources

In recent years, different physical systems have been studied in order to realize single photon sources [12] [50].

A first category is represented by **nonlinear processes**, such as parametric down conversion in bulk crystals [65] and waveguides [66], and four-wave mixing in optical fiber [67]. In these techniques pairs of related photons are created according to phase-matching condition $\Delta k = 0$ and energy conservation: the detection of the first photon announces the existence and the physical properties of the partner. These are probabilistic processes and do not allow, in principle, an efficient on-demand generation. Furthermore, it is necessary to operate at low laser powers in order to have a negligible probability of generating more than one couple, further limiting quantum efficiency. In order to be used as efficient sources in quantum optics experiments, multiplexing schemes [68] [69] must be adopted to organize multiple parametric sources in order to increase the probability of emission from a single pair, keeping the probability of multiple emission negligible.

Cold atoms and ions can also be used. The level transitions of interest are in particular those related to the hyperfine structure, well known and which clearly provide a reproducible system. In the absence of Doppler effect and collisions with the residual gas, these transitions are narrow and very stable under laser illumination. Thanks to the absence of non-radiative channels, these systems also have a quantum efficiency close to unity and an emission of single photons on demand. However the main issues are isolation, manipulation and entrapment of single atoms, which require an experimental apparatus that is difficult to scale to a large number of high emitters.

Another important category of single photon sources is represented by **solid-state**

emitters, such as individual organic molecules, color centers and nanocrystals in various morphologies, which have the main advantage of being scalable on chip and integrated into devices.

Organic molecules were the first solid-state systems on which the photon antibunching phenomenon was observed [21]. These have the advantage of being intrinsically identical objects and are also very simple to create, through rapid and inexpensive chemical synthesis protocols. Their nanometric size also makes them excellent candidates for scalability and integration on future devices. By working at low temperatures, it is possible to achieve high efficiency values that can be further improved if the emitter is implanted within crystalline matrices; in this way the photophysical properties of the molecule are preserved. Otherwise interaction with the surrounding environment causes bleaching, blinking and low photostability [70] [71].

Color centers are crystallographic defects in inorganic crystalline semiconductor structures due to substitutional or interstitial impurities and vacancies. These defects introduce energy levels within the energy gap between the valence band and the conduction band allowing absorption and fluorescence mechanism initially forbidden. The major example is diamond, within which it is possible to create different types of defects, such as nitrogen-vacancy centers (NV), silicon-vacancy centers (SiV), and silicon carbide centers (SiC) [72]. These emitters are characterized by high stability and show a stable single photons emission even at room temperatures, however the emission is not very intense and is affected by spectral diffusion. Having a high refractive index, the diamond also makes the extraction of fluorescence light complicated; in order to increase the collection efficiency and reduce the background, a possible strategy is to create nanocrystals [23].

Semiconductor **quantum dots (QD)** have been long studied as single-photon sources. They are formed by a semiconductor material, with a certain energy band gap and a size comparable to the De Broglie wavelength, within a second semiconductor with a larger band gap; this confines in the three dimensions of space the charge carriers in a spatial region characterized, like for atoms, by discrete energy levels. Quantum dots can be fabricated by molecular beam epitaxy (MBE), in which self-assembly processes allow the formation of islands of nanoscopic size [73] or through chemical synthesis, producing colloidal quantum dots [74]. In weak excitation regime an exciton can be produced on demand in these systems and radiative recombination of the electron-hole pair results in single-photon emission. The small QD's size makes them suitable for integration into micro-cavities such as micro-pillars, disks or spheres to significantly increase the spontaneous emission rate through the Purcell effect, or in photonic structures, such as Bragg mirrors, to control the emission direction. A disadvantage of these nanostructures is the presence of spectral diffusion and blinking phenomena [63].

Recently the interest in perovskites, originally studied for solar-cell applications [75], has increased in this field. **Perovskite nanocrystals** are versatile emitters and promising nano-objects for quantum applications [76], showing single photon emission

at low [?] and room [29] temperatures. They present several advantages with respect to competitors: in addition to being used at room temperature - differently from epitaxial quantum dots - they are easily synthesized by low-cost, well mastered wet chemistry techniques, differently from single defects in nanodiamonds and epitaxial quantum dots which require heavy fabrication facilities. Moreover, their emission's wavelength can be tuned playing on their size and composition. Thus, by choosing an appropriate perovskite composition, they can emit in near-infrared, differently from II-VI colloidal quantum dots.

Optical stability is the main limitation in their use and to reduce this problem different solutions have been attempted: polymer encapsulation [77] [78], alumina encapsulation using atomic layer deposition [79] [80] or surface passivation [81].

In these thesis high stability samples of perovskite nanocrystals will be presented, showing at the same time reduced blinking and strong antibunching of the emission.

Chapter 2

CsPbX₃ perovskites

In recent years metal halide perovskites have been the subject of numerous studies motivated by rapid advances of their performance in solar cells, whose efficiency has increased from 3 – 4% to 20% in ten years [29]. Despite this has greatly contributed to put perovskites into research spotlight, inorganic lead halide perovskites have been known since the end of the 19th century [82] - although their semiconductor nature was reported only in 1950s [83] - while hybrid organic-inorganic lead halide perovskites have been known since the late 1970s [84]. Very recently, a further explosion of interest has been observed, motivated by some advantageous optical and electrical properties of this versatile material which could offer unique opportunities for a new generation of optoelectronic devices, including light-emitting diodes (LEDs) [85] [86] and laser [87] [88]. In addition, the synthesis of nanostructured forms of perovskites allows the effects of quantum confinement to be used to provide quantum light sources at room temperature. In this chapter I will illustrate the chemical composition and the main crystalline structures of perovskites, giving more emphasis to cesium lead halide perovskites and focusing on the optical and electronic characteristics that make this type of perovskite interesting materials. Finally, I will list the main synthesis methods, the main issues and the key challenge to their further development.

2.1 Chemical composition and structural landscapes

The term *perovskite* is associated with compounds having the same crystalline structure as calcium titanate ($CaTiO_3$). The general structural formula is ABX_3 where A is a organic or inorganic cation, B is a metal and X is a halide. The ideal crystal structure consists, as showed in figure 2.1, in a 3D anionic network of corners sharing $[BX_6]^{4-}$ octahedra with a 12-fold coordinated A cation occupying the site in the middle of the cube surrounded by 8 octahedra. It is possible to give an equivalent description in terms of elementary cell: the A and B ions are arranged according to a cubic centered-body structure, with the A ions at the vertices and the B ions in the center, while the X ions are arranged in the center of each cube's face.

Materials with perovskite-type crystal structure are known for their complex structural landscapes with a large number of possible polymorphs. Indeed, perovskites undergo structural changes upon application of external stimuli, such as

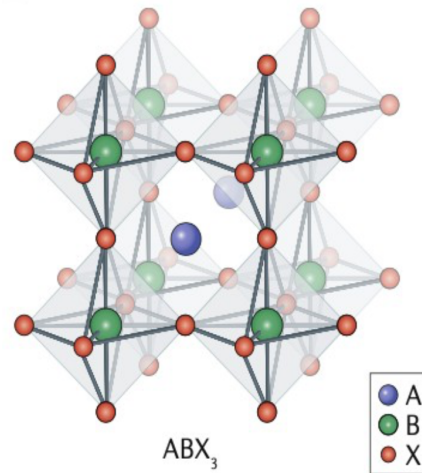


Figure 2.1. Crystal structure of 3D perovskites with general structural formula ABX_3 . Figure taken from reference [89].

temperature, pressure or applied electric field [90]. The ideal cube structure responds to such stimuli by forcing the BX_6 octahedral network to tilt lowering the symmetry of the structure [91] [92], as shown in figure 2.2. These deviations from cubic symmetry depend on the characteristics of each compound.

Three 3D polymorphs are generally observed [93]: cubic, tetragonal and orthorhombic, in order of decreasing symmetry. In particular, many studies have been carried out on the transition from orthorhombic to tetragonal to cubic perovskite structures as a function of temperature. For example, in the case of $CsPbBr_3$, the passage from the cubic to the tetragonal phase was revealed at 403 K, while the passage from the tetragonal to the orthorhombic phase at 361 K [94]. In general, perovskite have different optical properties depending on the crystalline phase in which they are found.

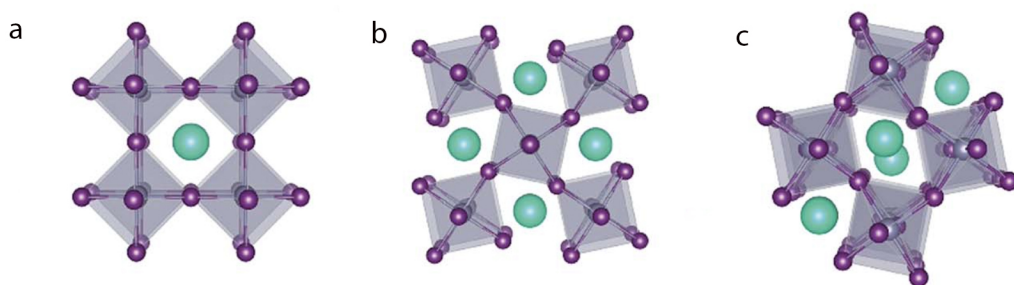


Figure 2.2. 3D perovskite structures in order of decreasing symmetry: a) cubic phase, b) tetragonal phase, c) orthorhombic phase. Figure taken from reference [95].

There are some criteria to empirically predict the stability and the lattice

distortion of perovskite's compounds. Firstly, *Goldschmidt's tolerance factor* is used:

$$t = \frac{r_A + r_X}{2^{\frac{1}{2}}(r_B + r_X)} \quad (2.1)$$

in which r_A , r_B and r_X are the radii of A, B and X ions respectively. As we can see in figure 2.3, a t value between 0.8 and 1 is a favorable condition to obtain a perovskite structure; in particular for $0.9 < t < 1$ a cubic structure is obtained and for $0.8 < t < 0.9$ a distorted one [89]. Larger or smaller values usually do not allow formation of perovskite structures. Moreover, perovskites at the limit of the tolerance factor requirement ($t \approx 0.8$ or $t \approx 1$) are metastable at room temperature.

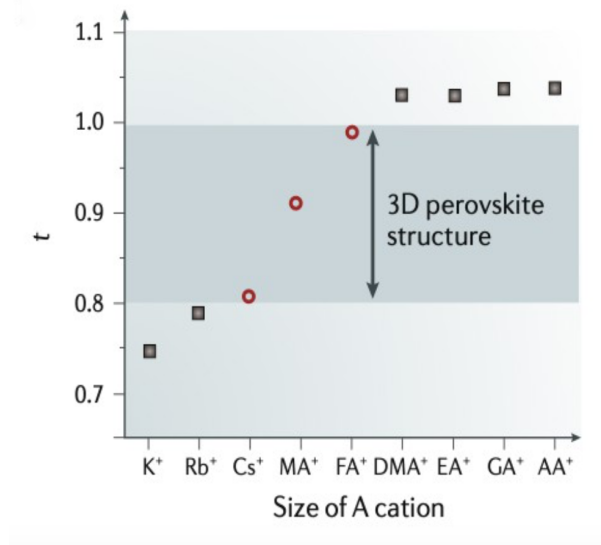


Figure 2.3. Tolerance factor for different A cations. Figure taken from reference [89].

However, the definition of an ionic radius is challenging in some cases, such as for organic A cations, where hydrogen-bonding interactions cause varying bond lengths. To solve this problem was proposed [96] a rigid sphere model applicable to organic cations to obtain an effective ionic radius $r_{A,eff}$:

$$r_{A,eff} = r_{mass} + r_{ion} \quad (2.2)$$

where, assuming free rotational freedom around the center of mass, r_{mass} is the distance between the molecule's centre of mass and the atom with the longest distance to the centre of mass, instead r_{ion} is the ionic radius of this atom.

An additional criteria for the possibility to form perovskites is the *octahedral factor* given by the ratio of the ionic radius of B and X atoms:

$$\mu = \frac{r_B}{r_X} \quad (2.3)$$

Even though the system has a very favorable tolerance factor, a value of μ lower than 0.442 do not allow the formation of a stable perovskite structure [97]. Anyway, both

tolerance factor t and octahedral factor μ are necessary but not sufficient conditions for ABX_3 halide perovskite formation.

By keeping the same chemical structure (ABX_3) but starting from different elements, numerous compounds with different optical properties can be made. The choice of the different elements, the most common of which are listed below, therefore depends on the type of application.

- **A site**

Depending on the nature of A cation, perovskites are classified as hybrid or inorganic. In hybrid perovskites A is an organic cation, such as formamidinium ($HC(NH_2)_2^+$, FA) or methylammonium ($CH_3NH_3^+$, MA); in inorganic perovskites the A cation is inorganic, such as potassium (K), rubidium (Rb) and cesium (Cs). The A cation does not directly contribute to the electronic properties due to negligible overlap of electron orbitals between the organic component and inorganic BX_6 octahedra [93]. However, the size of A cations can affect the degree of distortion changing indirectly the electronic properties. In general, as shown in figure 2.3, the choice of a suitably small monovalent cation (Cs, MA, FA) makes favorable the 3D symmetry; in particular, cesium is the inorganic cation most employed.

- **B site**

The B metal cation sites are occupied by a metal of the group 14 of the periodic table in a divalent oxidation state, such as lead Pb^{2+} , tin Sn^{2+} and germanium Ge^{2+} . Lead has been the most widely employed due its superior performance and stability compared to tin and germanium. In particular, tin-based compounds are more sensitive to temperature and humidity and germanium-based ones have been less studied due to germanium's instable nature in 2+ oxidation state [93].

- **X site**

The halide anion has been the most varied component in perovskites; iodine (I), chlorine (Cl) and bromine (Br) are commonly used. Iodide has provided the foundation for hybrid perovskites, but its substitutes are of great interest because its ease of oxidation undermines the perovskites stability. Bromine has been the most effectively used for its better stability under ambient operating conditions.[98] [99].

In this thesis I will focus on perovskites in which the A cation is cesium and the B cation is lead, in particular on $CsPbBr_3$.

2.2 Electronic and optical properties

All $CsPbX_3$ ($X = Cl, Br, I$) compounds have similar electronic properties and all are characterized by a direct band gap¹ at R point of the band structure, as shown in figure 2.4 (panel a) for $CsPbBr_3$. The electric structure of $CsPbX_3$, including scalar relativistic and spin-orbit interactions, has been studied in numerous works [100] [101] in which the band structure is described in the framework of the density functional theory. These works agreed that the maximum of the valence band is formed predominately by the hybridized halide (X) p-orbitals and the minimum of the conduction band is formed by the overlap of the Pb p-orbitals [102]. This is visible in Figure 2.4b, showing the density of states of the cubic phase of $CsPbBr_3$ with the corresponding contributions of the different elements to the energy band.

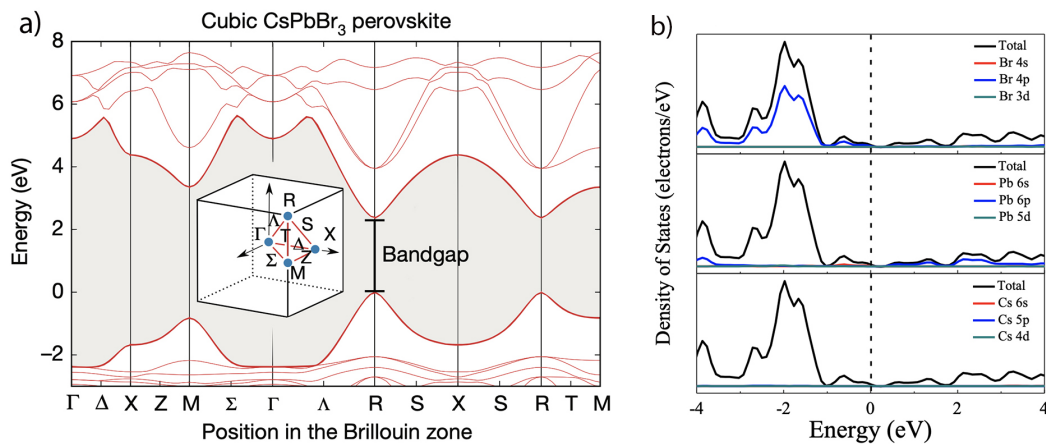


Figure 2.4. a) Band structure of cubic $CsPbBr_3$ perovskite. The electronic bandgap is indicated in the band structure at the R point. Figure taken from reference [103] b) Density of states (DOS) of cubic $CsPbBr_3$ with corresponding contributions of elements to energy gap. Figure taken from reference [104]

The bandgap of $CsPbX_3$ perovskites varies according to the halide employed. In fact, since the maximum of valence band contains some X p-orbitals and the energy levels of the p-states of the X ions increases from Cl to I, the maximum of valence band up-shifts and the band gap becomes smaller from Cl to I [102], as shown in table 2.1.

Table 2.1. Energy gap at room temperature (300K) for different $CsPbX_3$ compounds.

Compounds	Energy gap	Reference
$CsPbCl_3$	2.85 eV	[105]
$CsPbBr_3$	2.23 eV	[105]
$CsPbI_3$	1.73 eV	[106]

¹The band gap is defined as the difference between the maximum of the valence band (VBM), that is the highest energy electronic band occupied at $T = 0K$, and the minimum of the conduction band (CBM), that is the lowest energy unoccupied electronic band at $T = 0K$.

The great interest in $CsPbX_3$ perovskites arises from the fact that optical absorption and emission spectra can be tuned over the entire visible spectral region by simply adjusting the halide composition or by varying the nanocrystal's size. Their photoluminescence is characterized by high quantum yields of 50 – 90% and narrow linewidths² of 12 – 45 nm. For example, $CsPbCl_3$ shows 12 nm width in the blue limit of the visible range, $CsPbBr_3$ shows 20 nm width in green region and $CsPbI_3$ shows 40 to 45 nm width in red region [30].



Figure 2.5. $CsPbX_3$ perovskites ($X = Cl, Br, I$) exhibit tunable bandgap energies covering the entire visible spectral region with narrow and bright emission: (a) colloidal solutions in toluene under UV lamp; (b) representative PL spectra; (c) typical optical absorption and PL spectra. Figures taken from reference [107].

For their high quantum efficiency and their narrow emission linewidths, $CsPbX_3$ perovskites are particularly interesting for light emission applications. Indeed, compared to conventional rare-earth phosphors or organic polymers and dye, $CsPbX_3$ perovskites offer blue, green, and red primary colors with an impressive gamut. As

²The linewidth is measured as the full width at half maximum (FWHM).

shown in figure 2.6, a selected triangle of red, green, and blue emitting $CsPbX_3$ nanocrystals encompasses 140% of the North American National Television Standard Committee (NTSC) specification, extending mainly into red and green regions and even up to 100% of the newer International Telecommunication Union Rec. 2020 standard.

To investigate the size-dependent fluorescent colors of $CsPbX_3$ perovskites, several attempts to reduce the size of bulk perovskites to the sub-micron scale have been performed[108][109], until the synthesis of nanocrystals whose sizes are close to the exciton Bohr radius, corresponding to $5nm$, $7nm$ and $12nm$ for $CsPbCl_3$, $CsPbBr_3$ and $CsPbI_3$ respectively[107]. This constraint of dimensionality significantly change their electronic energy spectrum, resulting in a transition from continuous to discrete energy levels and thus reaching the quantum-confined regime[110]. This achievement allowed to explore their quantum properties [111], demonstrating an antibunching behavior of their photoluminescence emission [29]. As I will describe in chapter 3, this observation is explained by the presence of a fast Auger recombination, that is an efficient non-radiative recombination pathway strictly connected to the strong quantum confinement. It consists in an energy transfer from an e-h pair to a third particle (electron, hole or exciton) because of the Coulomb interaction and, in our case, provides an efficient channel for non-radiative dissipation of multi-excitons to prevent simultaneous emission of multiple photons.

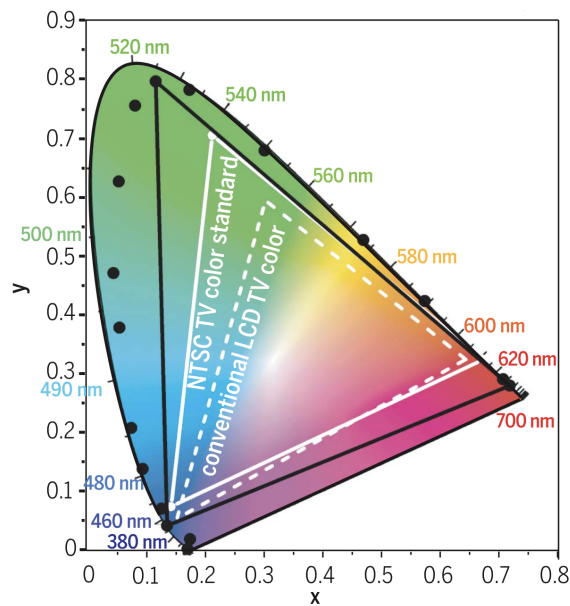


Figure 2.6. PL spectra of $CsPbX_3$ nanocrystals plotted on CIE chromaticity coordinates. A CIE chromaticity diagram, introduced by the Commission Internationale de l’Eclairage, allows the comparison of the quality of colors by mapping colors visible to the human eye in terms of hue and saturation. In this diagram the chromaticity coordinates of $CsPbX_3$ (black points) are compared with common color standards (white lines), reaching 140% of the NTSC color standard (solid black line). Figure taken from reference [107].

2.3 CsBrX₃ perovskites as single photon emitter: the state of the art

The spectroscopic investigation of the optical properties of perovskite nanocrystals at the single emitter level has been at first hampered by their poor stability under laser excitation, as explained in section 2.4, leading to an initial lack of understanding of their interesting properties in the high confinement regime[112].

Quantum confinement effect has been observed in organic-inorganic methylammonium lead halide perovskite quantum dots[113] and nanoplatelets[114] [115]. However, the unsolved photostability of organic-inorganic lead halide perovskites has made their use considerably difficult[116]. All-inorganic CsPbBr₃ perovskites have thus been regarded as potential substitutes of the hybrid organic-inorganic ones, showing at the same time a better operational stability to moisture and illumination[81], quantum confinement effect[107] and a faster non-radiative Auger recombination than in organic-inorganic perovskites, resulting in a key decay channel[117].

Moving in this direction, in 2015 single photon emission has been observed from CsPbX₃ nanocrystals at low temperature ($T = 6K$)[?], measuring a second-order auto-correlation function of $g^2(0) = 0.3$, and at room temperature with a $g^2(0) = 0.06$ [29]. In particular, the latter result has demonstrated that this kind of perovskites can serve as room-temperature sources of single photons. The difference between the g^2 values obtained at low and room temperature was explained as a possible change of the efficiency in quenching multi-exciton states via Auger recombination[118]. Unlike the numerous subsequent reports on cubic-shaped perovskite nanocrystals[110][119][103][120], the investigation of the quantum properties of nanocrystals with anisotropic shapes has received less attention and most of the studies has been rather focused on their fabrication methods[121]. Nevertheless, quantum confinement has been observed also for CsPbBr₃ nanowires[122] and nanoplatelets[123][124]. Very recently single photon emission has been demonstrated for CsPbBr₃ nanoplatelets at a temperature of 5K, reporting a value of $g^2(0) = 0.1$ [125].

Further investigations in the quantum optics properties will be possible with an improvement in the synthesis methods and the stability of lead halide nanocrystals, whose main issues are detailed in the next chapter.

2.4 Synthesis, main issues and surface passivation approaches

In recent years there has been a rapid development of the fabrication method of CsBrX₃ perovskites. Many interesting approaches have been developed to obtain nanocrystals with various morphologies, from nanocubes to nanoplates [111] [121] [126]. The approaches could be divided into two categories: *direct synthesis methods*, including hot-injection[107], room-temperature reprecipitation[127], microwave[128], ultrasonication[129] and salvothermal[130] methods and *post-synthesis methods*, such as template-assisted synthesis[131] and ion exchange[132]. For the purpose of this thesis, I will focus on the hot-injection method, illustrating the main steps.

Figure 2.7 shows the scheme of the hot-injection strategy used in the first successful synthesis of high-quality $CsPbX_3$ colloidal nanocrystals in 2015 [107]. Firstly, a PbX_2 precursor is dissolved in a three-neck flask containing octadecene, oleylamine (OAm) and oleic acid (OA); OA and OAm help to solubilize PbX_2 and stabilize the nanocrystals as surfactant. Then, a cesium oleate is injected in the flask at high temperature, varying from 140° to 200° C. After waiting several seconds, the solution is cooled down to room temperature in an ice-bath. This general approach can be modified to synthesize nanocrystals with different sizes, shapes and compositions[133].

In spite of the interesting optical properties of $CsPbX_3$ perovskites, their practical

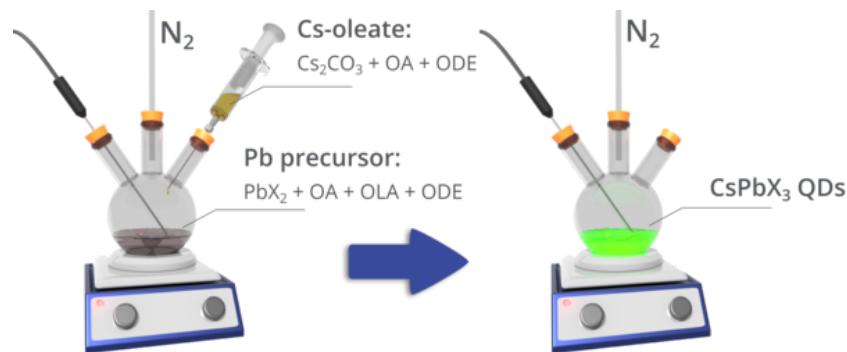


Figure 2.7. Schematic of hot injection synthesis for $CsPbX_3$ QDs. Figure taken from www.ossila.com/blogs/news/perovskite-quantum-dot-synthesis.

use is limited by different forms of instability that need to be overcome as they lead to a rapid loss of performance. In fact, although these materials are not susceptible to oxidation in the ground state, the long term stability may be limited in presence of a combination of moisture, oxygen and light.

Regarding oxygen induced degradation, it has been highlighted the importance of defects[134], in particular in the case of iodide vacancies³ in $CsPbI_3$, for photo-decomposition in presence of oxygen. The vacancies have a similar volume to molecular oxygen, offering an easy path for oxygen in the perovskite lattice. Highly reactive super-oxide O_2^- anions are formed as molecular oxygen accepts photo-excited electrons from the perovskite conduction band. These super-oxide anions can then deprotonate the A site cation, resulting firstly in decomposition to lead iodide and A-gas [95].

Whereas oxygen only decomposes the nanocrystals under light exposure, the exposure to moisture causes rapid decomposition even in the dark. Water molecules can easily penetrate the perovskite structure, forming strong hydrogen bonds with organic cations and weakening those between these cations and the PbX_6 network. This makes easier to degrade perovskite for external factors such as heat or the electric field [135].

For commercialization, moisture resistance and photo-stability should be guaranteed. Until now, surface passivation methods have proven to be quite useful for

³Iodide vacancy densities are intrinsically high and can be generated rapidly upon photoexcitation.

improving stability, mainly through modification of the surface by organic ligands and encapsulation in waterproof materials. In particular, when the nanocrystals are colloidal and dispersed in solution - as in the case studied in this thesis - the nature of the surface ligands and the nanocrystal-ligand bond are important factors which can determine photo-stability [133]. After the first successful synthesis of *CsPbX₃* nanocrystals, the OA and OAm become the most used capping ligands even if the obtained stability under dilution is not excellent. Replace OA and OAm with alternative ligands to enhance *CsPbX₃* perovskites properties is then a key challenge for future development and practical use of this materials.

Chapter 3

Experimental setup and methods

Optical spectroscopy at the single emitter level is a powerful tool to study the photo-physics of nanoemitters. Indeed, observing a single emitter removes the usual ensemble average, revealing phenomena hidden in ensemble measurements, as the fluorescence intermittency [61]. During the last thirty years various experimental methods [136] have been developed to detect single emitters fluorescence, such as near-field scanning optical microscopy (SNOM), wide-field microscopy and confocal microscopy. In this chapter, I will present the microscopy setup to perform photoluminescence, antibunching and polarization measurements. Then I will illustrate the different experimental methods employed: I will introduce a model to deduce the emitter excitation from saturation curve measurements and I will explain how we registered and processed the data. Finally I will describe the $CsPbBr_3$ synthesis and sample preparation.

3.1 Standard fluorescence microscopy techniques

In our setup both wide-field and confocal excitation schemes are used: in the wide-field scheme the sample is excited by a non-collimated light-emitting diode (LED) and a broad area of the sample, with many emitters, is illuminated; in the confocal scheme a pulsed laser is used to excite one specific emitter of the sample. In both cases, the samples are prepared by spin coating on a glass microscope coverslip a diluted solution of nanocrystals of appropriate concentration, as I will illustrate in section 3.6. The coverslip is then mounted on a motorized stage (MadCityLabs) fixed on an inverted microscope (Nikon Eclipse Ti). This stage allows a xy plane displacement such that the whole sample can be investigated and it is characterized by an excellent stability.

As showed in the complete experimental setup in figure 3.1, for both microscope configuration the excitation light - respectively at $405nm$ for the laser and at $400nm$ for the LED - is reflected towards the sample by means of a dichroic mirror¹ placed at an incident angle of 45° to the incoming light.

¹A dichroic mirror is an interference filter highly reflective below the cut-off wavelength and highly transmissive for larger wavelengths.

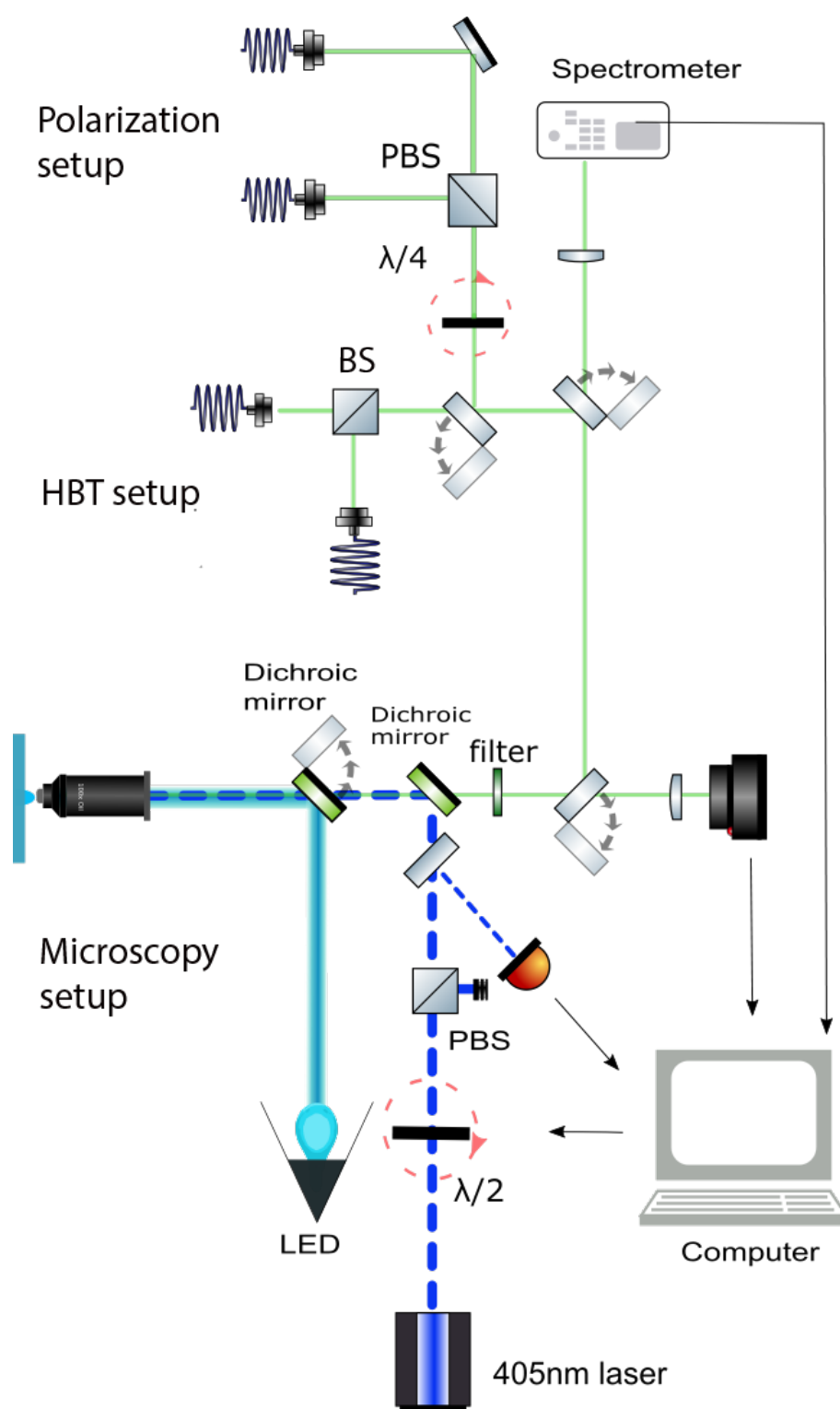


Figure 3.1. Experimental setup used for the optical and quantum characterization of the perovskites nanocrystals.

Then, an objective lens is used to both focus the excitation light on the sample and back-collect the nanoemitter's fluorescence. This objective lens is a crucial element of the microscope system, determining light transmission, image contrast and resolution. To obtain a high (diffraction-limited) spatial resolution, it is useful to use an oil immersion objective, in which a small drop of oil is deposited between the front lens of the objective and the glass coverslip, instead of having an air gap. Oil has a refraction index of 1.515, closer to the refractive index of the glass coverslip $n = 1.523$ than air. This increases the maximum angle of the cone of light that can enter the front lens of the objective, which is a characteristic described by the objective's numerical aperture (NA). The higher the numerical aperture of an objective, the broader its angular collection.

In our measurements we used an oil objective with NA= 1.4, a magnification of $100x$ and a collection efficiency of $C = 78\%$ for standard fluorescence and antibunching measurements, instead an objectives with NA= 0.95, a magnification of $100x$ and a collection efficiency of $C = 17\%$ for polarization measurements. This choice is due to the fact that a larger numerical aperture allows to collect light over a larger solid angle and thus it modifies the collected polarization pattern and measured degree of polarization[137] [138].

The light collected by the objective from the sample is then sent towards the detection apparatus after being suitably filtered, as showed in figure 3.1 and explained below.

Wide-field microscopy

The wide-field scheme, whose operating principle is illustrated in figure 3.2, has only been used to image samples on a CCD camera for an overview of the sample, giving us the possibility of exploring it and then systematically selecting a single emitter to be characterized. In this scheme a large area of the sample is excited by a non-collimated light beam from the LED at 400 nm (CooLED pE-100 LightSource). This LED provides a full irradiance of $25W$ with a precise irradiance control in 1% steps (from 0% to 100% of the full irradiance). For the ensemble measurements we set an irradiance value of $2.5W$.

The LED beam is reflected by the dichroic mirror with a cut off at 432 nm (Edmund), then the objective lens focuses it on the sample. The ensemble fluorescence is back-collected by the objective lens and spectrally isolated from the residual LED excitation using the same dichroic mirror mentioned above and a long-pass filter with a cut on of 450 nm (THORLABS). The fluorescence is then imaged on a high quantum-efficiency CCD camera (HAMAMATSU ORCA Flash 4.0 LT).

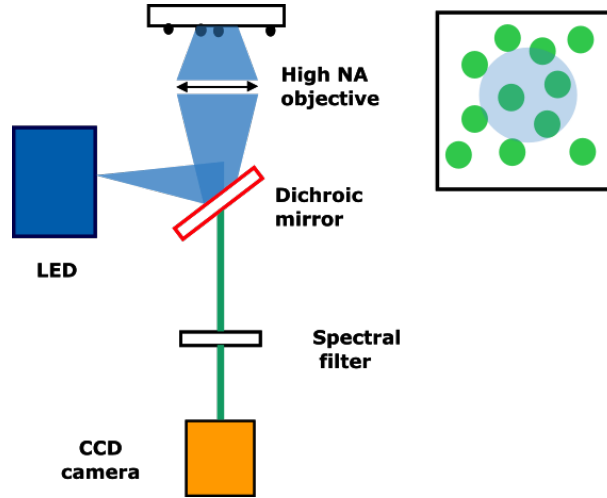


Figure 3.2. Wide-field configuration, where a large area of the sample is excited by a LED and observed on a CCD camera.

Confocal microscopy

Confocal microscopy gives the possibility of exciting a single nanocrystal at a time. In our case the emitters are arbitrarily distributed with a mean separation distance of $10\mu m$, thus this microscopy scheme is fundamental for isolating and detecting single emitters without simultaneously exciting several emitters and collecting the light emitted from adjacent ones. The operating principle of a confocal fluorescence microscopy is illustrated in figure 3.3.

We use a picosecond pulsed diode laser (LD405-B, PicoQuant), emitting at 405 nm with a repetition rate adjustable between 2.5 MHz and 5 MHz and a pulse width of less than 50 ps. The laser beam is coupled to a single mode fiber in order to clean the beam shape, then it is reflected by the dichroic mirror with a cut off at 405 nm (SEMROCK) and it is sent to the sample through the objective lens.

In order to study the fluorescence from different single nanocrystals over a large area on the substrate, the sample is scanned using the motorized stage previously mentioned. The stage allows displacements with an accuracy of less than $1\mu m$, a repeatability of less than 100 nm, a step resolution of 95 nm and a maximum speed of 2 mm/s. The stage is positioned such that the single nanocrystal is at the center of the laser spot. The nanocrystal fluorescence is back-collected and collimated by the objective lens and then spectrally filtered with the dichroic mirror and a long-pass filter with a cut on of 405 nm (SEMROCK) in order to remove residual laser excitation.

The collected light can be imaged on the high quantum efficiency CCD camera or collimated by a lens and sent to a spectrometer (Princeton Instrument-Spectra Pro) equipped with a similar high quantum efficiency CCD camera. Alternatively, using a flip mirror, the collected light can be sent to the polarization measurement set-up described in section 3.2 or, using a second flip mirror, it can be sent to a pair of avalanche photodiodes (APDs, Excelitas) in a Hanbury Brown-Twiss (HBT) configuration. In this case a 50 : 50 beam splitter divides the photoluminescence

in two arms and the photoluminescence is focused by means of two lenses on the respective detectors, as shown in figure 3.1. The last part of the setup concerning the acquisition process will be detailed in section 3.4.

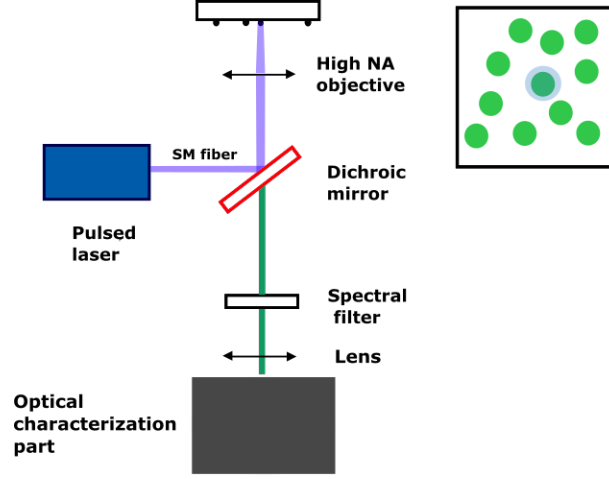


Figure 3.3. Operating principle of a confocal configuration.

3.2 Polarization microscopy

To determine the degree of polarization of the light emitted by the nanocrystals we measure the Stokes polarization parameters that describe the polarization behavior of an optical beam. These parameter are a set of four real numbers (S_0, S_1, S_2, S_3) defined starting from the complex E_x and E_y components of the real vector that describes the electric field:

$$\begin{aligned} E_x(z, t) &= E_{0x} \cos(\omega t - kz + \delta_x) \\ E_y(z, t) &= E_{0y} \cos(\omega t - kz + \delta_y) \end{aligned} \quad (3.1)$$

where t is time, E_{0x} and E_{0y} are the maximum amplitudes of the optical field, ω is the angular frequency, k the wave vector's modulus, δ_x and δ_y the phase constants. In a matrix form they are given by:

$$S = \begin{Bmatrix} S_0 \\ S_1 \\ S_2 \\ S_3 \end{Bmatrix} = \begin{Bmatrix} E_{0x}^2 + E_{0y}^2 \\ E_{0x}^2 - E_{0y}^2 \\ 2E_{0x}E_{0y} \cos \delta \\ 2E_{0x}E_{0y} \sin \delta \end{Bmatrix} \quad (3.2)$$

where $\delta = \delta_x - \delta_y$. From eq. 3.2 we see that they are described in terms of intensities (amplitudes squared) and therefore can be measured by using standard photodiodes. Stokes parameters have a relatively simple experimental interpretation:

- S_0 describes the total intensity of the optical field;

- S_1 describes the preponderance of linearly horizontally polarized light over linearly vertically polarized light;
- S_2 describes the preponderance of linear $+45^\circ$ polarized light over linear -45° polarized light;
- S_3 describes the preponderance of right circularly polarized light over left circularly polarized light.

The degree of polarization is defined by

$$P = \frac{\sqrt{S_1^2 + S_2^2 + S_3^2}}{S_0} \quad (3.3)$$

Experimentally we determine the Stokes parameters starting from a simple setup consisting of a quarter wave plate followed by a polarizer as described by Berry et al. [139]. According to this method, the intensity of the optical beam on the detector is given by:

$$I(\theta) = \frac{1}{2}(S_0 + S_1 \cos^2 2\theta + S_2 \cos 2\theta \sin 2\theta + S_3 \sin 2\theta) \quad (3.4)$$

To extract the Stokes parameters from the measured intensity in order to obtain the value of P , this equation can be rewritten by using the trigonometric half-angle formula[140] to yield:

$$I(\theta) = \frac{1}{2}(A + B \sin 2\theta + C \cos 4\theta + D \sin 4\theta) \quad (3.5)$$

where

$$A = S_0 + \frac{S_1}{2}, \quad B = S_3, \quad C = \frac{S_1}{2}, \quad D = \frac{S_2}{2} \quad (3.6)$$

Fitting the experimental data with the function 3.6, we can extract the Stokes parameters from the A, B, C, D values obtained from the fit:

$$S_0 = A - C, \quad S_1 = 2C, \quad S_2 = 2D, \quad S_3 = B \quad (3.7)$$

Finally, we can calculate the degree of polarization through the equation 3.3.

Setup

The fluorescence beam is directed to the branch dedicated to polarization measurement, using a flip mirror placed before the HBT setup, as showed in the complete setup in figure 3.1. According to Berry's method, a quarter-wave plate on a motorized rotation stage together with a polarizing beam splitter cube is used, as shown in figure 3.4. The collimated fluorescence light passes through the quarter-wave plate and it is separated in two arms by the polarizing beam splitter cube; each arm is focused on a single photon counting avalanche photodiode. During measurements the quarter-wave plate can be rotated from its initial position. The intensity of the optical beam on the detector is given by the quantity in equation 3.4. We plot the intensity detected by one photodiode normalized by the total intensity detected on both photodiodes in order to account for fluctuations of the total emitted intensity

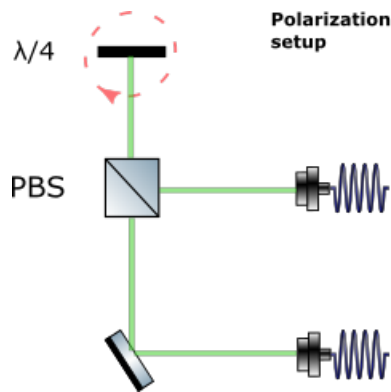


Figure 3.4. Top view of the polarization set-up. One output port of the PBS is sent to the detection while the other is used for normalize the intensity.

due to emitter's blinking. For these measurements we used the objective with a numerical aperture $NA = 0.95$ and not the oil immersion objective ($NA = 1.4$). In fact, as explained in section 3.1, a larger numerical aperture allows to collect light over a larger solid angle and it can modify the collected polarization pattern and the measured degree of polarization. A typical output reported in literature[141] is showed in Figure 3.5, respectively for a $CsPbBr_3$ perovskite nanocube and nanowire. The polarized emission from the nanowire is assigned to its very anisotropic shape, instead the cubic crystalline structure of the nanocube determines an almost total absence of polarization.

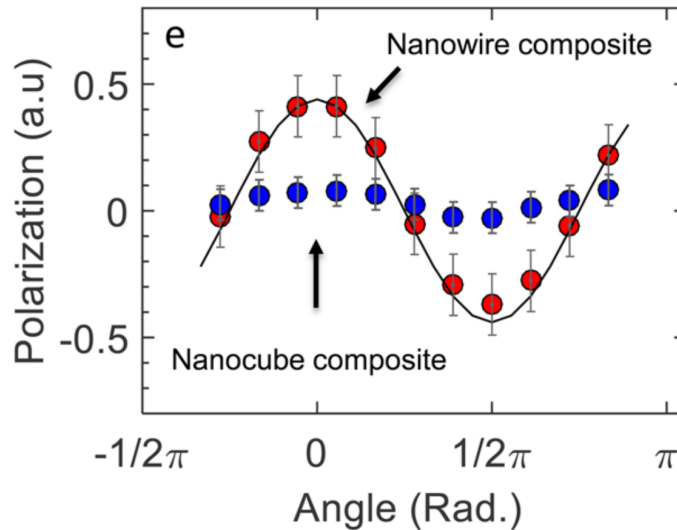


Figure 3.5. Typical polarization trend for perovskite nanocubes and nanowires, respectively. Figure taken from reference [141].

3.3 Photoluminescence as a function of the excitation power

The nanocrystal's photoluminescence strongly depends on the excitation power. It is therefore necessary to evaluate how the emitters are excited by the laser independently of the specific configuration of the setup, such as laser spot diameter. One parameter that allows this analysis is the average number of electron-hole pairs generated by the excitation inside the crystal $\langle N_{eh} \rangle$. As we have seen in section 1.4, laser pulses contain a random number of photons with a Poisson distribution. The laser excitation can produce a certain number of electron-hole pairs N_{eh} inside the nanocrystal's quasi-continuum of states ² that follows a Poisson distribution $P(N_{eh}, \langle N_{eh} \rangle)$ whose mean value $\langle N_{eh} \rangle$ depends on the excitation power. Any of this m -multiexciton state decays to the $(m - 1)$ state through an electron-hole recombination which can occur radiatively or non-radiatively with a probability to emit a photon given by the quantum yield for the m -multiexciton state QY_m . This is defined as:

$$QY_m = \frac{\gamma_{R,m}}{\gamma_{R,m} + \gamma_{A,m} + \gamma_{NR,m}} \quad (3.8)$$

where γ_R is the radiative recombination rate, γ_A is the Auger recombination rate - responsible for single photon emission as I will explain - and γ_{NR} describes other non-radiative decay channels than Auger one.

A multi-photons quantum cascade process is then created[142] and it is repeated until all the electron-hole pairs have recombined. As the number of electron-hole pairs created inside the nanocrystal increases with the excitation intensity, the photon statistics is modified because the probability to emit multiple photons increases[143]. Also the blinking, as explained in section 4.4, depends on the number of electron-hole pairs inside the crystal. We understand then why it is important to evaluate N_{eh} . Below we present a theoretical model[144] with the aim of study the saturation behavior in the case of a quantum cascade of multi-photons in order to control the laser excitation and interpret the measurement.

According to this model, the mean number of photons emitted by a nanocrystal after a given excitation pulse can be written as follow:

$$N_{ph} = \sum_{N_{eh}=1}^{\infty} P(N_{eh}, \langle N_{eh} \rangle) \sum_{m=1}^{N_{eh}} QY_m \quad (3.9)$$

Whit a statistical scaling approach[145] [146], the higher orders multi-excitonic quantum yields QY_m in eq 3.9 can be written in terms of single exciton and bi-exciton QYs:

$$QY_m = \frac{QY_2}{m(1 - QY_2) - QY_1} \quad (3.10)$$

²Under a laser excitation at 405 nm - corresponding to an energy much higher than the *CsPbBr₃* bandgap - the electron energy levels can be considered as a quasi-continuum of states.

where

$$QY_1 = \frac{\gamma_{R,1}}{\gamma_{A,1} + \gamma_{NR,1} + \gamma_{R,1}}$$

$$QY_2 = \frac{\gamma_{R,2}}{\gamma_{A,2} + \gamma_{NR,2} + \gamma_{R,2}}$$

and where $\gamma_{R,1-2}$, $\gamma_{A,1-2}$, $\gamma_{NR,1-2}$ are the radiative, Auger and non-radiative decay rate for the exciton and biexciton state, respectively.

Let us now consider three different cases:

- **All multi-excitonic Quantum Yields are suppressed by efficient Auger recombination**

In this case $\gamma_A \gg \gamma_R$, thus $QY_m \approx 0$. and eq. 3.9 becomes:

$$N_{ph} = QY_1(1 - e^{-N_{eh}}) \quad (3.11)$$

At high excitation $e^{-N_{eh}}$ goes to zero and a saturation of N_{ph} occurs.

- **Multi-exciton states are not quenched by any non-radiative relaxation process**

If multiexciton states are not quenched by any non-radiative relaxation process, like Auger effect, the quantum yield is identical for any number m of excitons ($QY_m = QY'$) and the photon emission statistics will follow the excitation linearly:

$$N_{ph} = QY' \langle N_{eh} \rangle \quad (3.12)$$

- **Multi-exciton emission are imperfectly quenched by Auger non radiative recombination**

In this case multi-exciton quantum yields are not negligible. For $\langle N_{eh} \rangle$ up to 5, equation 3.9 can be approximated as:

$$N_{ph} \simeq QY_1[(1 - e^{-\langle N_{eh} \rangle}) + c \frac{QY_2}{QY_1} \langle N_{eh} \rangle] \quad (3.13)$$

In fact, the multiexciton contribution in eq. 3.9, that we can labeled with N_m , can be approximated by a linear function[147] depending only on the biexciton quantum yields:

$$N_m \simeq cQY_2 \langle N_{eh} \rangle \quad (3.14)$$

where the constant c is obtained through a fitting of different multiexciton emission curves, finding a value $c = 0.4$. The biexciton quantum yield QY_2 is experimentally measurable through the second order autocorrelation function $g_2(0)$ at low excitation power[118]:

$$\lim_{\langle N_{eh} \rangle \rightarrow 0} g_2(0) = \frac{QY_2}{QY_1} \quad (3.15)$$

Experimentally we can express equation $\langle N_{eh} \rangle$ as a function of the exciting laser power P . This quantity is indeed proportional to $\langle N_{eh} \rangle$:

$$\langle N_{eh} \rangle = \frac{P}{P_{sat}} \quad (3.16)$$

where the *saturation power* P_{sat} is the power that corresponds to $\langle N_{eh} \rangle = 1$. It is possible to rewrite the equation 3.13 in terms of photoluminescence signal I_{PL} - that is the rate of photon counts measured by the single photon detector when the nanocrystal is excited by a laser pulse with a rate Γ - due to the fact that I_{PL} is just proportional to N_{ph} . We obtain:

$$I_{PL} = A[1 - e^{-\frac{P}{P_{sat}}}] + B \frac{P}{P_{sat}} \quad (3.17)$$

where A and B depend on the intensity of single and biexciton components of the emission. By fitting the measurable data with this formula, with A , B and P_{sat} free parameters, it is possible to extract the power saturation P_{sat} in order to obtain a reference to perform the emitter characterization.

We can see that the saturation of the photoluminescence as a function of the excitation power is a useful signature of single photon emission. When all multiexcitonic QYs are suppressed by efficient Auger recombination, $QY_m \simeq 0$ for $m > 1$, the probability of emitting more than one photon for excitation pulse is negligible and a perfect saturation curve is expected. When multi-exciton states are not quenched by any non-radiative relaxation process the trend of N_{ph} is linear with the excitation power. In intermediate case of multiexciton QYs not negligible, the contribution from the multiexcitonic emission modifies the shape of the saturation curve. The three different trends are shown in figure 3.6.

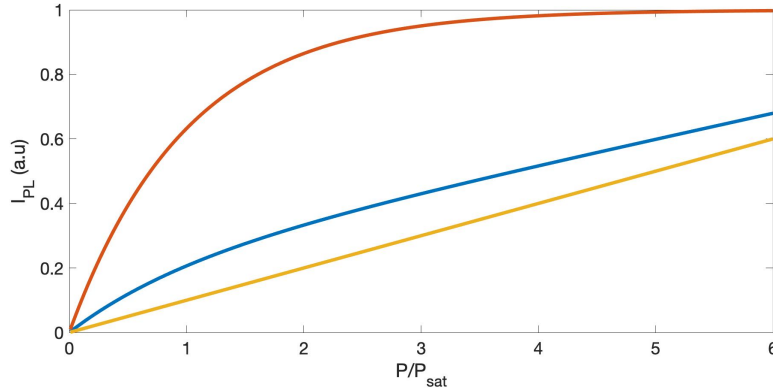


Figure 3.6. Theoretical saturation curve. Red line: saturation curve of a nanocrystal presenting perfect saturation, no multiexciton emission. Yellow line: saturation curve of a nanocrystal without any multiexciton emission quenching processes. Blue line: intermediate case.

Saturation setup

As shown in the complete scheme of the set-up in figure 3.1, to vary the laser power a motorized half-wave plate is used, followed by a beam splitter. The laser beam that comes out of the beam splitter passes through a partially reflecting mirror which allows to send a fraction of the beam on a photodiode. The transmitted beam is used for the confocal microscopy.

3.4 Time-correlated single photon counting technique

In this section I will describe the single photons detection technique. We use a time-correlated single photon counting (TCSPC) system to efficiently measure the arrival times of fluorescence photons. In our case the electronic system consists of a PicoHarp 300 acquisition card together with the PHR 800 4-channel detector router from PicoQuant. The measurements carried out with this technique allow us to derive several quantities of interest: the correlation function of the signal at short time delays, the photoluminescence decay and the photoluminescence versus time.

Let's start with the first quantity. By measuring the temporal correlation between the events given by the detection of a photon, this technique reconstructs the second order autocorrelation function of the typical intensity of the emitter. Once the first photon is detected, the APD generates a pulse which is sent to the electronics, schematized in figure 3.7.

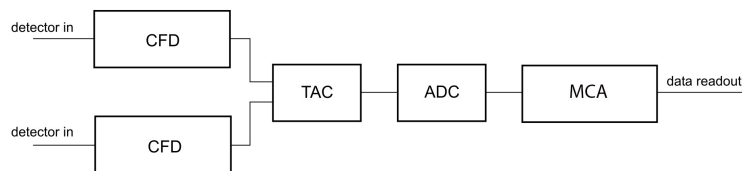


Figure 3.7. Scheme of TCSPC electronics.

The pulse is processed by a *constant fraction discriminator* (CFD) providing a *start* signal. The start signal activates a *Time to Amplitude Converter* (TAC) circuit which is a highly linear integrator generating a voltage ramp over time. The TAC loads a capacitor until the pulse given by a second detection event sends a *stop* signal to the ramp. The signal accumulated in the capacitor, proportional to the time delay between the two detected photons, is digitized by means of an *Analog to Digital Converter* (ADC) and sent to a *multichannel analyzer* (MCA). The MCA constructs a histogram of the number of start-stop coincidences as a function of the time interval between detection events. To build the instogram the entire range of time values is divided into a series of intervals of a certain temporal width, called *bin time*, and the number of events detected during a given bin time is counted. This histogram reproduces, at small delays, the second-order autocorrelation function of the intensity $g^2(\tau)$. If the autocorrelation function displays an antibunching

behavior with a dip at zero delay, we know that we are studying a single emitter. We can observe that to correlate each photon arrival time with the next one it is

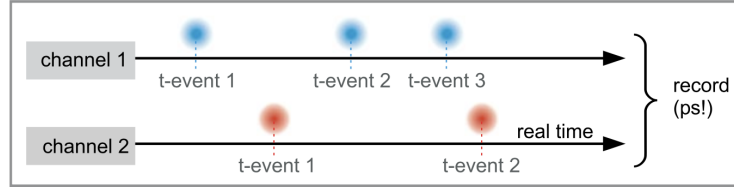


Figure 3.8. Data acquisition mode for antibunching measurement.

fundamental to use the Hanbury-Brown Twiss configuration and, conversely, it is not possible to evaluate the photon statistics $p(n)$ of a quantum state of light with only one detector. In fact, a real detector always has a dead time which does not allow to measure two events if they arrive with a minimum delay. In our case, the APD is blind until the avalanche of electrons produced by a single detection event is quenched and the breakdown potential is recovered. Consequently, if two photons arrive within the detector dead time (typically between 25 and 50 ns) only one pulse can be detected. This limitation is therefore overcome by splitting the photon beam into two arms in the HBT scheme and using two independent detectors, so that the photons arrival time can be correlated between two detectors.

Now let's see how to get the photoluminescence decay and the photoluminescence trace using the TCSPC technique. The TCSPC working scheme remains the same as in figure 3.7 but in this case a synchronization signal (SYNC) is set on the laser, used as a reference, and not on the second APD. In this way, as we can see in figure 3.8, the excitation laser triggers a timer, which is stopped with the detection of a fluorescence photon; this time delay between the excitation of the nanocrystal and the emission of a photon is called *microtime* t . Moreover, for each pulse the absolute arrival time with respect to the beginning of the experiment is registered; this is called *macrotime* T . The microtime t and the macrotime T are labeled to each registered pulse together with the information of which channel (APD) the signal is coming from.

We obtain the photoluminescence decay by building a histogram of the microtime, with a bin width being a multiple of the resolution. We use a bin time of 512 ps. The photoluminescence trace is obtained by building a histogram of the macrotime, counting the number of photons detected during a given bin time. This bin time should be short enough to be able to observe fast intensity fluctuations, but at the same time long enough to appreciate something other than noise. A typical bin time value is 50 ms.

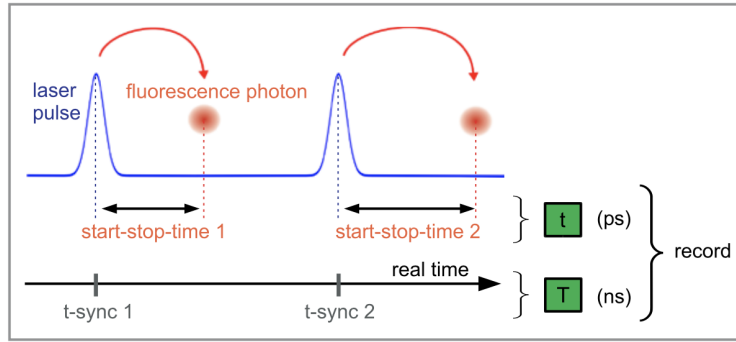


Figure 3.9. Data acquisition mode for photoluminescence decay and trace.

3.5 Noise sources and noise cleaning on $g^2(\tau)$ measurements

We have to consider different sources of noise in our set-up, such as light coming from the room, reflected excitation light and dark counts of the APDs. Light coming from the room can be almost totally removed if measurements are made in a dark room and if the whole detection part of the setup is covered; reflected excitation light can be removed if a spectral filter is used. The dark counts of the APDs correspond, instead, to the intrinsic noise of the detector: the avalanche process can be triggered by thermally-generated carriers within the semiconductor, thus output pulses can be created even if the APD is in complete darkness. The APDs we used have typical dark noise less of 250 counts/s. The noise level on the APDs is controlled before starting measurements.

Background noise affects the g^2 value we get from TCSPC measurements. It is therefore necessary to take into consideration the presence of the background counts in order to clean the g^2 histogram from them. The method we used to correctly perform the $g^2(\tau)$ measurement is explained in Annex A.

3.6 Synthesis and deposition methods

The $CsPbBr_3$ perovskite nanocubes studied in this thesis were synthesized in collaboration with the *Institute de Nanoscience de Paris* (INSP) with a method used for the first time for produced quantum emitters.

The commonly used Protesescu's synthesis procedure illustrated in section 2.4 leads to highly luminescent perovskite-based nanocrystals with bright, spectrally narrow and broadly tunable photoluminescence, particularly appealing for optoelectronic applications such as lasing, photon detection, light-emitting diodes and photovoltaic. However, the nanocrystals obtained with this synthesis procedure cannot be used for single emitter applications in which we are instead interested. Confinement is required to obtain single photon emission properties from a two

level system-like emitter, instead the Pretesescu's method allow to grow bulk like $CsPbBr_3$ cubes without confinement. In fact, according to TEM images in figure 3.10, all dimensions are above the Bohr radius (corresponding to 7 nm for $CsPbBr_3$) and this is made even more clear by the histogram of sizes in the same figure. As a result, the absorption spectrum is poorly structured and the photoluminescence matches the bulk one (515 nm or 2.41 eV).

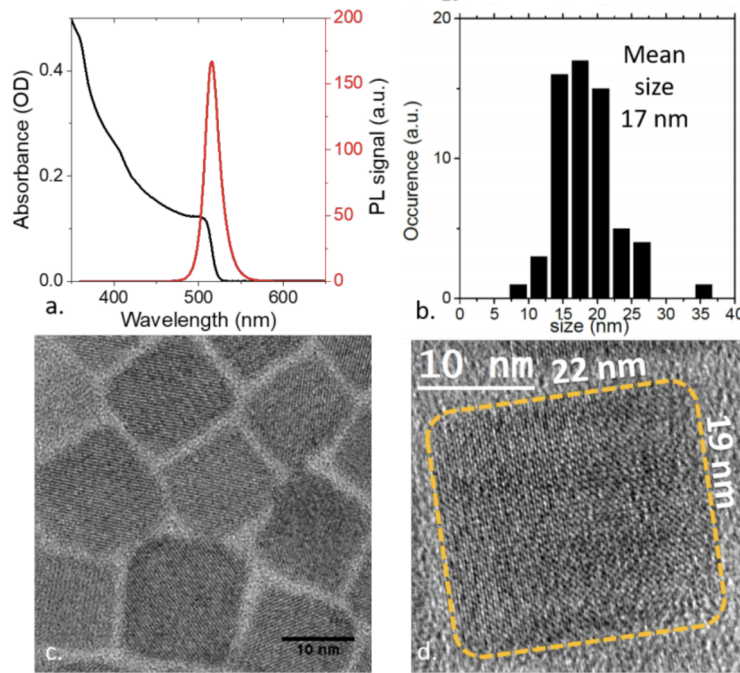


Figure 3.10. a) Absorption and photoluminescence spectra of the material obtained from the Pretesescu's method b) Size histogram determined from TEM image for the $CsPbBr_3$ cube obtained from Pretesescu's method c), d) Respectively TEM and high resolution TEM of $CsPbBr_3$ cube obtained from the Pretesescu's method

In addition to confinement, the nanostructure at which we are interested needs to be sufficiently colloidally stable to avoid aggregation and to allow dilution. The possibility of diluting the colloidal solution without losing stability has indeed great importance, allowing us to isolate the single emitter in order to characterize it or to couple it to photonic devices. The cubes obtained from Pretesescu's method present instead a limited colloidal stability under dilute conditions due to the fact that the alkyl ammonium ligands have strong binding dynamics[148] to the nanocrystals surface.

An alternative solution may be the use of nanoplatelets, which are an other confined form of perovskite material but with the disadvantage that their large lateral extension also leads to a poor colloidal stability. This is why we chose to target small confined nanocubes: this shape combines quantum confinement together with a reasonable colloidal stability. For the growth of $CsPbBr_3$ cube nanocrystals studied

in this thesis, we use a synthesis procedure initially developed for the growth of $CsPbBr_3$ nanosheet[149], in which the nanocubes are a side product of the synthesis.

Compared to the usual Protesescu's procedure, there are three major changes, as described in the recipe in annex B:

1. less cesium oleate is injected in the three-neck flask to favor the growth of a cesium free phase;
2. two additional ligands - *octanoic acid* and *octyl amine* - with saturated alkyl chains are introduced to favor the crystallization of the cesium free phase;
3. the reaction time is extended from several seconds to several minutes to favor the reaction step.

The main product of this synthesis is $CsPbBr_3$ nanoplatelets (NPL) with an absorption peak at 430 nm as shown in figure 3.11. Moreover, there are two additional products: Cs-free Ruddelsden-Popper perovskites and $CsPbBr_3$ nanocubes. The first ones are formed by a plane of lead bromide sandwiched between two planes of ligands with C8 chains and present a clear peak at 398 nm in the absorption spectrum. We are instead interested in the nanocubes, responsible for the small absorption edge from 450 nm to 500 nm shown in the absorption curve³ in the inset of figure 3.11.

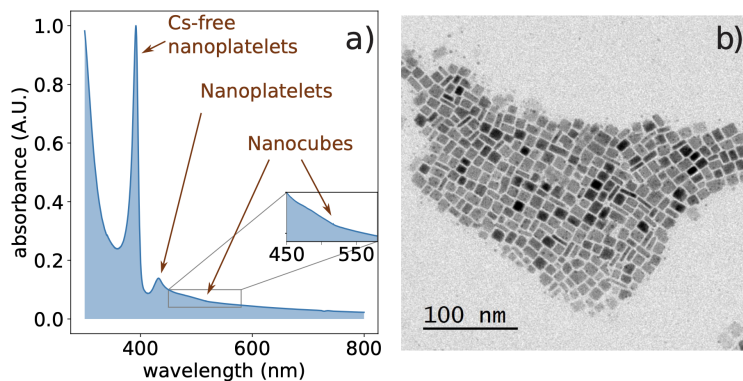


Figure 3.11. a) Absorption spectrum of the products obtained from the synthesis. The inset shows the portion of the spectrum corresponding to nanocubes contribution. b) Transmission electron microscopy image of $CsPbBr_3$ nanocubes responsible for the photoluminescence.

TEM images in figure 3.12 reveals that the lateral extension of the two populations is very different. These particles, being far smaller than the NPLs, can be easily sorted thanks to selective precipitation.

Figure 3.13 shows the structural characterization of the confined cubes. The photoluminescence is blue-shifted compared to the bulk like cube of the Protesescu's

³We can see the signature of these confined cubes as a small change in the slope of the absorption curve.

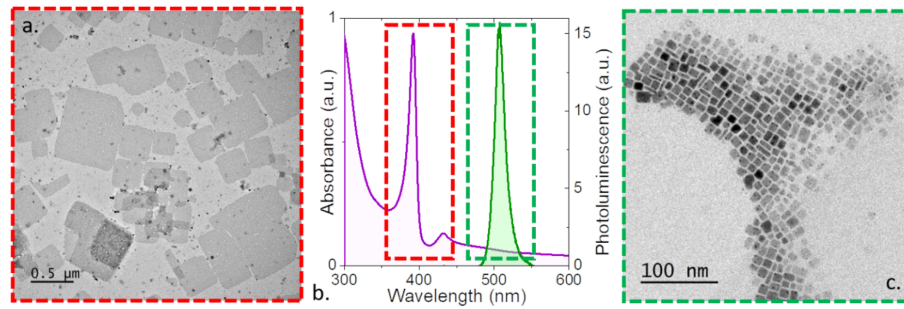


Figure 3.12. a) TEM of the large NPLs presenting absorption below 450 nm and obtained from selective precipitation of the synthesis given in Liu et al. b) Absorption and photoluminescence spectra of the material obtained from the method given in Liu et al. c) TEM of the small confined cube presenting photoluminescence above 450 nm and obtained from selective precipitation of the synthesis given in Liu et al.

method depicted in figure 3.10, with a maximum at 506 nm (2.45 eV). TEM images in the same figure clearly show anisotropic particles whose shape corresponds to NPL with a small aspect ratio (around 3 – 4). Some confined particles lie on the edge while others lie on their main facet: this allows to extract the mean particle thickness (3.6 nm) and lateral extension (11.3 nm), as reported in the histogram in the same figure.

Moreover, the method of fabrication presented allows to obtain higher stability samples which can be excited under optical excitation for more than one hour, as I will illustrate in the next chapter.

To characterize and study the nanocrystals it is necessary to deposit the colloidal solution on a substrate with a concentration that depends on the type of measurement to be made. To investigate the role of the dilution on the stability, for example, it has been necessary to carry out a dilution using toluene as solvent, starting from the most concentrated colloidal solution (typically with a molar concentration between $1\mu\text{M} - 2\mu\text{M}$, up to a dilution of 1 : 50.

For each concentration, the samples are prepared with the *spin-coating method*: $10\mu\text{l}$ of the colloidal solution are deposited on a microscope coverslip (BK7, 180m thick) with a pipette. The coverslip is fixed to a plate by an aspirator and, by spinning the plate, the solution is spread uniformly across the whole surface of the substrate, due to centrifugal force. Moreover, uniform evaporation of the solvent occurs because of rapid rotation. The result is that high volatile component are removed from the coverslip because of the evaporation and the nanocrystals remain on its surface. Although this method makes the colloidal solution more stable, we also investigate the role of the dilution on the stability.

We can consider that the sample is of good quality if:

- the nanoparticles are distant a couple of microns enough from each other;
- the sample is mostly made of single nanocrystals and not clusters of nanocrystals.

Indeed the nanocrystals have to be at least a couple of microns apart in order to

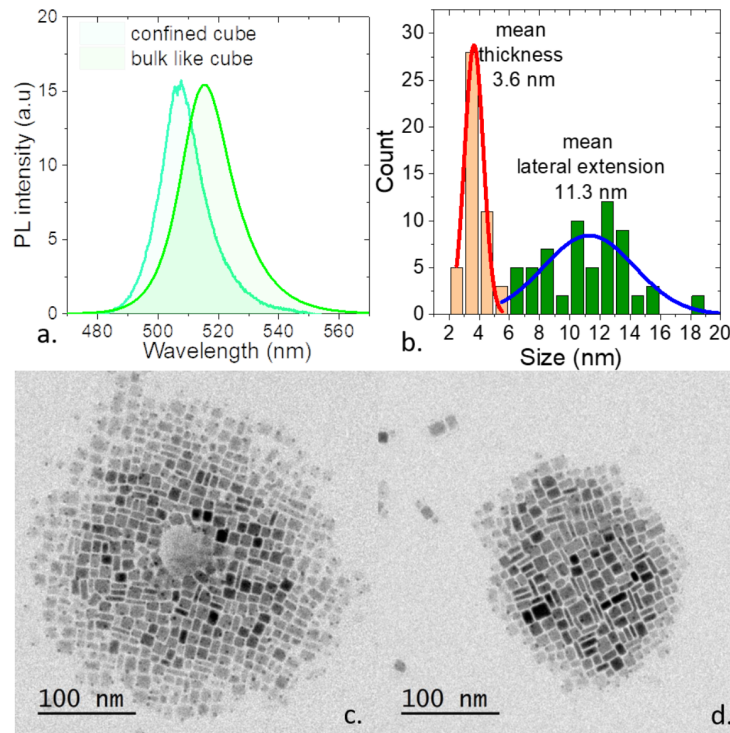


Figure 3.13. a) Photoluminescence spectra for confined cubes used in this work and for the bulk like CsPbBr₃ cubes from the Protesescu's method. b) The size histogram for our cubes shows two peaks which are fitted by two gaussians leading to a mean thickness of 3.6 nm and a mean lateral extension of 11.3 nm. c) and d) are TEM images of the confined cubes.

be sure to excite only one at a time by the laser spot. In our case we have an average distance of $10\mu\text{m}$ between the nanoparticles in the concentrated sample and this value clearly increases in samples where dilutions have been made. Moreover, having at least 50% of the nanoparticles that are single nanocrystals and not clusters is a good situation in order not to lose time searching for single particles during measurements. In our concentrated samples we have 70% of single nanocrystals (not clusters) and 85% of these have a single photon emission, as demonstrated in section 4.6.

Chapter 4

Experimental study of $CsPbBr_3$ nanocrystals

In this chapter I will present the results obtained from the characterization of the optical properties of $CsPbBr_3$ nanocrystals, from the study of the effect of dilution on their photostability and from the analysis of blinking and their single photon emission.

4.1 Emission spectra

A typical emission spectrum of our $CsPbBr_3$ nanocrystals is shown in Figure 4.1. It is characterized by a central wavelength of 500 nm and a full width at half maximum (FWHM) of about 15 nm.

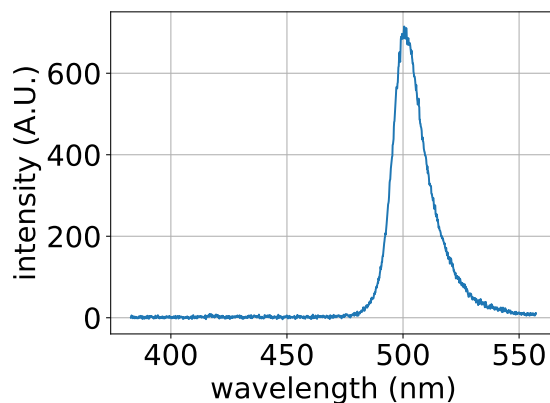


Figure 4.1. Typical emission spectrum of the $CsPbBr_3$ nanocrystals.

We carried out a systematic study of the spectra of 24 emitters, obtaining the distribution of the emitted wavelengths and the corresponding FWHM distribution shown in figures 4.2 and 4.3 respectively. In these distributions two peaks with central emission wavelength at 485 nm and 510 nm respectively are visible. The

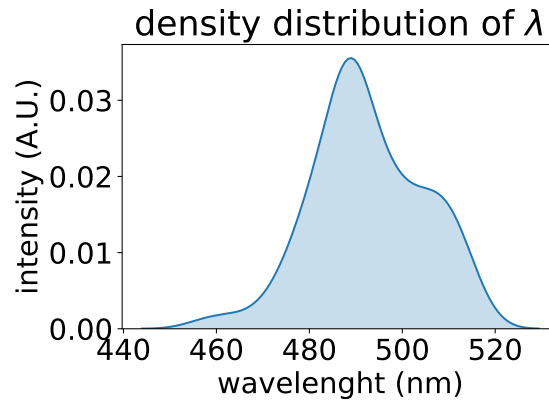


Figure 4.2. Central wavelength distribution of the emission for a sample of 24 emitters.

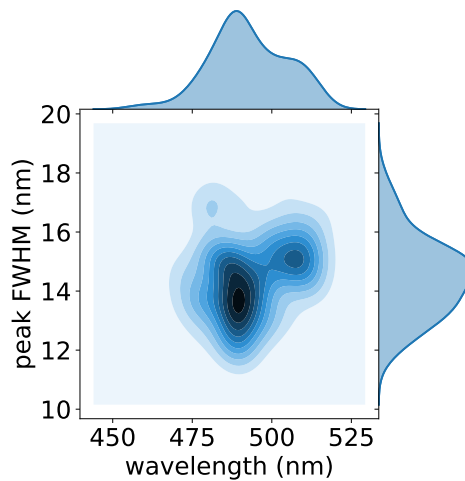


Figure 4.3. FWHM distribution of the emission for a sample of 24 emitters.

mean FWHM of the emitted light is about 14 nm for the first peak and 15 nm for the second one. In literature a mean FWHM of 20 nm for the bulk perovskite emission wavelength, without quantum confinement, at about 520 nm is reported [30]. In comparison with this data, we attribute the emission with a mean FWHM of 14 nm to small size nanocubes with slight quantum confinement and the emission with a mean FWHM of 15 nm to large size nanocubes for which the confinement is mostly absent. In section 4.6 I will show that these small size nanocubes exhibit strongly antibunched emission, demonstrating the crucial role of the charge confinement on their quantum properties.

4.2 Saturation measurement

For each of the 24 emitters studied, we measured the emitted intensity as a function of the excitation power, subtracting the background from the experimental data. As explained in section 3.3, the data were fitted using the saturation function obtained in eq.3.17, in order to obtain the saturation power P_{sat} and consequently a reference for the characterization of the different emitters. A typical saturation curve is shown in figure 4.4. To minimize the effect of the blinking on the data analysis, multiple measurements are taken for each experimental power in the graph, and only the one with the strongest emission is kept. We observed a median P_{sat} of 62 nW.

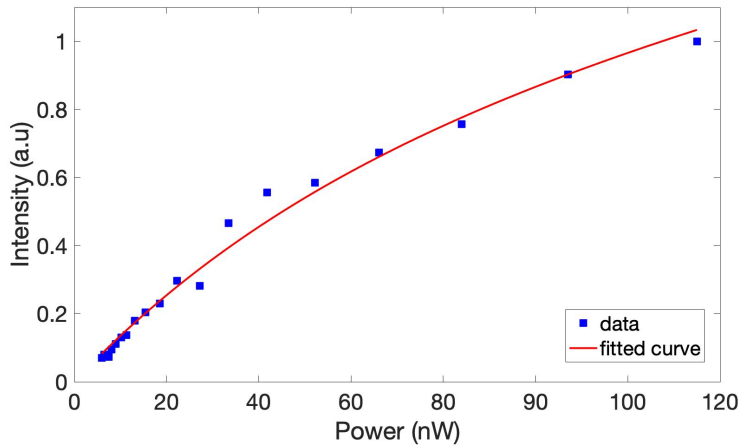


Figure 4.4. Saturation measurement of a single nanocrystal. The blue squares are the experimental data while the red line is the fitted function from equation 3.17.

The presence of a bi-exciton component, which is deduced from the presence of a non-perfect saturation curve as explained in section 3.3, indicates that the correlation function $g^2(0)$ will depend on the excitation power. To show this behavior we also performed g^2 measurements as a function of the excitation power and we observed a slight dependence of the g^2 value from the excitation power. An example of this behavior is illustrated in figure 4.5.

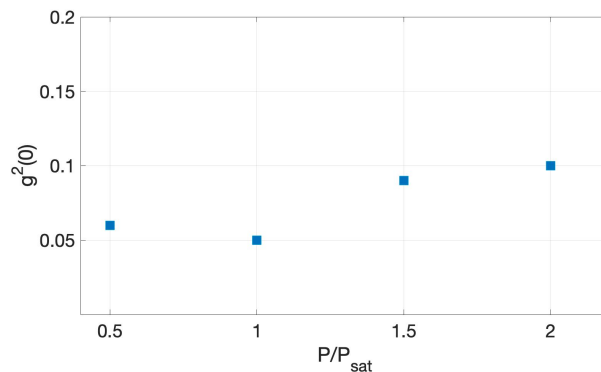


Figure 4.5. Dependence of the $g^2(0)$ on the normalized excitation power.

4.3 Effect of the sample dilution on the photobleaching

As explained in section 2.4, lead halides perovskite nanocrystals suffer from fast photo-bleaching in presence of a combination of moisture, oxygen and light. Overcoming their emission instability is a critical challenge and the subject of an intense research [150]. One possible way to evaluate the photostability of nanocrystals is to monitor their photoluminescence over time [141]. Generally $CsPbBr_3$ nanocrystals - spin-coated onto a glass substrate and in direct contact with air - bleach after a couple of minutes and, even when they are encapsulated with polymers, the longest measurement time recorded in the literature is 100 s [78]. Moreover, taking consecutive spectra of $CsPbBr_3$ emitters, a shift of the central emission peak of more than 10 nm in a few tens of seconds is generally observed [78] [151] [29]. The observed spectral drift has been attributed to the degradation of the nanocrystals, resulting in a progressive reduction of their sizes.

With the synthesis method we used, described in Annex B, it is possible to obtain a significant improvement in the photostability of the emitters under illumination, resulting in the possibility of collecting luminescence for more than one hour with strongly reduced bleaching effects.

We studied the effect of illumination on six samples of different dilutions. These dilutions were carried out in toluene starting from the concentrated solution (with a molar concentration of $1 \mu\text{M}$), up to a dilution of 1 : 50, as shown in figure 4.6. We started by analyzing the highest concentration sample. First, we made sure that this high concentration still allowed us to individually target each emitter so that we could conduct a study on the individual emitter. Once the emitter to be characterized was chosen, its suitability was verified: a photoluminescence spectrum was taken to verify the presence of a single narrow peak¹, then a saturation measurement was carried out to determine the saturation intensity together with an antibunching measurement to verify its nature as a single photon emitter, that is the object we are interested. The selected emitter was excited at the saturation intensity for two hours while its emission spectrum was collected every 5 minutes. In figure 4.7 it is possible to observe the evolution of the normalized emission spectra with respect to time. A blue-shift in the central emission peak of less than 10 nm after two hours is observed.

The blue shift is a sign of emitter's degradation but in our case it has been observed on a time scale of two orders of magnitude longer in previous works, thus indicating a remarkable stability of our emitters. The best result reported in the literature is indeed a blueshift of 16 nm in 300 s [29].

The robustness that characterizes this high concentration sample, however drops fast when we make a dilution. Since our ultimate goal is to couple a single emitter to a tapered optical nanofiber to develop an integrated single photon source, it is necessary to use a strongly diluted sample. We are therefore interested in investigating the stability of emitters as their concentration in the solution changes. For

¹The presence of a single and narrow peak in the spectrum excludes that we are observing a cluster of emitters.



Figure 4.6. Different dilutions carried out in toluene starting from the concentrated solution.

this purpose, each of the six samples with increasing dilution is illuminated with the LED set to its full irradiance (25 W). We recorded a video of the illuminated area, taking a frame every 20 seconds for 20 minutes. In this way, by analyzing each frame of the video, it is possible to estimate the number of nanocrystals that are still emitting with respect to the first frame. Figure 4.8 shows the resistance curves obtained.

The initial slope of each curve gives information on the average lifetime of the emitters under illumination. The high concentration sample (1 : 1) is robust and highly photostable; in fact after 20 minutes more than half of the nanocrystals are still emitting. The samples with greater dilutions (from 1 : 2 to 1 : 50) have instead bleached after 5 minutes. We can see that the (1:50) solution appears better than (1 : 2) one. This is due to the fact that for increasing dilutions an increasing number of aggregates is observed. Although with our analysis it is possible to filter out most of the clusters, with the post-selection is not possible to distinguish the small

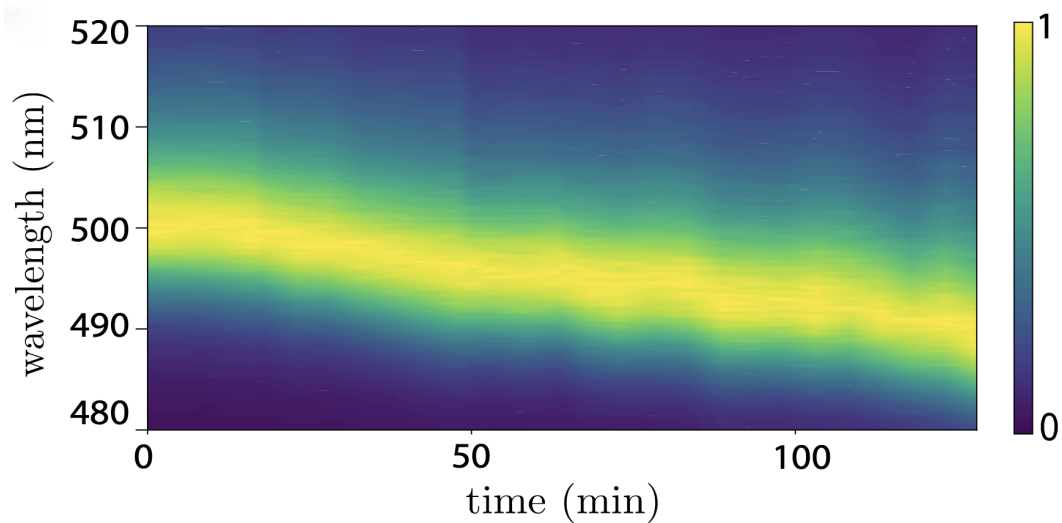


Figure 4.7. Evolution with respect to time of the emission wavelength of a single perovskite NC excited at the saturation intensity. Each spectrum is normalized to the maximum intensity.

aggregates from the single emitters and therefore to eliminate them. These small residual aggregates last for longer time, leading to an overestimation of the number of particles still active after a given time. We attribute the effect of the diminution of the photostability with the dilution to the dynamic bonding of the ligand to the perovskite nanocrystal surface. Under dilute conditions, there is no longer a balance between bound and unbound ligands in the solution: the fraction of the bound ligands decreases as they can hardly find the surface of the nanocrystal. As a result, the dilution process leads to poorly passivated nanocrystals which can easily bleach.

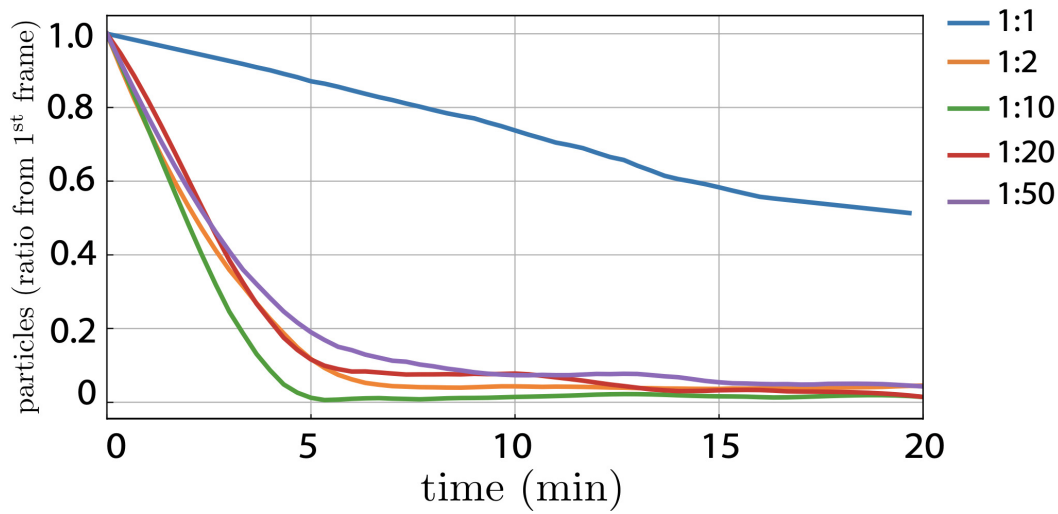


Figure 4.8. Percentage of nanocrystals still emitting after a certain time under strong illumination for 1 : 1, 1 : 2, 1 : 10, 1 : 20, 1 : 50 dilutions.

4.4 Blinking characterization

The emitted intensity of a nanocrystal is not constant in time but tends to fluctuate between high and low intensity states on time scales spanning from microseconds to hundreds of seconds due to the aforementioned phenomenon of blinking. As explained in section 1.7, this behavior has been reported in literature for several kinds of quantum emitters, an example of which is shown in figure 4.9.

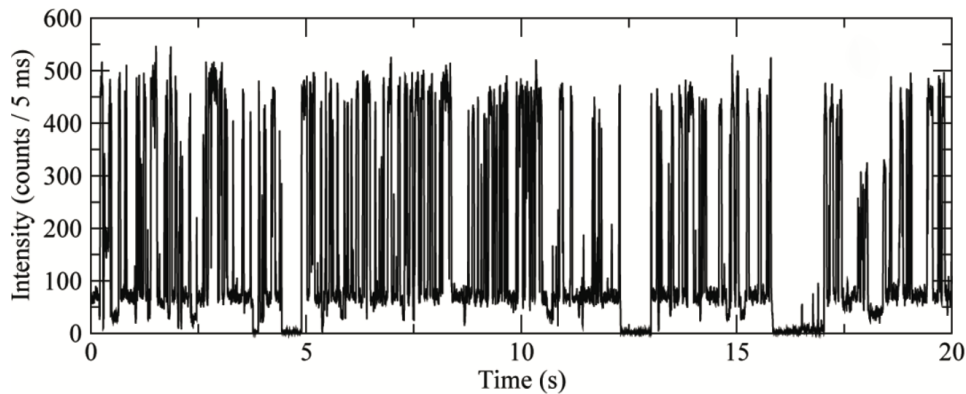


Figure 4.9. Typical blinking behavior reported for a single CdSe/CdS nanocrystal. Figure taken from reference [152].

The details of the underlying mechanism responsible for blinking are still highly debated, but it is generally agreed that non-fluorescence periods during blinking are directly result of charge carrier trapping. This is a process that affects charge transport and recombination in nanocrystals and it consists in localization of an

electron or a hole at lattice defects within the crystal structure or at unsaturated bonds on the nanocrystal surface atoms. In the case of semiconductor nanocrystals, these trap states create energy levels within the semiconductor band gap. Typical timescales for removal of a charge from the conduction band to a trap state are one to tens of picoseconds, instead lifetimes of trap states range from nanoseconds to microseconds. When the charge is trapped for long time, the nanocrystal is said to be in a *charge-separated state*: one charge in a localized trap state and its counterpart delocalized inside the nanocrystal.

Two models have been developed in literature to link charge trapping with OFF periods, we will refer to these models by calling them *model A* and *model B*.

Model A

Charge trapping leaves nanocrystals in a charge-separate state. The unpaired charge in the core induces a low fluorescence quantum yield because most of the electron-hole (e-h) pairs recombine non-radiatively with the extra charge by an effect called *Auger effect*. As already explained, it is an efficient non-radiative recombination pathway strictly connected to the strong quantum confinement. It consists in an energy transfer from an e-h pair to a third particle (electron, hole or exciton) because of the Coulomb interaction; in our case the energy is transferred from the new generated excitons to the spectator charge. The low fluorescence state lasts for a time dictated by the lifetime of the trapped charge. Once the trapped charge recombines with its countercharge, the low fluorescence period is over.

In figure 4.10 the different steps are shown:

- ON states are the result of continuous cycling photon absorption to create an exciton, followed by radiative recombination of e-h pair.
- ON to OFF switching occurs when charge carrier goes to a trap state, leaving a delocalized charge of opposite sign inside the nanocrystal.
- During OFF states, despite the subsequent absorption cycles, the resulting charged nanocrystal remains usually non-fluorescent or very low fluorescent, because emission is quenched by a competition between the fast non-radiative Auger recombination and radiative recombinations.
- OFF to ON switching occurs when the trapped charge returns into the nanocrystal and recombines with its counterpart.

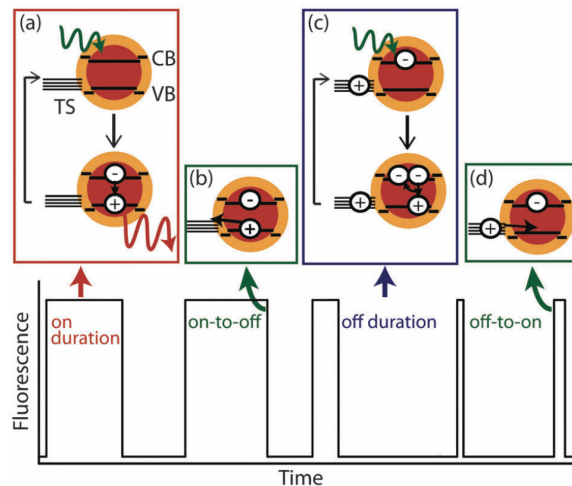


Figure 4.10. Schematic depiction of blinking model A. The nanocrystal conduction band edge (CB), valence band edge (VB), and surface trap states (TS) are labeled. Figure taken from reference [153]

Model B

Model B do not require long-lived traps or Auger recombination [154] and there is not a permanent charging of the core during low fluorescence periods. During an off state a carrier, i.e a hole, is predicted to trap in a state with a lifetime of $\sim 1\mu s$ and then to recombine non-radiatively with the unpaired one, i.e an electron, in the nanocrystal conduction band. The nanocrystal returns to the neutral ground state rapidly following each excitation event. The trapping rate fluctuates in time and the nanocrystal remains in an off state for the duration that the trapping rate is much faster than the radiative recombination rate [155]. The result is that blinking is caused by time-dependent fluctuations of that trapping rate: the off duration is determined by the time the trapping rate dominates the radiative recombination rate and not by the lifetime of the trapped charge - as in model A - and the photoluminescence intensity in this case is not determined by the competition between radiative and non-radiative rate but by the one between radiative and trapping rate [153]. In figure 4.11 the different steps are shown:

- ON states occur when the trapping rate is considerably slower than the fluorescence rate; the nanocrystal cycles between photon absorption to create an exciton that recombines radiatively.
- ON to OFF switching occurs when the trapping rate becomes faster than the fluorescence rate.
- During OFF states, the nanocrystal cycles between photon absorption to create an exciton, fast removal of the charge to a trap state and non radiative recombination with the counterpart charge in conduction band.
- OFF to ON switching occurs when the trapping rate becomes very slow again.

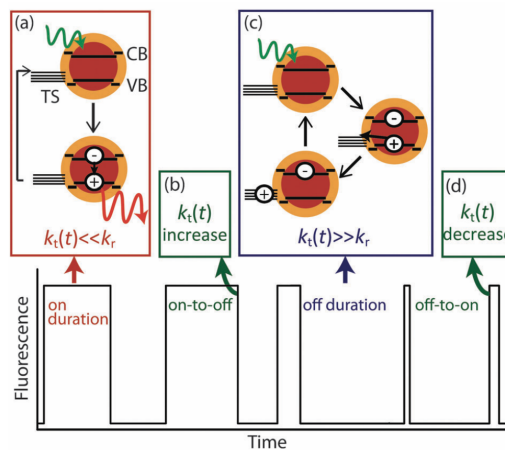


Figure 4.11. Schematic description of blinking model B, where k_t is the trapping rate and k_f the recombination rate. The nanocrystal conduction band edge (CB), valence band edge (VB), and surface trap states (TS) are labeled. Figure taken from reference [153].

A well established method to experimentally distinguish between type A and type B blinking is to study the spontaneous emission lifetime dependence on the emission intensity. Indeed in type A blinking the lifetime is expected to depend on the emission intensity [155] while in type B blinking the lifetime should not depend on the intensity [156].

We can explain this behavior as follow. As seen, in type A blinking ON and OFF periods correspond to a neutral nanocrystal and a charged nanocrystal, respectively, and this charging/discharging causes the random switching between the two luminescence states. The dynamic of the bright state is dominated by radiative recombination of the neutral exciton, which has a spontaneous emission lifetime (~ 15 nanoseconds in perovskite nanocrystals [29]). For the charge exciton the three particle Auger recombination opens a fast, non-radiative channel, resulting in a shorter lifetime (of the order of the nanosecond [29]) and a reduced photoluminescence quantum yield. For these reasons this model predicts correlated fluctuations of the photoluminescence intensity and lifetime, as observed experimentally [157] [158] [152]. In type B blinking, instead, we observed periods of low luminescence intensity that are not accompanied by a significant shortening of the photoluminescence lifetime [153]. Indeed, the photoluminescence intensity fluctuates between ON and OFF states, but the photoluminescence lifetime remains constant [155]. This is explained by the fact that the low fluorescence quantum yield of the OFF state is the result of the fast removal of a carrier (i.e. a hole) to a trap state and not a result of Auger recombination.

It is possible that no clear ON-OFF transitions are observable and that the nanocrystal shows a photoluminescence trajectory with a quasi-continuous distribution of intensity as a function of time, as showed in figure 4.12b. In this case it is more appropriate to describe the behavior of the emitter in terms of *flickering*. Flickering occurs when the switching time between bright and low photoluminescence states is too short with respect to the experimental binning of the photoluminescence time-trace curve. For $CsPbBr_3$, for example, the switching usually occurs on a microsecond time scale [159], instead the chosen binning of the time-trace curve is typically of tens of milliseconds. In this case the data within each bin represents an average intensity, therefore it is not possible to completely distinguish the bright and low states. Our emitters, like the vast majority of perovskite nanocrystals reported in literature [160] [161], show a clear flickering behavior in their emission time, as showed in figure 4.13. trace The flickering characterizes most of the perovskite nanocrystals reported in the literature [29] [160] including our emitters.

To understand better what type of blinking characterizes the emitters studied, we therefore have studied the dependence of the spontaneous emission lifetime on the emission intensity.

Figure 4.13 shows the timetrace that we have obtained making a 15 minutes measurement on a single nanocrystal with the TCSPC technique explained in section 3.4. The signal is binned with a binning time of 50ms. Interestingly, the nanocrystal's emission is characterized by a reduced blinking with respect to the typical behavior of this kind of perovskites reported in literature. The emitter was used for other kind of measurements after this one, and lasted for more than one hour.

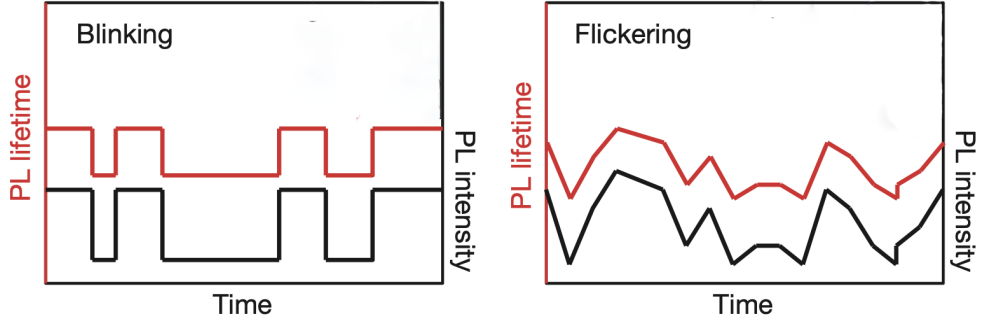


Figure 4.12. A-type blinking and flickering.

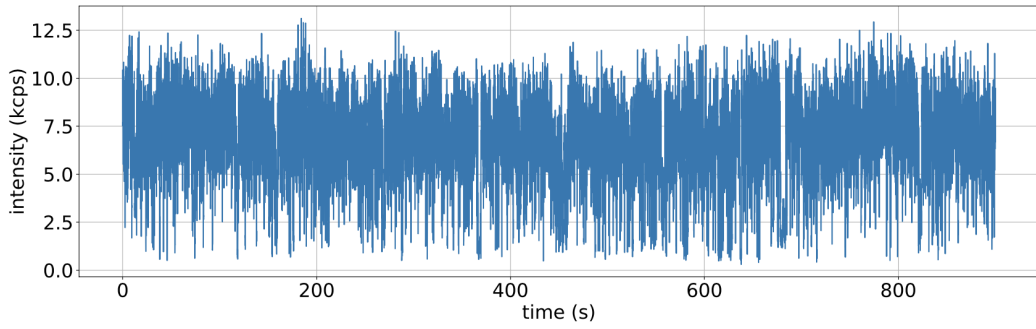


Figure 4.13. Time trace of a single nanocrystal, performed with a binning of 50ms.

We then fit the luminescence decay obtained with the TCSPC technique, showed in figure 4.14, with a triple-exponential decay model:

$$A_1 e^{-\frac{t-t_0}{\tau_1}} + A_2 e^{-\frac{t-t_0}{\tau_2}} + A_3 e^{-\frac{t-t_0}{\tau_3}} + B \quad (4.1)$$

where the three different lifetimes, τ_1 , τ_2 and τ_3 , correspond respectively to the neutral, the charged, and the biexciton emission states [160]. In eq. 4.14 t_0 represents the pulse arrival time, A_i are the amplitudes of each decay component and B is an offset that takes into account the dark counts. As shown in figure 4.14, the fitting procedure shows a good agreement with the experimental data and we obtain lifetimes of 14.7 ns, 6.1 ns and 1.4 ns for the neutral, charged and biexciton emission states, respectively.

We can now study the correlation between photoluminescence intensities and lifetimes. In figure 4.15 a zoom of the blinking trace and the average lifetime versus time are reported. It is possible to observe qualitatively a correlation between the two curves and this indicates the presence of a type A blinking for these emitters.

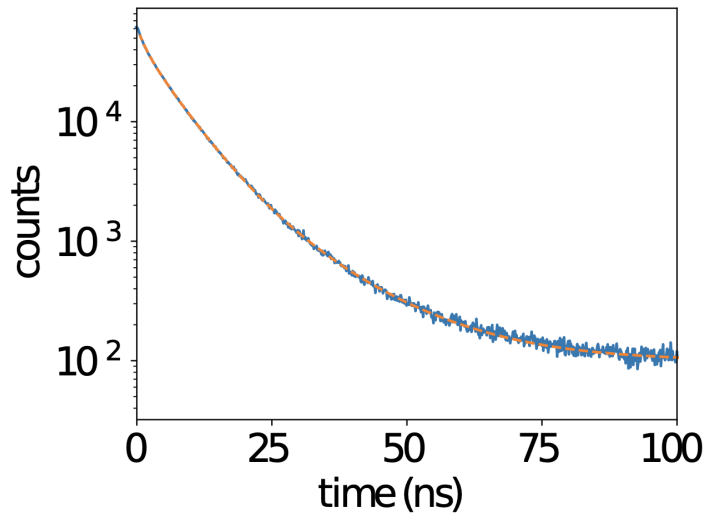


Figure 4.14. Lifetime of a single nanocrystal, fitted with a triple-exponential decay model. We obtain 1.4 ns, 6.1 ns and 14.7 ns, corresponding respectively to the lifetimes of the biexciton, charged and neutral emission states.

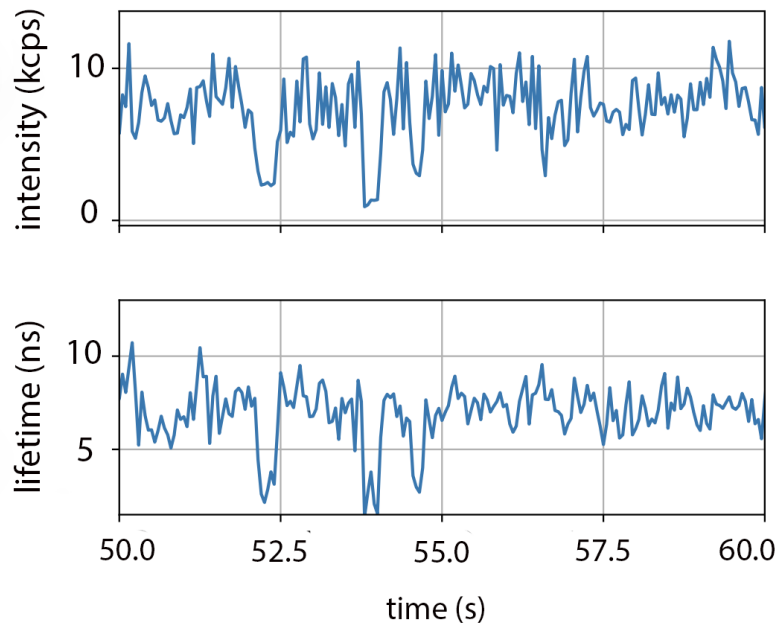


Figure 4.15. Blinking trace (upper graph) and lifetime (lower graph) of a single nanocrystal.

An other useful tool for the quantitative analysis of correlations between photoluminescence intensities and lifetimes during fluctuations is the *fluorescence lifetime-intensity distribution* (FLID) representation [162] [29] [155]. In this representation, the probability of occupying a given state in the two-dimensional lifetime–intensity

space is shown by the color variation from blue to red as the probability increases. In figure 4.16 FLIDs images are shown, corresponding to an excitation intensity of $0.5P_{sat}$ and $2P_{sat}$ respectively, obtained with a bin size of 50 ms. In the FLIDs images, the area corresponding to 50% and 68% probability of emission are delimited with dark curves, respectively the inner one and the outer one. It is thus possible to observe a strong correlation between the photoluminescence intensity and the photoluminescence lifetime during the fluctuations, in agreement with the A-type blinking model.

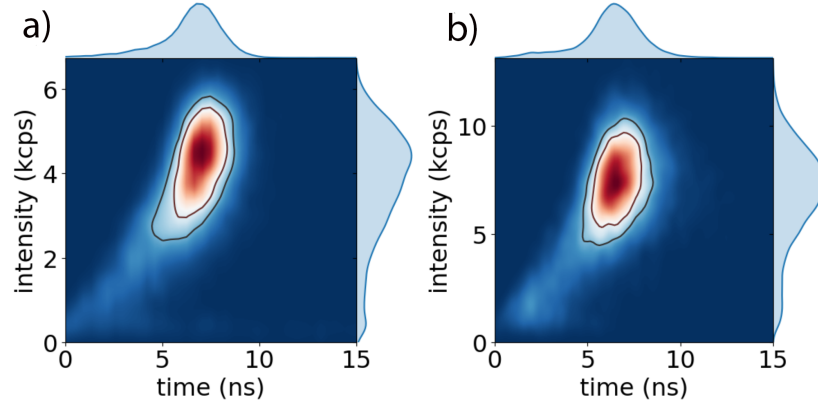


Figure 4.16. Fluorescence lifetime-intensity distribution (FLID) images of a single emitter, excited at half (a) and twice (b) the saturation intensity.. The closed curves contains 50% (inner one) and 68% (outer one) of the occurrences.

Furthermore, in our case the perovskite nanocrystals show a remarkable stability of the bright state emission with the increase of the excitation power, unlike previous works[29] that showed a predominance of the low state emission for high excitation powers and a significant decrease of the emission intensity, as reported in figure 4.17.

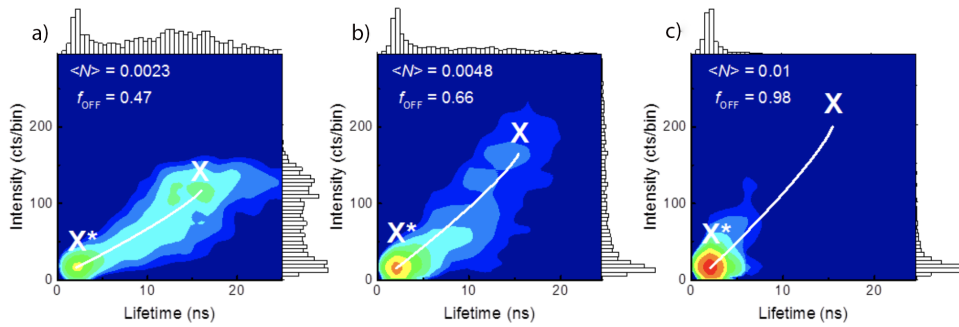


Figure 4.17. Fluorescence lifetime-intensity distribution (FLID) images reported by *Park et al.*[29] for increasing excitation power. The color change from blue to red corresponds to increasing probability of occurrence of a given state in the $I_{PL}-\tau_{PL}$ space, showing a predominance of the low state emission for high excitation powers and a significant decrease of the emission intensity.

4.5 Polarization measurement

In figure 4.18 a typical polarization measurement is shown. The data are obtained and analyzed according the method explained in section 3.2. The curve has a mean value of 0.5 due to the fact that, as explained in section 3.2, it is normalized by the total intensity detected on both the photodiodes in the polarization setup, in order to account for fluctuations due to the blinking. Fitting the data with eq 3.6, we can extract the Stokes parameters:

$$S = \begin{Bmatrix} S_0 \\ S_1 \\ S_2 \\ S_3 \end{Bmatrix} = \begin{Bmatrix} 0.9390 \pm 0.0475 \\ 0.1629 \pm 0.0558 \\ -0.1484 \pm 0.0558 \\ 0.0320 \pm 0.0279 \end{Bmatrix} \quad (4.2)$$

According to equation 3.3, we then obtain a degree of polarization of $P = 23\%$.

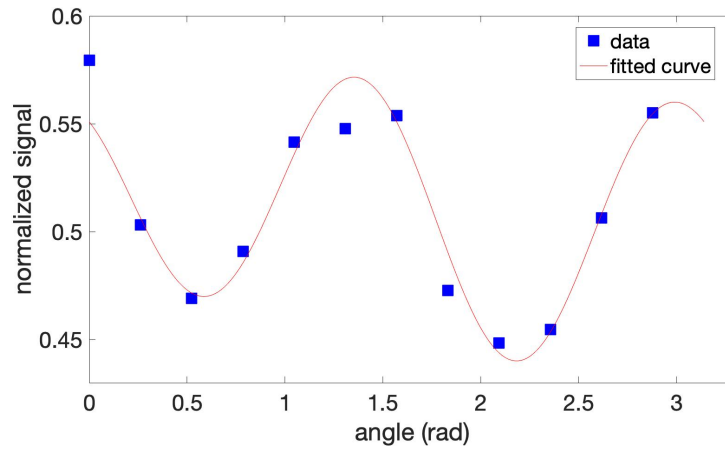


Figure 4.18. Typical polarization measurement.

The studied nanocrystals are therefore slightly polarized. This is in agreement with the results reported in the literature for $CsPbBr_3$ perovskite nanocubes[141][116] and can be explained by their symmetrical crystal structure. As showed in a recent study on the polarization properties of the $CsPbX_3$ perovskites[163], the presence of polarization depends indeed on the symmetry of the crystal structure and different degrees of polarization are observed as the halide varies, as shown in figure 4.19. The $CsPbBr_3$ perovskite belongs to cubic crystal structure while, for example, $CsPbI_3$ quantum dots are distorted from the cubic structure due to the bigger iodine atom[113][164]. The $CsPbI_3$ distorted cubic structure breaks the space inversion symmetry and the resulted asymmetrical structure would be responsible for the polarization properties of this compound[165]. For $CsPbBr_3$ nanocubes this does not happen due to the absence of anisotropies.

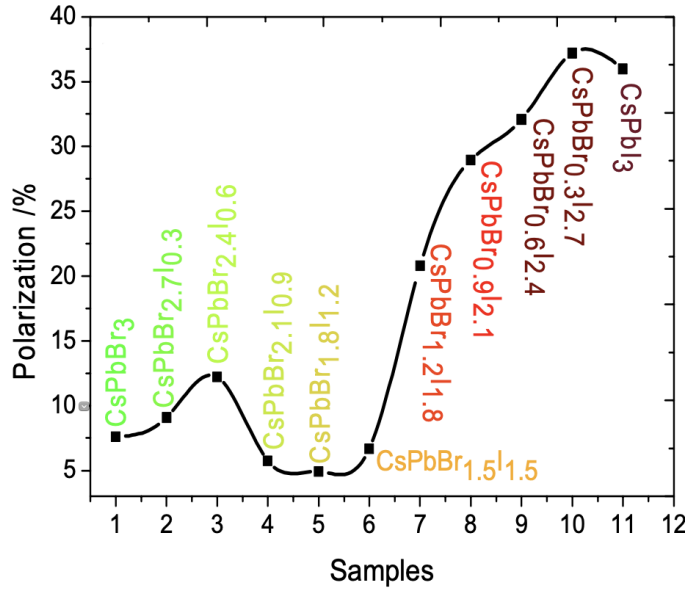


Figure 4.19. Polarization of different $CsPbX_3$ perovskites. Figure reported from reference [163].

4.6 Quantum properties

To verify the nanocrystals' nature as single photon emitters and to characterize their quantum emission, we measured the second order autocorrelation function $g^2(0)$ using the Hanbury Brown and Twiss setup and recording the data with the time tagged time-resolved method using the TCSPC technique, as explained in section 3.4. To easily compare the $g^2(0)$ values obtained for different emitters, all the antibunching measurements have been performed at the saturation power. With the TCSPC technique is therefore possible to obtain the histogram of the relative arrival times of the photons, such as the one presented in figure 4.20.

In general we have that, due to blinking, the autocorrelation function's peaks close to the 0 delay peak are higher than 1, instead for large delays compared to the characteristics blinking time they tend to 1, as showed in figure 4.21. Therefore, using an established procedure in the literature [166] [167], the histogram has been normalized by setting the mean height of the peaks with $\tau \simeq 10ms$ to be 1.

The background of this type of measures is mainly given by the noise of the APDs and it has been subtracted from the experimental data following the procedure explained in section 3.5.

For the measure reported in figure 4.20, a value of g^2 at $\tau = 0$ delay of 0.02 was obtained. This value, being well below the value 0.5, demonstrates the presence of single photon emission. On a sample of 24 emitters, the 50% of them show an excellent single photon emission, presenting a value of $g^2(0) < 0.2$. The $CsPbBr_3$ nanocrystals studied therefore exhibit a single photon emission quality comparable with other commonly used room temperature single photon emitters, such as InGaN

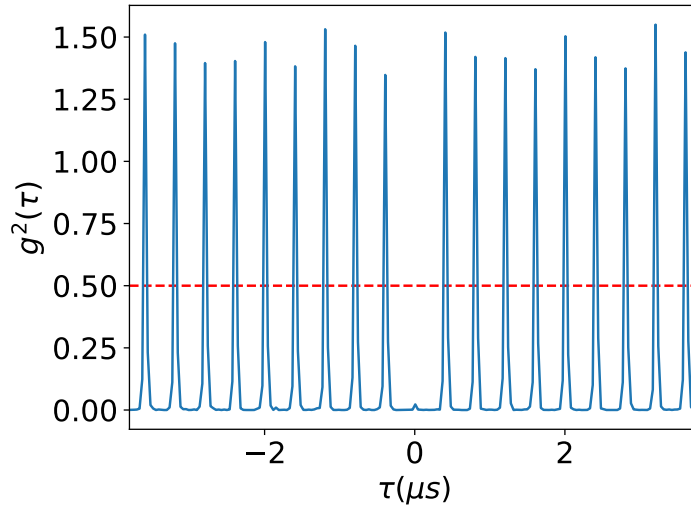


Figure 4.20. $g^2(0)$ function of a single nanocrystal emitting high quality single photons, measured with a repetition rate of 2.5 MHz.

quantum dots, NV defects in diamonds and CdS/CdSe dot in rod.

The $g^2(0)$ measurements made on the sample of 24 emitters were then analyzed as a function of the central emission wavelength, as shown in figure 4.22. Each experimental point in the figure represents a different emitter and all the emitters are excited at their saturation intensity. In this distribution it is possible to observe that for longer wavelengths the value of the second order autocorrelation function degrades. In particular, the measures characterized by a central emission wavelength bigger than 505 nm show a value of $g^2(0)$ bigger than 0.5, no longer presenting antibunching. We can explain this behavior considering that as the size of the nanocrystals increases, quantum confinement decreases and the emission wavelength increases, reducing the quality of the single photon emission.

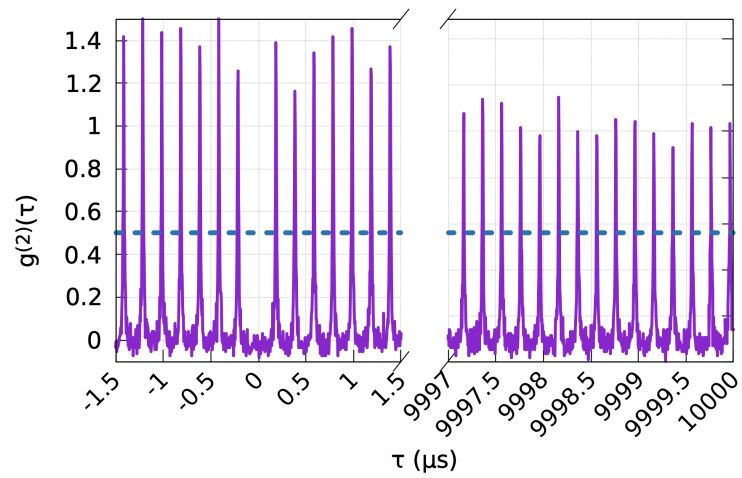


Figure 4.21. Measurement of the autocorrelation function $g^2(=)$ of a single perovskite nanocrystal, showing clear single photon emission. The $g^2(0)$ is shown around $\tau \simeq 0ms$, where peaks are higher than 1 and for $\tau \simeq 10ms$ where they tend to 1. The blue line indicates the value of $g^2(0)$ below which there is single photon emission.

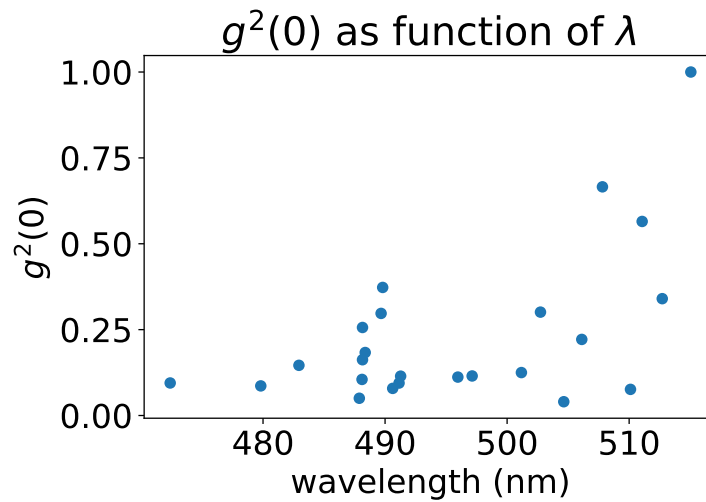


Figure 4.22. Measured $g^2(0)$ values as a function of the central wavelength of the emission of the nanocrystals. All the emitters were excited at their saturation intensity.

Chapter 5

Nanofiber integration

In this chapter I will describe the first realization of coupling of a single $CsPbBr_3$ perovskite nanocube with an optical tapered nanofiber, resulting in a prototype of an hybrid nanophotonic device for quantum-technologies-oriented applications[168]. I will start by describing the propagation of light within an optical fiber, without the intention to be exhaustive but with an emphasis on the aspects necessary for understanding the experimental work. Then I will illustrate the manufacturing procedure to obtain an optical nanofiber and how particles are deposited on that nanofiber. Finally I will present the results of the experimental measurements.

5.1 Optical nanofibers

An optical nanofiber [169] is a cylindrical nonplanar waveguide, generally made of glass and transparent in the visible wavelength range. Its diameter is typically less than the wavelength of the guided light. In the visible domain - to which the *optical* adjective refers - this corresponds to a size of a few hundred nanometers. This object can be schematized by a cylindrical dielectric core with refractive index n_1 and radius a and a cladding with smaller refractive index n_2 . In our case $n_2 = 1$, as the role of the cladding is played by the air surrounding it. The nanofiber is connected on both sides to the standard fiber by a transition zone with a very gentle slope, as showed in figure 5.1.

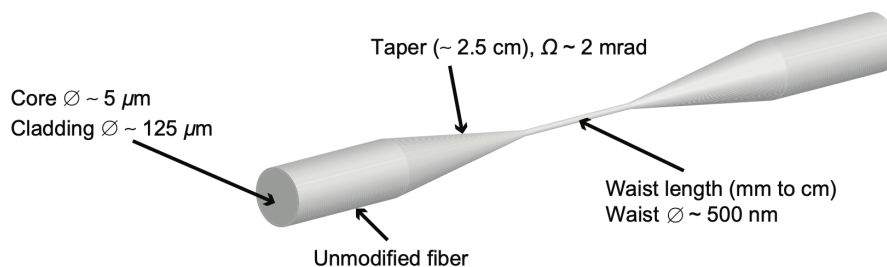


Figure 5.1. Illustration of a typical tapered nanofiber. Figure taken from reference [169].

Optical nanofibers offer several advantages:

- **strong confinement of the electromagnetic field** over the whole fiber length[170];
- **intense evanescent field in the vicinity of the fiber**, which enables the coupling of the light emitted by a nano-emitter located nearby directly into the nanofiber, obtaining a compact and integrated single photon source[171];
- **high transmission** offered by the manufacturing method[172]. In particular, our nanofibers are obtained by stretching a standard optical fiber while heating it in order to reduce its diameter to some hundreds of nanometers. An adiabatic transition between the standard fiber part and the nanofiber region allows an efficient light transmission of the whole system, moreover the glass malleability ensures low surface roughness.
- **great versatility** in terms of connectivity to other systems, demonstrated by the growing importance that such hybrid systems are acquiring in quantum optics and quantum information[2] [173] [174].

5.2 Light propagation in an optical fiber

In this section I will explain how to obtain the guided modes for a step-index optical fiber¹ starting from Maxwell's equations; then I will illustrate the properties of the fundamental mode we are interested in.

5.2.1 Nanofiber electromagnetic modes

In an inhomogeneous dielectric medium², as in the case of a nanofiber, the vector wave equation derived from Maxwell's equations is given by[175]:

$$\nabla^2 \vec{E} - \frac{n(\vec{r})^2}{c^2} \frac{\partial^2 \vec{E}}{\partial t^2} + \nabla \left(\frac{1}{n(\vec{r})^2} \nabla n(\vec{r})^2 \cdot \vec{E} \right) = 0 \quad (5.1)$$

where c is the speed of light, $n(\vec{r})$ the refractive index in r and $\nabla^2 \vec{E}$ the Laplacian of the electric field. The equation in inhomogeneous media differs from that in the homogeneous case mainly by the third term. When the third term is absent, each Cartesian transverse component of the field obeys the scalar wave equation[176]. The third term, on the other hand, couples the components of the field and makes a vector treatment necessary.

In the case of an optical fiber with a core of index n_1 and a cladding of index n_2 , the first two terms have an amplitude of the order E_0/λ^2 and the third term has an amplitude of the order of $\frac{E_0}{\lambda^2} (n_1^2 - n_2^2)/n_2^2$ [177], where E_0 is the electric field's amplitude. There are two cases:

- $(n_1^2 - n_2^2)/n_2^2 \ll 1$: in this case the third term is negligible[178] and the guided modes are essentially the electric-magnetic transverse modes(TEM) [175];

¹A waveguide in which the index profile has abrupt changes between the core and the cladding is called a step-index waveguide.

²The medium is non-magnetic, linear, non-dispersive, isotropic and in the absence of charge and current.

- $(n_1^2 - n_2^2)/n_2^2 \simeq 1$: this is our case of a silica nanofiber $n_1 \simeq 1.46$ surrounded by air ($n_2 = 1$). In this case the third term plays an important role [176].

In this section I will follow the vector treatment proposed by *Snyder and Love*[176] looking for solutions of the equation 5.1 in the case of an optical nanofiber with the only constraint of $n_1 > n_2$, as described in [169] [177] [179] [180].

Let us consider a reference frame of cylindrical coordinates with the axis of the fiber parallel to the z -axis, as shown in figure 5.2.

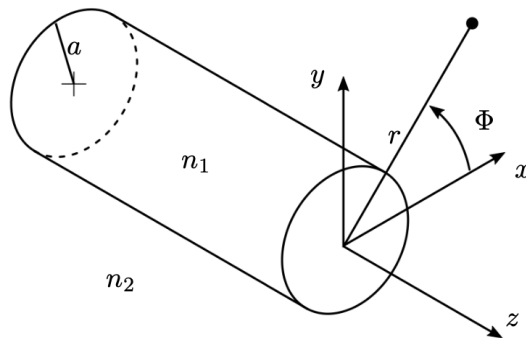


Figure 5.2. Reference frame used for the description of the electric field. The origin is fixed in the center of the fiber with the axis of the fiber coinciding with the z axis.

We first solve the equation 5.1 for the longitudinal components of the field E_z and H_z , separately in the core and in the cladding. The wave equation takes the form:

$$(\nabla^2 + n_{1,2}^2 k^2) \begin{bmatrix} E_z(r, \Phi, z) \\ H_z(r, \Phi, z) \end{bmatrix} = 0 \quad (5.2)$$

The solutions propagate in the z direction with a propagation constant $\beta = 2\pi n_{eff}/\lambda$, where n_{eff} is the effective refractive index, a key parameter in guided propagation. In the case of a optical fiber described by a core index n_1 and a cladding index n_2 , $n_2 \leq n_{eff} \leq n_1$. The wavelength of the guided light can thus be written as λ/n_{eff} , taking a value between λ/n_1 - that is, the wavelength for the light that propagates in the media of index n_1 - and the wavelength λ/n_2 , for light that propagates in the media of index n_2 . The solutions of eq. 5.2 can be written in the form:

$$\begin{bmatrix} E_z(r, \Phi, z) \\ H_z(r, \Phi, z) \end{bmatrix} \propto u(r) e^{\pm i l \Phi} e^{-i \beta z}, \quad l = 0, 1, 2, \dots \quad (5.3)$$

By introducing eq. 5.3 into eq.5.2, we obtain the differential Bessel equations for $u(r)$ in the core and in the cladding respectively:

$$\frac{\partial^2 u(r)}{\partial r^2} + \frac{1}{r} \frac{\partial u(r)}{\partial r} + (h^2 - \frac{l^2}{r^2}) u(r) = 0, \quad r \leq a \quad (\text{core}) \quad (5.4)$$

$$\frac{\partial^2 u(r)}{\partial r^2} + \frac{1}{r} \frac{\partial u(r)}{\partial r} + (q^2 + \frac{l^2}{r^2}) u(r) = 0, \quad r \geq a \quad (\text{cladding}) \quad (5.5)$$

where $h^2 = n_1^2 k^2 - \beta^2$ and $q^2 = \beta^2 - n_2^2 k^2$. By considering only the physically acceptable solutions, the following solutions are obtained:

$$\begin{bmatrix} E_z(r, \Phi, z) \\ H_z(r, \Phi, z) \end{bmatrix} = \begin{bmatrix} A \\ B \end{bmatrix} J_l(hr) e^{i(\pm l\Phi - \beta z)} \quad r \leq a \quad (5.6)$$

$$\begin{bmatrix} E_z(r, \Phi, z) \\ H_z(r, \Phi, z) \end{bmatrix} = \begin{bmatrix} C \\ D \end{bmatrix} K_l(qr) e^{i(\pm l\Phi - \beta z)} \quad r \geq a \quad (5.7)$$

where J_l is the l -order Bessel function of the first kind and K_l is the modified l -order Bessel function of the second kind (similar to an exponential decay).

Once the longitudinal field components, E_z and H_z , are known, all field components can be obtained. We can determine thus the remaining components of the field E_r , E_Φ , H_r and H_Φ starting from the components E_z and H_z and using Maxwell's equations $\nabla \times \vec{E} = -i\omega\mu_0\vec{H}$ and $\nabla \times \vec{H} = i\omega\epsilon_0 n^2 \vec{E}$. Boundary conditions at $r = a$ impose the following relations for the interior constants A and B , and for the exterior constants C and D :

$$\begin{aligned} \frac{B}{A} &= \pm \left[\left(\frac{1}{ha} \right)^2 + \left(\frac{1}{qa} \right)^2 \right] \left[\frac{J'_l(ha)}{haJ_l(ha)} + \frac{K'_l(qa)}{qaK_l(qa)} \right]^{-1} \\ \frac{C}{A} &= \frac{J_l(ha)}{K_l(qa)} \\ \frac{D}{A} &= \frac{B}{A} \frac{J_l(ha)}{K_l(qa)} - \frac{l^2 \beta^2}{K_0^2} \left[\left(\frac{1}{ha} \right)^2 + \left(\frac{1}{qa} \right)^2 \right]^2 \end{aligned} \quad (5.8)$$

The knowledge of the propagation constant β and the constant A completely define the system³. An eigenvalue equation determines the propagation constant:

$$\left[\frac{J'_l(ha)}{haJ_l(ha)} + \frac{K'_l(qa)}{qaK_l(qa)} \right] \left[n_1^2 \frac{J'_l(ha)}{haJ_l(ha)} + n_2^2 \frac{K'_l(qa)}{qaK_l(qa)} \right] = \beta^2 \frac{l^2}{k^2} \left(\frac{1}{(ha)^2} + \frac{1}{(qa)^2} \right)^2 \quad (5.9)$$

where, as seen, $h^2 = n_1^2 k^2 - \beta^2$ and $q^2 = \beta^2 - n_2^2 k^2$.

Before describing the solutions (modes) allowed by eq. 5.9, let's remember how the modes can be classified based on the characteristics of the longitudinal field components:

- A **transverse electric and magnetic mode**, or **TEM** mode, has $E_z = 0$ and $H_z = 0$. Thus dielectric waveguides do not support TEM modes.
- A **transverse electric mode**, or **TE** mode, has $E_z = 0$ and $H_z \neq 0$
- A **transverse magnetic mode**, or **TM** mode, has $E_z \neq 0$ and $H_z = 0$
- A **hybrid mode**, **HE** or **EH**, has both $E_z \neq 0$ and $H_z \neq 0$.

³A is usually determined using energy conservation by means of the Poynting vector

The eigenvalue equation 5.9 must be numerically solved and admits two families of solutions (modes): the hybrid modes HE_{lm} and EH_{lm} , where l and m respectively characterize the azimuthal and radial distributions. In particular, in the case $l = 0$, they are reduced to an electric transverse (TE_{0m}) or magnetic transverse (TM_{0m}) mode respectively. The mode properties of a waveguide are commonly characterized in terms of dimensionless waveguide parameters. One possible choice is to define a normalized frequency, also known as the *V number*:

$$V = \frac{2\pi}{\lambda} a \sqrt{n_1^2 - n_2^2} \quad (5.10)$$

where a is the radius of the fiber. In figure 5.3 are shown the solution of eq. 5.9 in terms of $n_{eff} = \beta/k$ as a function of V for various families of modes.

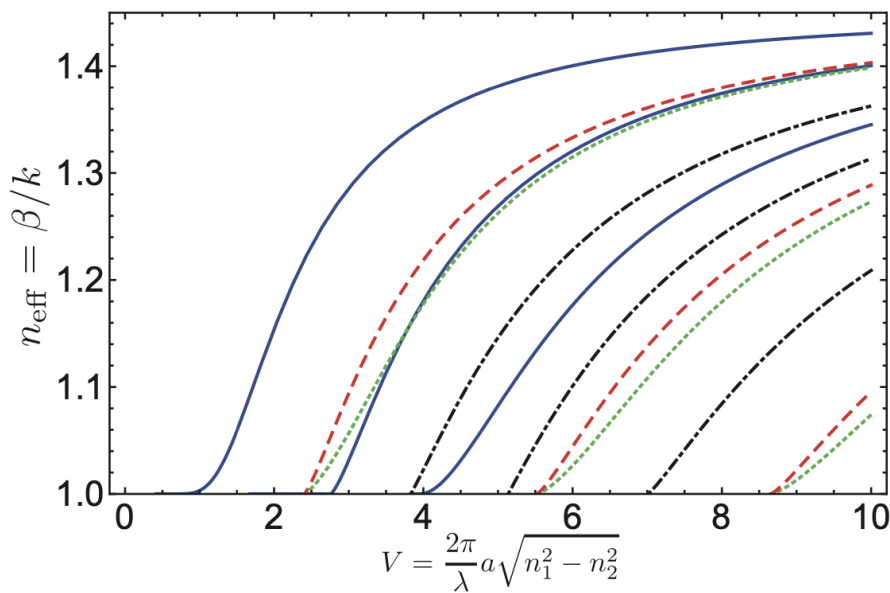


Figure 5.3. Effective index of refraction as a function of V-number. The families of modes and their colors are HE (solid blue), EH (dashed-dotted black), TE (dashed red), TM (dotted green). Figure taken from reference [169].

Only one solution remains when the diameter approaches zero: the fundamental mode HE_{11} . The waveguide is then single-mode under the condition:

$$0 < V < 2.405 \quad (5.11)$$

or, equivalently, $\rho/\lambda < 0.36$. The graph shows that, for an increasing fiber radius, the value of the effective index associated with the mode increases starting from the cladding value $n_2 = 1$ towards the core value $n_1 = 1.46$. When a mode is created, the light essentially *sees* the cladding index $n_2 = 1$, i.e. the fiber modes are outside the fiber. For a higher fiber radius the effective refractive index n_{eff} grows until, for a very large fiber, it approaches the core index n_1 , i.e. the modes propagate into the core .

5.2.2 Electric field of the HE_{11} mode

We are interested in the fundamental mode and, in particular, in the field outside the fiber since the emitters are positioned in this region. The cylindrical components of the fundamental mode field for $r > a$ can be written as:

$$\begin{aligned} E_r(r, \Phi, z, t) &= -iA \frac{\beta}{2q} \frac{J_1(ha)}{K_1(qa)} [(1-s)K_0(qr) + (1+s)K_2(qr)] e^{i(\omega t - \beta z)} \quad (5.12) \\ E_\Phi(r, \Phi, z, t) &= \pm A \frac{\beta}{2q} \frac{J_1(ha)}{K_1(qa)} [(1-s)K_0(qr) - (1+s)K_2(qr)] e^{i(\omega t - \beta z)} \\ E_z(r, \Phi, z, t) &= A \frac{J_1(ha)}{K_1(qa)} K_1(qr) e^{i(\omega t - \beta z)} \end{aligned}$$

where $h = \sqrt{n_1^2 k^2 - \beta^2}$, $q = \sqrt{\beta^2 - n_2^2 k^2}$, β is the propagation constant associated with the fundamental mode and

$$s = \frac{(qa)^{-2} + (ha)^{-2}}{J_1'(ha)/(haJ_1(ha)) + K_1'(qa)/(qaK_1(qa))}. \quad (5.13)$$

The \pm sign of the E_Φ component corresponds to two different polarizations of the HE_{11} mode. In fact, the two transverse components E_r and E_Φ oscillate in phase quadrature and the electric field describes an ellipse whose circulation, clockwise or anti-clockwise, is given by the sign of E_Φ . We denote these two modes with $HE_{11}^{circ, \pm}$. A superposition of this modes $\{HE_{11}^{circ, +} \pm HE_{11}^{circ, -}\}$ is still a solution of eq 5.1.

In the cylindrical coordinates the Cartesian components of the electric field in such a mode for $r > a$ can be written as:

$$\begin{aligned} E_x(r, \Phi, z, t) &= -iA \frac{\beta}{2q} \frac{J_1(ha)}{K_1(qa)} [(1-s)K_0(qr) \cos(\Phi_0) + (1+s)K_2(qr) \cos(2\Phi - \Phi_0)] e^{i(\omega t - \beta z)} \\ E_y(r, \Phi, z, t) &= -iA \frac{\beta}{2q} \frac{J_1(ha)}{K_1(qa)} [(1-s)K_0(qr) \sin(\Phi_0) + (1+s)K_2(qr) \sin(2\Phi - \Phi_0)] e^{i(\omega t - \beta z)} \\ E_z(r, \Phi, z, t) &= A \frac{J_1(ha)}{K_1(qa)} K_1(qr) \cos(\Phi - \Phi_0) e^{i(\omega t - \beta z)} \quad (5.14) \end{aligned}$$

The angle Φ_0 determines the orientation axis of the polarization of the field. The two sets of solutions corresponding to $\Phi_0 = 0, \pi/2$ express two different orthogonal and locally linear polarizations, aligned along the x and y axes, respectively. The two modes that correspond to these polarizations are denoted as HE_{11}^x and HE_{11}^y respectively.

The two representations presented, called *quasi-circular* and *quasi-linear* representations, constitute two equivalent bases for describing the electric field of a single-mode fiber.

5.2.3 Longitudinal component of the fundamental mode

The fundamental mode has a longitudinal component $E_z(r, \Phi) \neq 0$ which oscillates in phase quadrature with the transverse field. The presence of this component is a consequence of the Gauss law $\nabla \cdot \vec{E} = 0$. According to this equation a focused light beam of wavelength λ that propagates along $\pm z$ has a longitudinal component:

$$E_z = \pm ki \nabla \cdot \vec{E}_T \quad (5.15)$$

where the \pm corresponds to the two possible directions of propagation and \vec{E}_T is the transverse field. The presence of i in the expression for E_z means that E_z is phase quadrature with the transverse components, depending on the propagation direction.

From figure 5.4a we can observe that in the case of an HE_{11}^x mode, the transverse field goes from a maximum amplitude to an almost zero amplitude in a range of hundreds of nanometers. This rapid variation implies a significant longitudinal component according to eq 5.15. In fact in figure 5.4b it is possible to observe that the longitudinal component is about a third of the transverse component where the transverse field varies very rapidly. Instead, at the center of the fiber - where the transverse field is almost constant - the longitudinal component is zero. In general,

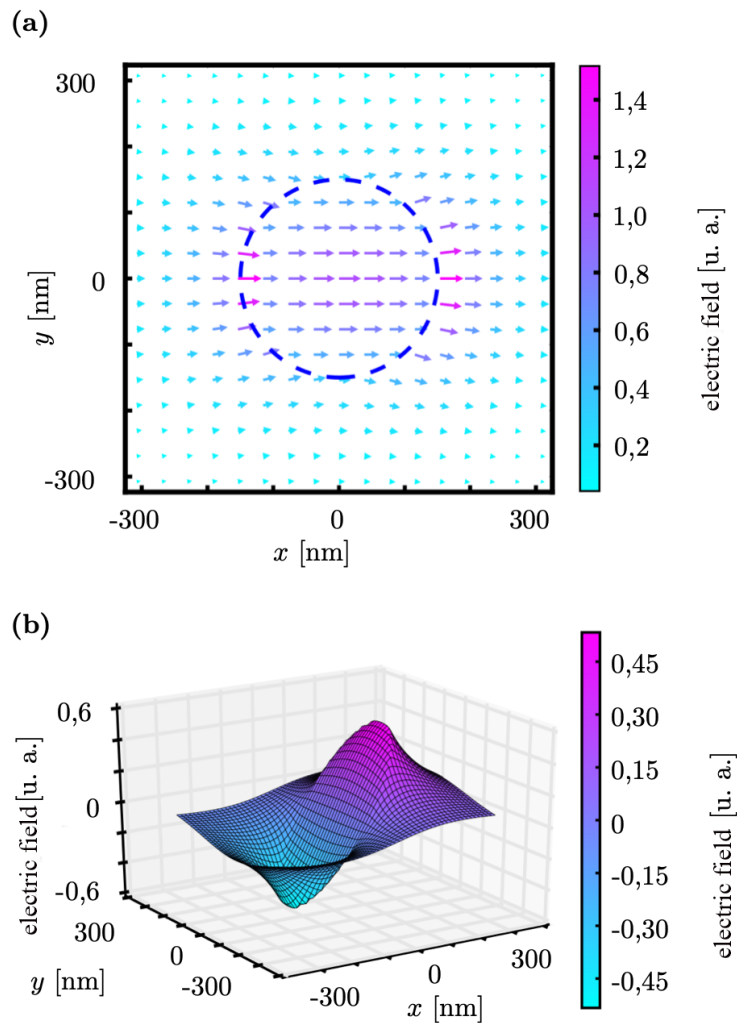


Figure 5.4. Electric field of the mode HE_{11}^x . Figure taken from reference [177].

the polarization of a quasi linear fundamental mode is elliptical in the plane in which the propagation axis and the main polarization axis lie. Moreover, polarization, direction of propagation and evanescent field follow the right hand rule, as illustrated

in figure 5.5. In our case the light propagates along the positive zeta axis; in the upper half-plane of the fiber the field circulates counterclockwise (i.e. it has spin along the y axis) and in the lower half-plane the circulation of the field is clockwise (i.e. the spin points in the opposite direction).

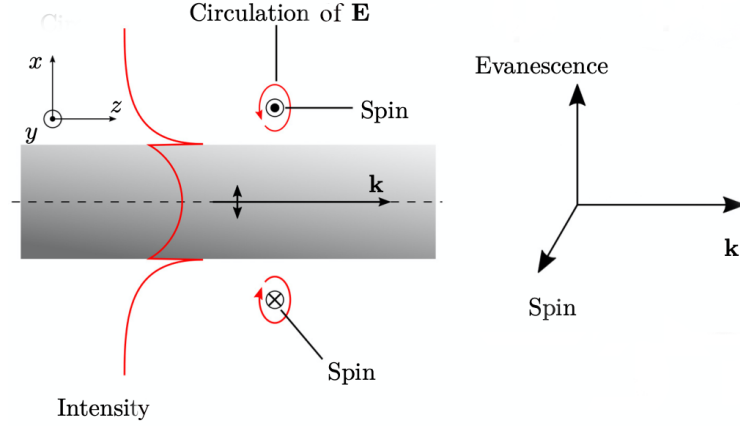


Figure 5.5. Interdependence between polarization, direction and evanescence. Figure taken from reference [177].

5.2.4 Choice of the nanofiber's diameter

We have seen that the effective refractive index β/k varies from a higher value $n_2 = 1.46$ for which the mode is mostly in the bulk silica to a lower value $n_1 = 1$ for which the mode is mostly in the evanescent field outside the fiber. We have also seen that the single-mode condition for vacuum-clad silica-core fibers requires that $a/\lambda < 0.36$ and this, as showed in figures 5.3 and 5.4, means that in this case the mode is mostly in the evanescent field outside the fiber and it is very intense near the nanofiber's surface. Figure 5.6 shows the different profiles inside and outside the nanofiber for the the total intensity of the electric field in a fundamental mode with quasi-linear polarization along x axis. In figure 5.7 the cross-section profiles of the intensities $|E_x|^2$, $|E_y|^2$ and $|E_z|^2$ of the Cartesian-coordinate components of the electric field are plotted⁴.

The strong evanescent field around the nanofibre is an efficiently tool for detecting nanoparticles in the vicinity of the fiber[182], allowing the light emitted by the nano-object to be coupled to the fiber. In fact it has been theoretically predicted that, due to the confinement of the field in the guided mode, an appreciable amount of fluorescence photons can be channeled into a single-guided mode of the nanofiber [31] and an efficient probing of few atom fluorescence through the guided mode of the nanofibre has been experimentally demonstrated[183].

The coupling between an emitter in the vicinity of the surface and the guided mode can be controlled and maximized by playing on the diameter of the nanofiber,

⁴We can see that $|E_z|^2$ is not negligible at all.

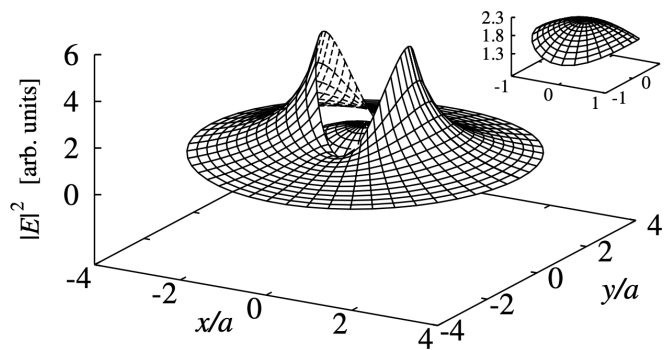


Figure 5.6. Cross-section profile of the total intensity $|E|^2$ of the electric field in a fundamental mode with quasi-linear polarization. The inset shows the inner part of the profile, which corresponds to the field inside the fiber. The parameters used: $a = 200nm$, $\lambda = 1.3\mu m$, $n_1 = 1.4469$, $n_2 = 1$, and $\Phi_0 = 0$. Figure taken from reference [181].

i.e. by looking for the diameter of the nanofiber for which the intensity is maximum at the surface. A maximum intensity is observed for a fiber diameter close to $\lambda/2$.

5.3 Producing optical nanofibers

The nanofiber is produced starting from a standard optical fiber and using taper fiber technology. The essence of this technology is to heat and pull a single-mode optical fiber to a very thin thickness maintaining the taper condition to keep adiabatically the single-mode condition. The apparatus used to produce the nanofibers is shown in figure 5.8.

The first step before pulling the fiber is to carefully clean it and remove the plastic buffer that covers the fiber. In fact, the pre-pull cleanliness of the fiber is essential to obtain high transmission through the optical nanofiber. If any particulate remains from the fiber buffer or if dust arrives on the fiber before being introduced to the flame, the particulate will burn and greatly diminish the final transmission. A three-step cleaning is performed: we use isopropyl alcohol on lens tissue to remove larger particulates, a few wipes of acetone are then applied in order to dissolve smaller remnants of the buffer and again a final cleaning with isopropyl alcohol removes residues left from the previous solvent, which can also decrease transmission.

The fiber is carefully placed into the grooves of the fiber clamps on the pulling apparatus. Here the fiber is suspended between two motorized translation stages that can move horizontally and are controlled by a computer. A Bunsen burner is positioned under the fiber and its vertical position is controlled by a motor, which provides also a controlled flame of H_2 and O_2 .

Once the fiber is ready, the tapering process is started from a computer-controlled interface. Once the characteristics of the nanofiber have been defined (desired diameter of the nanofiber, length of the nanofiber, profile of the transition zone),

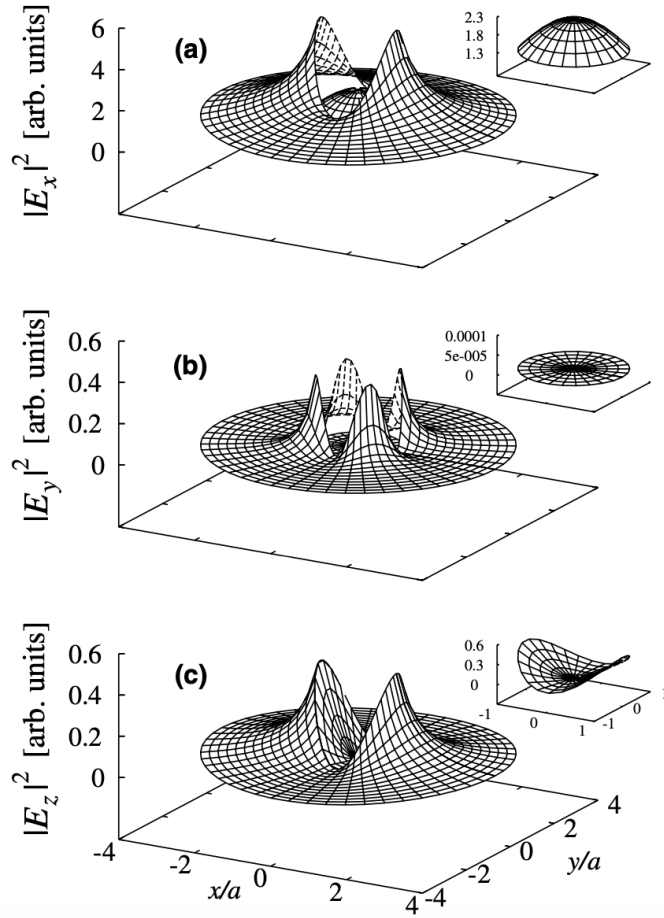


Figure 5.7. Cross-section profiles of the intensities $|E_x|^2$, $|E_y|^2$, and $|E_z|^2$ of the Cartesian-coordinate components of the electric field in a fundamental mode with quasi-linear polarization. The insets show the inner parts of the profiles, which correspond to the field inside the fiber. The parameters for this figure are the same as those for figure 5.6. Figure taken from reference [181].

the trajectories of the motorized translations are calculated using a Matlab routine [184]. When the pulling starts, the flame is placed at a given distance from the fiber and the motors start moving and pulling the fiber in order to obtain the desired shape. The movements needed to perform this operation depend not only on the chosen profile, but also on the physical characteristics of the flame, such as its size and temperature. The distance between the flame and the fiber, as well as the flux of hydrogen and oxygen need to be carefully chosen in order to obtain the effective flame diameter used to calculate the fiber profile. The tapering process lasts several minutes. A photodiode, placed at the output of the fiber allows to monitor the transmission during the whole pulling process. In addition, the image of the fiber is collected by a microscope objective and recorded by a camera behind it: this is useful for a correct positioning of the flame. With this method it is possible to reach fiber radii as small as 150 nm [185] and to observe transmissions over 95% [33].

In our case, we produced a nanofiber with a radius of 250 nm and we observed a transmission of 93%.

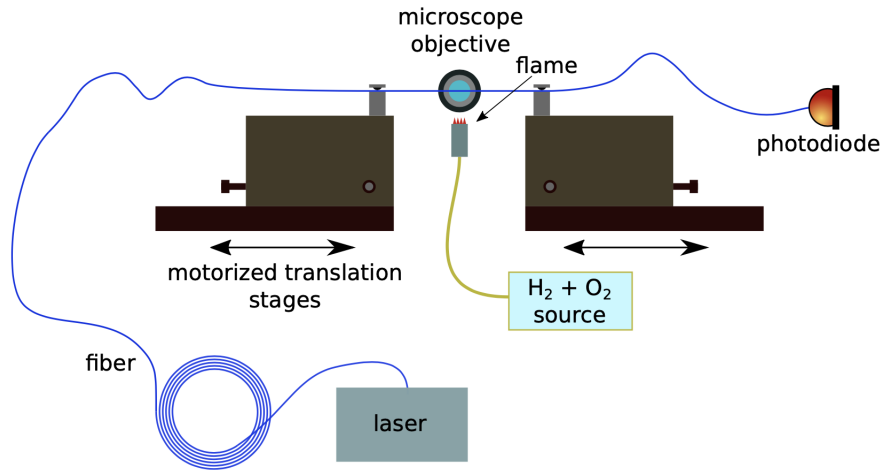


Figure 5.8. Scheme of the pulling setup. First the fiber is cleaned and clamped over the flame as shown, then the flame moves up and the two motorized platforms pull the fiber and move it over the flame, while the procedure is imaged using a microscope objective on top. The transmission is monitored over the whole procedure by a photodiode at the output of the fiber. All the protocol is controlled by a computer. Figure taken from reference [166].

5.4 Deposition technique

To place the nanoemitter on the nanofiber we touch the fiber with a drop of solution containing the nanoparticles, as shown in figure 5.9. It is important to have a solution diluted enough in order to be sure to deposit a very small number of nanoparticles on the nanofiber, ideally a single particle. Then we make a 1 : 100 dilution in toluene of the original solution and we take $20\mu\text{l}$ of this solution with a micro-pipette in order to obtain a drop at its end. The pipette is mounted on translation plates above the nanofiber, which allow the nanofiber to be gently touched with the drop, and then to take it off. This is a critical step, as the nanofiber can easily break and it is useful to monitor the movement with a microscope. When successful, this procedure results in several emitters deposited onto the nanofiber.

5.5 Antibunching measurement

Our goal is to detect single photon emission from a nanoemitter placed on the nanofiber, demonstrating that the single perovskite nanocrystal is coupled to the nanofiber and emits single photons directly inside it. The setup used for the antibunching measurement is shown in figure 5.10. First, we select the nanoemitter on which to perform the measurement. For this purpose the laser beam at 405

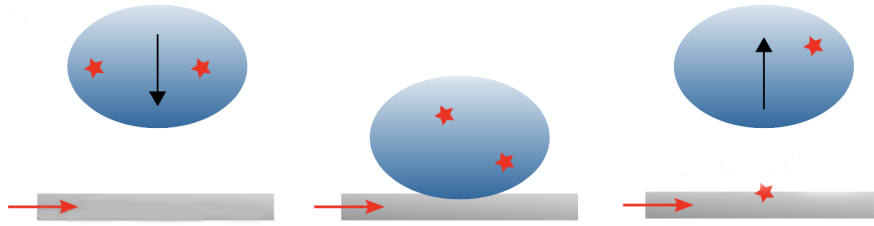


Figure 5.9. Illustration of the deposition technique. A drop of the colloidal solution is formed at the tip of a micro-pipette. We bring the drop closer to the nanofiber through which light propagates. After contact with the nanofiber, the drop is removed.

nm is sent into the fiber: in this way we can excite the emitters on the nanofiber and detect their photoluminescence through the microscope objective. We then excite the selected nanocrystal with the laser beam sent through that microscope objective and we collect the light from the fiber. The end of the fiber is plugged to an HBT setup for the g^2 measurement with the same protocol described in section 3.4⁵. With the dilution used, the nanocrystals can be used for some minutes once deposited.

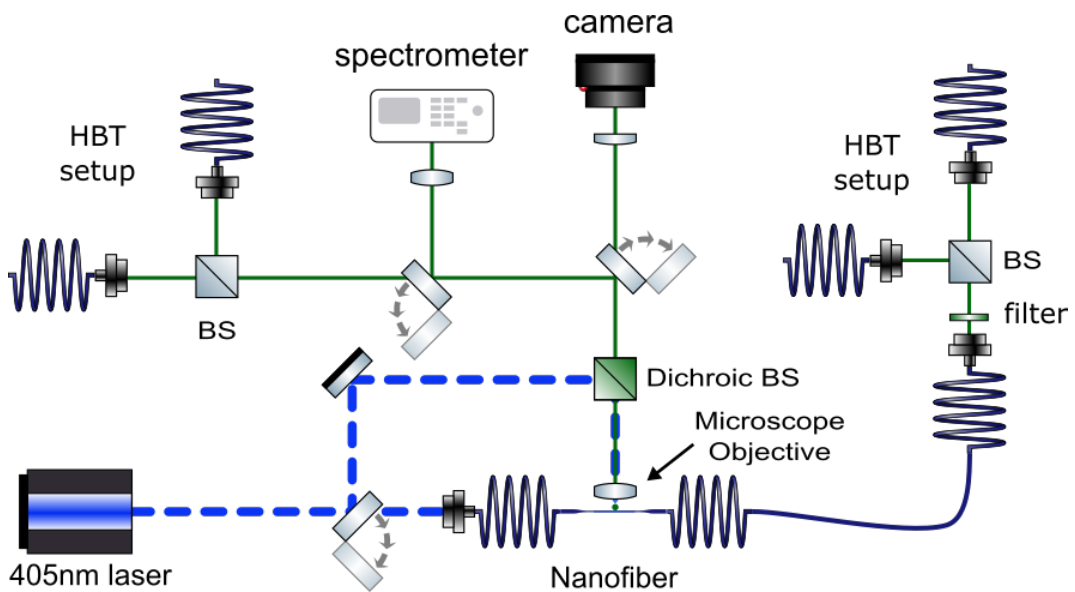


Figure 5.10. Setup used to measure single photons emission from a nanocrystal coupled to the nanofiber.

⁵Optionally, photon antibunching and spectral measurements can be performed also in free-space via the light collected with the microscope objective.

Figure 5.11 shows an antibunching measurement performed on the light collected via the nanofiber, corresponding to a $g^2(0) = 0.24$. This measurement, which has not yet been optimized, gives a result compatible with the $g^2(0)$ values obtained from the nanocrystals deposited on the glass microscope coverslip.

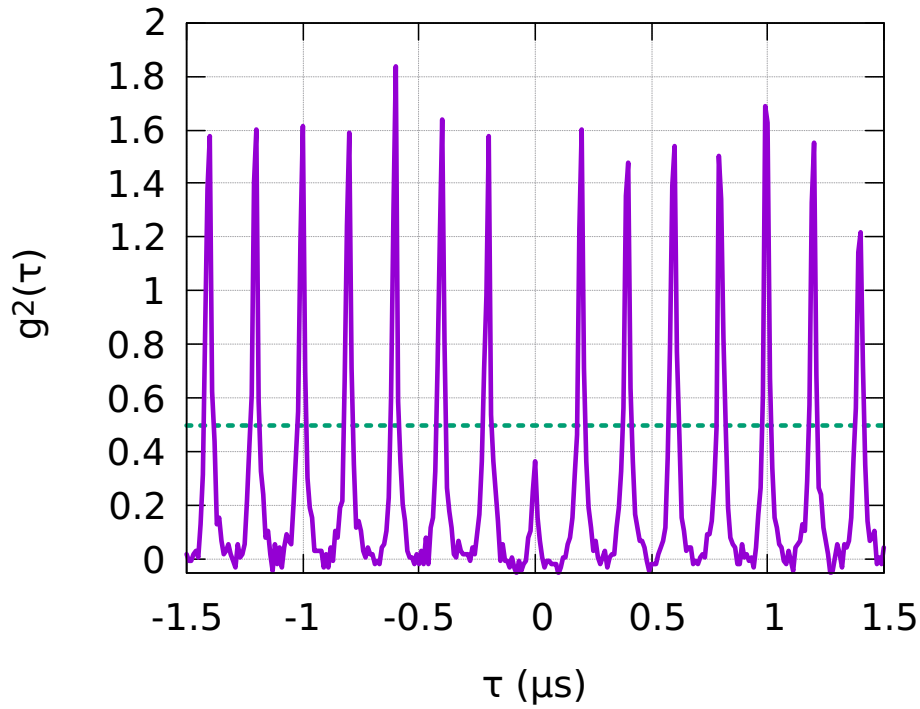


Figure 5.11. Autocorrelation function of a single nanocrystal emitting single photons into the nanofiber, measured with a repetition rate of 5 MHz.

We have then demonstrated that a significant fraction of the nanocrystal's emitted light is coupled into the nanofiber and propagates to its end and that our NCs are not damaged by the deposition process, validating this approach for this kind of sources.

Conclusion and outlook

In this thesis I presented a full analysis of the optical and quantum properties of highly photo-stable $CsPbBr_3$ perovskite nanocrystals.

Perovskite nanocrystals are versatile emitters and promising nano-objects for quantum applications: their emission's wavelength can be tuned playing on their size and composition and they show single photon emission at low and room temperatures. In recent years there has been a rapid development of the fabrication method of $CsPbBr_3$ perovskites in order to overcome the great instability due to moisture, oxygen and light, which characterize this kind of emitters.

In this work I characterized highly efficient $CsPbBr_3$ nanocubes synthesized with an established method used for the first time to produce quantum emitters. This method ensures an increased photostability and the possibility to excite the nanocrystals under optical excitation for more than one hour.

I prepared the samples for optical characterization measurements by spin-coating the colloidal solution containing $CsPbBr_3$ nanocubes. Firstly I showed the dependence of the photoluminescence on the excitation power, highlighting the importance of a saturation measurement to obtain a reference for the characterization of the different emitters. Wide-field and confocal microscopy techniques allowed me to have an overview of the sample and to select the single emitter to study, respectively. I measured the photoluminescence spectra, analyzing both the central wavelength and the FWHM distributions of the emission for a sample of 24 emitters. I studied the photostability under illumination, showing that our emitters exhibit a remarkable stability of about two orders of magnitude better than previous reported in literature. I also studied the role of the sample dilution on the stability, suggesting approaches to overcome the observed degradation. I then investigated the effect of the blinking on our nanocubes. After illustrating the different models proposed in the literature for the explanation of this phenomenon, I indicated the strong dependence of the spontaneous emission lifetime on the emission intensity as a tool for understanding the specific nature of blinking that characterizes our emitters. I also showed that the studied emitters are characterized by a reduced blinking with respect to the typical behavior of this kind of perovskites reported in literature. Using a polarization microscopy setup that takes into account the fluctuations of the emitted intensity due to the blinking, I showed that the nanocube's emission is slightly polarized. To verify the nanocrystals' nature as single photon emitters, I measured the second order auto-correlation function $g^2(0)$ using a Hanbury Brown and Twiss setup and I demonstrated that our nanocubes show strong photon antibunching of the emission and that the charge confinement has a crucial role on their quantum properties.

In the last part of this thesis I described the coupling of a single $CsPbBr_3$

nanocrystal with a tapered optical nanofiber, realized for the first time with such emitters. The nanofiber is produced starting from a standard optical fiber and using the tapered fiber technology: a single-mode optical fiber is heated and pulled - ensuring an adiabatic transition - until a sub-wavelength diameter is obtained. The choice of the diameter respects the single-mode condition for vacuum-clad silica-core fibers and it is such as to obtain a strong evanescent field around the nanofiber with a maximum intensity of the field near the nanofiber's surface. Such a nanofiber offers several advantages: the intense evanescent field allows the emitter's fluorescence photons to be channeled into the single-guided mode of the nanofiber and a high transmission is offered by the manufacturing technique in addition to a great versatility in terms of connectivity to others systems. After the deposition of the $CsPbBr_3$ nanocrystals onto the nanofiber, we performed antibunching measurements on the light collected via the nanofiber, obtaining a value of $g^2(0) = 0.24$. We then demonstrated that the single perovskite nanocrystal is coupled to the nanofiber and emits single photons directly inside it. Our result is a promising step towards the realization of compact, integrated, hybrid single photon devices at room temperature with perovskites nanoemitters [167, 186, 187, 188, 33, 189, 190, 191, 192, 193, 194, 195, 166, 196]. An important challenge to achieve this goal is to further improve the emitters' stability through an in-depth study of the role that ligands and dilution play on the nanocrystal's robustness.

Appendix A

Noise cleaning of the second order autocorrelation function

With the procedure illustrated below is possible to clean the g^2 histogram we get from TCSPC measurements from the background noise that characterizes the TCSPC technique.

Let's start by considering how the coincidences are counted. We call $M(\tau)$ the number of counts measured at a given delay τ . Each count can be generated either by a start from the signal or from the noise background and by a stop from the signal or from the noise background. Calling $s(\tau)$ the probability to have a start (or stop) generated by the signal and $b(\tau)$ the probability to have the start (or stop) generated by the background, we can write (when both $s(\tau)$ and $s(\tau) \ll 1$):

$$M(\tau) = C(b(\tau) + s(\tau))(b(\tau) + s(\tau)) \quad (\text{A.1})$$

where C is a constant of proportionality. We call $M' = \frac{M}{C}$. Considering τ_b between two consecutive peaks, we know that there is no signal there, $s(\tau_b) = 0$ and:

$$M'(\tau_b) = b^2(\tau_b) \quad (\text{A.2})$$

To find $M_c(\tau) = Cs^2(\tau)$ we solve the system of these two equations and we find that:

$$M_c(\tau) = M(\tau) + M(\tau_b) - 2\sqrt{M(\tau)}\sqrt{M(\tau_b)} \quad (\text{A.3})$$

With this formula we obtained the $g_2(\tau)$ histogram cleaned from the background counts.

Appendix B

Synthesis recipe

The recipe used to obtain the $CsPbBr_3$ perovskite nanocubes that have been studied in this thesis is described below.

Nanocrystals synthesis

The synthesis method requires that 174 mg of $PbBr_2$ are dissolved in 10 mL of octadecene in a three-neck flask. The flask is degased under vacuum at room temperatures for 15 minutes; then, the temperature is raised to 120°C. At 105°C the different ligands (in order 0.25 mL of oleylamine, 1.1 mL of oleic acid, 0.75 mL of octyl amine and 0.75 mL of octanoic acid) are injected making sure that vacuum has recovered after each injection. The solution is colorless at this stage and it is further degased at 120°C for 30 minutes. The atmosphere is switched to nitrogen and the temperature raised to 150°C. Around 0.1 mL of cesium oleate is injected in the flask and the solution turns turbid. After 35 minutes the solution is quickly cooled down using a ice-bath. The solution is transferred to plastic tube in order to be centrifuged and the supernatant is discarded. The pellet is dispersed in 5 mL of toluene and the solution is centrifuged again at low speed (2000 rpm for 1 min). Finally, the pellet is discarded and the colloiddally stable supernatant is stored.

Caesium oleate precursor

To obtain the Caesium oleate precursor 350 mg of Cs_2CO_3 of octadecene are mixed with 1.25 mL of oleic acid in a 50 mL three neck flask. The content of the flask is stirred and degased under vacuum at room temperature for 25 min. The flask is heated at 110°C for 15 min. The atmosphere is switched to nitrogen and the temperature raised to 150°C. The reaction is carried on for 15 min. At this stage the salt is fully dissolved. The temperature is cooled down below 100°C and the flask degased under vacuum.

Chemicals

$PbBr_2$ (Alfa Aesar, 98.5%), Cs_2CO_3 (Alfa aesar, 99,99%), oleylamine (OLA, Acros, 80 – 90%), oleic acid (OA, Sigma-Aldrich), octylamine (Oct.Am, Alfa aesar, 99%), Octanoic acid (Oct.Acid, Acros, 99%), octadecene (ODE, Acros Organics, 90%), toluene (VWR, rectapur).

Bibliography

- [1] Antonio Acín, Immanuel Bloch, Harry Buhrman, Tommaso Calarco, Christopher Eichler, Jens Eisert, Daniel Esteve, Nicolas Gisin, Steffen J Glaser, Fedor Jelezko, et al. The quantum technologies roadmap: a european community view. *New Journal of Physics*, 20(8):080201, 2018.
- [2] H Jeff Kimble. The quantum internet. *Nature*, 453(7198):1023–1030, 2008.
- [3] Stefano Pirandola, Jens Eisert, Christian Weedbrook, Akira Furusawa, and Samuel L Braunstein. Advances in quantum teleportation. *Nature photonics*, 9(10):641–652, 2015.
- [4] Ryszard Horodecki, Paweł Horodecki, Michał Horodecki, and Karol Horodecki. Quantum entanglement. *Reviews of modern physics*, 81(2):865, 2009.
- [5] Nicolas Gisin, Grégoire Ribordy, Wolfgang Tittel, and Hugo Zbinden. Quantum cryptography. *Reviews of modern physics*, 74(1):145, 2002.
- [6] Artur K Ekert. Quantum cryptography based on bell’s theorem. *Physical review letters*, 67(6):661, 1991.
- [7] Hoi-Kwong Lo and Hoi Fung Chau. Unconditional security of quantum key distribution over arbitrarily long distances. *science*, 283(5410):2050–2056, 1999.
- [8] Emanuel Knill, Raymond Laflamme, and Gerald J Milburn. A scheme for efficient quantum computation with linear optics. *nature*, 409(6816):46–52, 2001.
- [9] Pieter Kok, William J Munro, Kae Nemoto, Timothy C Ralph, Jonathan P Dowling, and Gerard J Milburn. Linear optical quantum computing with photonic qubits. *Reviews of Modern Physics*, 79(1):135, 2007.
- [10] Vittorio Giovannetti, Seth Lloyd, and Lorenzo Maccone. Quantum-enhanced measurements: beating the standard quantum limit. *Science*, 306(5700):1330–1336, 2004.
- [11] Vittorio Giovannetti, Seth Lloyd, and Lorenzo Maccone. Advances in quantum metrology. *Nature photonics*, 5(4):222, 2011.
- [12] Matthew D Eisaman, Jingyun Fan, Alan Migdall, and Sergey V Polyakov. Invited review article: Single-photon sources and detectors. *Review of scientific instruments*, 82(7):071101, 2011.

- [13] Markus Hennrich, Thomas Legero, Axel Kuhn, and Gerhard Rempe. Photon statistics of a non-stationary periodically driven single-photon source. *New Journal of Physics*, 6(1):86, 2004.
- [14] J McKeever, A Boca, AD Boozer, R Miller, JR Buck, A Kuzmich, and HJ Kimble. Deterministic generation of single photons from one atom trapped in a cavity. *Science*, 303(5666):1992–1994, 2004.
- [15] Axel Kuhn, Markus Hennrich, and Gerhard Rempe. Deterministic single-photon source for distributed quantum networking. *Physical review letters*, 89(6):067901, 2002.
- [16] Christian Maurer, Christoph Becher, Carlos Russo, Jürgen Eschner, and Rainer Blatt. A single-photon source based on a single Ca^{+} ion. *New journal of physics*, 6(1):94, 2004.
- [17] Matthias Keller, Birgit Lange, Kazuhiro Hayasaka, Wolfgang Lange, and Herbert Walther. Continuous generation of single photons with controlled waveform in an ion-trap cavity system. *Nature*, 431(7012):1075–1078, 2004.
- [18] Boris B Blinov, David L Moehring, L-M Duan, and Chris Monroe. Observation of entanglement between a single trapped atom and a single photon. *Nature*, 428(6979):153–157, 2004.
- [19] Brahim Lounis and William E Moerner. Single photons on demand from a single molecule at room temperature. *Nature*, 407(6803):491–493, 2000.
- [20] F De Martini, G Di Giuseppe, and M Marrocco. Single-mode generation of quantum photon states by excited single molecules in a microcavity trap. *Physical review letters*, 76(6):900, 1996.
- [21] Christian Brunel, Brahim Lounis, Philippe Tamarat, and Michel Orrit. Triggered source of single photons based on controlled single molecule fluorescence. *Physical Review Letters*, 83(14):2722, 1999.
- [22] Christian Kurtsiefer, Sonja Mayer, Patrick Zarda, and Harald Weinfurter. Stable solid-state source of single photons. *Physical review letters*, 85(2):290, 2000.
- [23] Alexios Beveratos, Rosa Brouri, Thierry Gacoin, Jean-Philippe Poizat, and Philippe Grangier. Nonclassical radiation from diamond nanocrystals. *Physical Review A*, 64(6):061802, 2001.
- [24] Romain Alléaume, François Treussart, Gaëtan Messin, Yannick Dumeige, Jean-François Roch, Alexios Beveratos, Rosa Brouri-Tualle, Jean-Philippe Poizat, and Philippe Grangier. Experimental open-air quantum key distribution with a single-photon source. *New Journal of physics*, 6(1):92, 2004.
- [25] Andrew J Shields. Semiconductor quantum light sources. In *Nanoscience And Technology: A Collection of Reviews from Nature Journals*, pages 221–229. World Scientific, 2010.

- [26] Charles Santori, David Fattal, Jelena Vučković, Glenn S Solomon, and Yoshihisa Yamamoto. Indistinguishable photons from a single-photon device. *nature*, 419(6907):594–597, 2002.
- [27] Zhiliang Yuan, Beata E Kardynal, R Mark Stevenson, Andrew J Shields, Charlene J Lobo, Ken Cooper, Neil S Beattie, David A Ritchie, and Michael Pepper. Electrically driven single-photon source. *science*, 295(5552):102–105, 2002.
- [28] Stefan Strauf, Nick G Stoltz, Matthew T Rakher, Larry A Coldren, Pierre M Petroff, and Dirk Bouwmeester. High-frequency single-photon source with polarization control. *Nature photonics*, 1(12):704, 2007.
- [29] Young-Shin Park, Shaojun Guo, Nikolay S Makarov, and Victor I Klimov. Room temperature single-photon emission from individual perovskite quantum dots. *Acs Nano*, 9(10):10386–10393, 2015.
- [30] Maksym V Kovalenko, Loredana Protesescu, and Maryna I Bodnarchuk. Properties and potential optoelectronic applications of lead halide perovskite nanocrystals. *Science*, 358(6364):745–750, 2017.
- [31] Fam Le Kien, S Dutta Gupta, VI Balykin, and K Hakuta. Spontaneous emission of a cesium atom near a nanofiber: Efficient coupling of light to guided modes. *Physical Review A*, 72(3):032509, 2005.
- [32] VV Klimov and Martial Ducloy. Spontaneous emission rate of an excited atom placed near a nanofiber. *Physical Review A*, 69(1):013812, 2004.
- [33] Maxime Joos, Chengjie Ding, Vivien Loo, Guillaume Blanquer, Elisabeth Giacobino, Alberto Bramati, Valentina Krachmalnicoff, and Quentin Glorieux. Polarization control of linear dipole radiation using an optical nanofiber. *Physical Review Applied*, 9(6):064035, 2018.
- [34] Ramachandrarao Yalla, KP Nayak, and K Hakuta. Fluorescence photon measurements from single quantum dots on an optical nanofiber. *Optics express*, 20(3):2932–2941, 2012.
- [35] Vadim V Vorobyov, Vladimir V Soshenko, Stepan V Bolshedvorskii, Javid Javadzade, Nikolay Lebedev, Andrey N Smolyaninov, Vadim N Sorokin, and Alexey V Akimov. Coupling of single nv center to adiabatically tapered optical single mode fiber. *The European Physical Journal D*, 70(12):269, 2016.
- [36] Rodney Loudon. *The quantum theory of light*. OUP Oxford, 2000.
- [37] Christopher Gerry, Peter Knight, and Peter L Knight. *Introductory quantum optics*. Cambridge university press, 2005.
- [38] Roy J Glauber. Coherent and incoherent states of the radiation field. *Physical Review*, 131(6):2766, 1963.
- [39] Roy J Glauber. The quantum theory of optical coherence. *Physical Review*, 130(6):2529, 1963.

- [40] Marlan O Scully and M Suhail Zubairy. Quantum optics, 1999.
- [41] Fu-Guo Deng and Gui Lu Long. Bidirectional quantum key distribution protocol with practical faint laser pulses. *Physical Review A*, 70(1):012311, 2004.
- [42] Brahim Lounis and Michel Orrit. Single-photon sources. *Reports on Progress in Physics*, 68(5):1129, 2005.
- [43] Rosa Brouri, Alexios Beveratos, Jean-Philippe Poizat, and Philippe Grangier. Single-photon generation by pulsed excitation of a single dipole. *Physical Review A*, 62(6):063817, 2000.
- [44] Mark Fox. *Quantum optics: an introduction*, volume 15. OUP Oxford, 2006.
- [45] R Hanbury Brown and Richard Q Twiss. Lxxiv. a new type of interferometer for use in radio astronomy. *The London, Edinburgh, and Dublin Philosophical Magazine and Journal of Science*, 45(366):663–682, 1954.
- [46] R Hanbury Brown and Richard Q Twiss. A test of a new type of stellar interferometer on sirius. *Nature*, 178(4541):1046–1048, 1956.
- [47] Pascale Senellart, Glenn Solomon, and Andrew White. High-performance semiconductor quantum-dot single-photon sources. *Nature nanotechnology*, 12(11):1026, 2017.
- [48] Chong-Ki Hong, Zhe-Yu Ou, and Leonard Mandel. Measurement of subpicosecond time intervals between two photons by interference. *Physical review letters*, 59(18):2044, 1987.
- [49] Benjamin Kambs and Christoph Becher. Limitations on the indistinguishability of photons from remote solid state sources. *New Journal of Physics*, 20(11):115003, 2018.
- [50] Mark Oxborrow and Alastair G Sinclair. Single-photon sources. *Contemporary Physics*, 46(3):173–206, 2005.
- [51] Alexander L Efros and David J Nesbitt. Origin and control of blinking in quantum dots. *Nature Nanotechnology*, 11(8):661, 2016.
- [52] Pavel Frantsuzov, Masaru Kuno, Boldizsar Janko, and Rudolph A Marcus. Universal emission intermittency in quantum dots, nanorods and nanowires. *Nature Physics*, 4(7):519–522, 2008.
- [53] C Bradac, T Gaebel, N Naidoo, MJ Sellars, J Twamley, LJ Brown, AS Barnard, T Plakhotnik, AV Zvyagin, and JR Rabeau. Observation and control of blinking nitrogen-vacancy centres in discrete nanodiamonds. *Nature nanotechnology*, 5(5):345–349, 2010.
- [54] Elke Neu, Mario Agio, and Christoph Becher. Photophysics of single silicon vacancy centers in diamond: implications for single photon emission. *Optics express*, 20(18):19956–19971, 2012.

- [55] Eli Barkai, YounJoon Jung, and Robert Silbey. Theory of single-molecule spectroscopy: beyond the ensemble average. *Annu. Rev. Phys. Chem.*, 55:457–507, 2004.
- [56] Thomas Gensch, Martin Böhmer, and Pedro F Aramendía. Single molecule blinking and photobleaching separated by wide-field fluorescence microscopy. *The Journal of Physical Chemistry A*, 109(30):6652–6658, 2005.
- [57] Xavier Brokmann. *Propriétés de fluorescence de nanocristaux de CdSe individuels*. PhD thesis, Université Pierre et Marie Curie-Paris VI, 2004.
- [58] G Margolin, V Protasenko, M Kuno, and E Barkai. Photon counting statistics for blinking cdse- zns quantum dots: A lévy walk process. *The Journal of Physical Chemistry B*, 110(38):19053–19060, 2006.
- [59] Xavier Brokmann, J-P Hermier, Gaëtan Messin, Pierre Desbiolles, J-P Bouchaud, and Maxime Dahan. Statistical aging and nonergodicity in the fluorescence of single nanocrystals. *Physical review letters*, 90(12):120601, 2003.
- [60] G Margolin and E Barkai. Nonergodicity of blinking nanocrystals and other lévy-walk processes. *Physical review letters*, 94(8):080601, 2005.
- [61] Manoj Nirmal, Bashir O Dabbousi, Mounqi G Bawendi, JJ Macklin, JK Trautman, TD Harris, and Louis E Brus. Fluorescence intermittency in single cadmium selenide nanocrystals. *Nature*, 383(6603):802–804, 1996.
- [62] Al L Efros and M Rosen. Random telegraph signal in the photoluminescence intensity of a single quantum dot. *Physical Review Letters*, 78(6):1110, 1997.
- [63] Rogier Verberk, Antoine M van Oijen, and Michel Orrit. Simple model for the power-law blinking of single semiconductor nanocrystals. *Physical Review B*, 66(23):233202, 2002.
- [64] M Kuno, DP Fromm, ST Johnson, Alan Gallagher, and David J Nesbitt. Modeling distributed kinetics in isolated semiconductor quantum dots. *Physical Review B*, 67(12):125304, 2003.
- [65] Edo Waks, Eleni Diamanti, and Yoshihisa Yamamoto. Generation of photon number states. *New Journal of Physics*, 8(1):4, 2006.
- [66] Alfred B U'Ren, Christine Silberhorn, Konrad Banaszek, and Ian A Walmsley. Efficient conditional preparation of high-fidelity single photon states for fiber-optic quantum networks. *Physical review letters*, 93(9):093601, 2004.
- [67] Elizabeth A Goldschmidt, Matthew D Eisaman, Jingyun Fan, Sergey V Polyakov, and Alan Migdall. Spectrally bright and broad fiber-based heralded single-photon source. *Physical Review A*, 78(1):013844, 2008.
- [68] Alan L Migdall, D Branning, and Stefania Castelletto. Tailoring single-photon and multiphoton probabilities of a single-photon on-demand source. *Physical Review A*, 66(5):053805, 2002.

- [69] Jeffrey H Shapiro and Franco N Wong. On-demand single-photon generation using a modular array of parametric downconverters with electro-optic polarization controls. *Optics letters*, 32(18):2698–2700, 2007.
- [70] William E Moerner and Michel Orrit. Illuminating single molecules in condensed matter. *Science*, 283(5408):1670–1676, 1999.
- [71] X Sunney Xie and Jay K Trautman. Optical studies of single molecules at room temperature. *Annual review of physical chemistry*, 49(1):441–480, 1998.
- [72] Sophia E Economou and Pratibha Dev. Spin-photon entanglement interfaces in silicon carbide defect centers. *Nanotechnology*, 27(50):504001, 2016.
- [73] Philip Moriarty. Nanostructured materials. *Reports on Progress in Physics*, 64(3):297, 2001.
- [74] Xavier Brokmann, E Giacobino, Maxime Dahan, and Jean-Pierre Hermier. Highly efficient triggered emission of single photons by colloidal cdse/ zns nanocrystals. *Applied Physics Letters*, 85(5):712–714, 2004.
- [75] Nam-Gyu Park. Perovskite solar cells: an emerging photovoltaic technology. *Materials today*, 18(2):65–72, 2015.
- [76] Gabriele Rainò, Michael A Becker, Maryna I Bodnarchuk, Rainer F Mahrt, Maksym V Kovalenko, and Thilo Stöferle. Superfluorescence from lead halide perovskite quantum dot superlattices. *Nature*, 563(7733):671–675, 2018.
- [77] Lung-Chien Chen, Ching-Ho Tien, Zong-Liang Tseng, Yu-Shen Dong, and Shengyi Yang. Influence of pmma on all-inorganic halide perovskite cspbbr3 quantum dots combined with polymer matrix. *Materials*, 12(6):985, 2019.
- [78] Gabriele Rainò, Annelies Landuyt, Franziska Krieg, Caterina Bernasconi, Stefan T Ochsenbein, Dmitry N Dirin, Maryna I Bodnarchuk, and Maksym V Kovalenko. Underestimated effect of a polymer matrix on the light emission of single cspbbr3 nanocrystals. *Nano letters*, 19(6):3648–3653, 2019.
- [79] Seryio Saris, Sanduni T Dona, Valerie Niemann, Anna Loiudice, and Raffaella Buonsanti. Optimizing the atomic layer deposition of alumina on perovskite nanocrystal films by using o2 as a molecular probe. *Helvetica Chimica Acta*, 2019.
- [80] Qinyong Xiang, Binze Zhou, Kun Cao, Yanwei Wen, Yun Li, Zhaojie Wang, Chenchen Jiang, Bin Shan, and Rong Chen. Bottom up stabilization of cspbbr3 quantum dots-silica sphere with selective surface passivation via atomic layer deposition. *Chemistry of Materials*, 30(23):8486–8494, 2018.
- [81] Jun Pan, Smritakshi P Sarmah, Banavoth Murali, Ibrahim Dursun, Wei Peng, Manas R Parida, Jiakai Liu, Lutfan Sinatra, Noktan Alyami, Chao Zhao, et al. Air-stable surface-passivated perovskite quantum dots for ultra-robust, single-and two-photon-induced amplified spontaneous emission. *The journal of physical chemistry letters*, 6(24):5027–5033, 2015.

- [82] Horace Lemuel Wells. Über die cäsium-und kalium-bleihalogenide. *Zeitschrift für anorganische Chemie*, 3(1):195–210, 1893.
- [83] CHR KN MØLLER. Crystal structure and photoconductivity of caesium plumbahalides. *Nature*, 182(4647):1436–1436, 1958.
- [84] Dieter Weber. $\text{Ch}_3\text{nh}_3\text{pbx}_3$, ein pb (ii)-system mit kubischer perowskitstruktur/ $\text{ch}_3\text{nh}_3\text{pbx}_3$, a pb (ii)-system with cubic perovskite structure. *Zeitschrift für Naturforschung B*, 33(12):1443–1445, 1978.
- [85] Guangru Li, Zhi-Kuang Tan, Dawei Di, May Ling Lai, Lang Jiang, Jonathan Hua-Wei Lim, Richard H Friend, and Neil C Greenham. Efficient light-emitting diodes based on nanocrystalline perovskite in a dielectric polymer matrix. *Nano letters*, 15(4):2640–2644, 2015.
- [86] Young-Hoon Kim, Himchan Cho, Jin Hyuck Heo, Tae-Sik Kim, NoSung Myoung, Chang-Lyoul Lee, Sang Hyuk Im, and Tae-Woo Lee. Multicolored organic/inorganic hybrid perovskite light-emitting diodes. *Advanced materials*, 27(7):1248–1254, 2015.
- [87] Haiming Zhu, Yongping Fu, Fei Meng, Xiaoxi Wu, Zizhou Gong, Qi Ding, Martin V Gustafsson, M Tuan Trinh, Song Jin, and XY Zhu. Lead halide perovskite nanowire lasers with low lasing thresholds and high quality factors. *Nature materials*, 14(6):636–642, 2015.
- [88] Guichuan Xing, Nripan Mathews, Swee Sien Lim, Natalia Yantara, Xinfeng Liu, Dharani Sabba, Michael Grätzel, Subodh Mhaisalkar, and Tze Chien Sum. Low-temperature solution-processed wavelength-tunable perovskites for lasing. *Nature materials*, 13(5):476, 2014.
- [89] Yongping Fu, Haiming Zhu, Jie Chen, Matthew P Hautzinger, X-Y Zhu, and Song Jin. Metal halide perovskite nanostructures for optoelectronic applications and the study of physical properties. *Nature Reviews Materials*, 4(3):169–188, 2019.
- [90] Federico Brivio, Jarvist M Frost, Jonathan M Skelton, Adam J Jackson, Oliver J Weber, Mark T Weller, Alejandro R Goni, Aurélien MA Leguy, Piers RF Barnes, and Aron Walsh. Lattice dynamics and vibrational spectra of the orthorhombic, tetragonal, and cubic phases of methylammonium lead iodide. *Physical Review B*, 92(14):144308, 2015.
- [91] Constantinos C Stoumpos and Mercouri G Kanatzidis. The renaissance of halide perovskites and their evolution as emerging semiconductors. *Accounts of chemical research*, 48(10):2791–2802, 2015.
- [92] Joshua Young and James M Rondinelli. Octahedral rotation preferences in perovskite iodides and bromides. *The journal of physical chemistry letters*, 7(5):918–922, 2016.
- [93] Qi Chen, Nicholas De Marco, Yang Michael Yang, Tze-Bin Song, Chun-Chao Chen, Hongxiang Zhao, Ziruo Hong, Huanping Zhou, and Yang Yang. Under

- the spotlight: The organic–inorganic hybrid halide perovskite for optoelectronic applications. *Nano Today*, 10(3):355–396, 2015.
- [94] Shunsuke Hirotsu, Jimpei Harada, Masashi Iizumi, and Kazuo Gesi. Structural phase transitions in CsPbBr_3 . *Journal of the Physical Society of Japan*, 37(5):1393–1398, 1974.
- [95] Tomas Leijtens, Kevin Bush, Rongrong Cheacharoen, Rachel Beal, Andrea Bowring, and Michael D McGehee. Towards enabling stable lead halide perovskite solar cells; interplay between structural, environmental, and thermal stability. *Journal of Materials Chemistry A*, 5(23):11483–11500, 2017.
- [96] Gregor Kieslich, Shijing Sun, and Anthony K Cheetham. Solid-state principles applied to organic–inorganic perovskites: new tricks for an old dog. *Chemical Science*, 5(12):4712–4715, 2014.
- [97] Chonghea Li, Xionggang Lu, Weizhong Ding, Liming Feng, Yonghui Gao, and Ziming Guo. Formability of ABX_3 ($x = \text{f, cl, br, i}$) halide perovskites. *Acta Crystallographica Section B: Structural Science*, 64(6):702–707, 2008.
- [98] Guoqing Tong, Luis K Ono, and Yabing Qi. Recent progress of all-bromide inorganic perovskite solar cells. *Energy Technology*, 8(4):1900961, 2020.
- [99] Alex Aziz, Nicholas Aristidou, Xiangnan Bu, Robert JE Westbrook, Saif A Haque, and M Saiful Islam. Understanding the enhanced stability of bromide substitution in lead iodide perovskites. *Chemistry of Materials*, 32(1):400–409, 2019.
- [100] G Murtaza and Iftikhar Ahmad. First principle study of the structural and optoelectronic properties of cubic perovskites CsPbM_3 ($m = \text{cl, br, i}$). *Physica B: Condensed Matter*, 406(17):3222–3229, 2011.
- [101] Yuan Ye, Xu Run, Xu Hai-Tao, Hong Feng, Xu Fei, and Wang Lin-Jun. Nature of the band gap of halide perovskites ABX_3 ($a = \text{CH}_3\text{NH}_3$, Cs ; $b = \text{Sn, Pb}$; $x = \text{cl, br, i}$): First-principles calculations. *Chinese Physics B*, 24(11):116302, 2015.
- [102] Li Lang, Ji-Hui Yang, Heng-Rui Liu, HJ Xiang, and XG Gong. First-principles study on the electronic and optical properties of cubic ABX_3 halide perovskites. *Physics Letters A*, 378(3):290–293, 2014.
- [103] Michael A Becker, Roman Vaxenburg, Georgian Nedelcu, Peter C Sercel, Andrew Shabaev, Michael J Mehl, John G Michopoulos, Samuel G Lambrakos, Noam Bernstein, John L Lyons, et al. Bright triplet excitons in caesium lead halide perovskites. *Nature*, 553(7687):189–193, 2018.
- [104] Xiaoming Li, Ye Wu, Shengli Zhang, Bo Cai, Yu Gu, Jizhong Song, and Haibo Zeng. CsPbX_3 quantum dots for lighting and displays: room-temperature synthesis, photoluminescence superiorities, underlying origins and white light-emitting diodes. *Advanced Functional Materials*, 26(15):2435–2445, 2016.

- [105] M Sebastian, JA Peters, CC Stoumpos, J Im, SS Kostina, Zhifu Liu, Mercuri G Kanatzidis, Arthur J Freeman, and Bruce W Wessels. Excitonic emissions and above-band-gap luminescence in the single-crystal perovskite semiconductors CsPbBr_3 and CsPbI_3 . *Physical Review B*, 92(23):235210, 2015.
- [106] Subham Dastidar, Christopher J Hawley, Andrew D Dillon, Alejandro D Gutierrez-Perez, Jonathan E Spanier, and Aaron T Fafarman. Quantitative phase-change thermodynamics and metastability of perovskite-phase cesium lead iodide. *The journal of physical chemistry letters*, 8(6):1278–1282, 2017.
- [107] Loredana Protesescu, Sergii Yakunin, Maryna I Bodnarchuk, Franziska Krieg, Riccarda Caputo, Christopher H Hendon, Ruo Xi Yang, Aron Walsh, and Maksym V Kovalenko. Nanocrystals of cesium lead halide perovskites (CsPbX_3 , $x = \text{Cl, Br, and I}$): novel optoelectronic materials showing bright emission with wide color gamut. *Nano letters*, 15(6):3692–3696, 2015.
- [108] Dawei Di, Kevin P Musselman, Guangru Li, Aditya Sadhanala, Yulia Ievskaya, Qilei Song, Zhi-Kuang Tan, May Ling Lai, Judith L MacManus-Driscoll, Neil C Greenham, et al. Size-dependent photon emission from organometal halide perovskite nanocrystals embedded in an organic matrix. *The journal of physical chemistry letters*, 6(3):446–450, 2015.
- [109] Pooja Tyagi, Sarah M Arveson, and William A Tisdale. Colloidal organohalide perovskite nanoplatelets exhibiting quantum confinement. *The journal of physical chemistry letters*, 6(10):1911–1916, 2015.
- [110] Fengrui Hu, Huichao Zhang, Chun Sun, Chunyang Yin, Bihu Lv, Chunfeng Zhang, William W Yu, Xiaoyong Wang, Yu Zhang, and Min Xiao. Superior optical properties of perovskite nanocrystals as single photon emitters. *ACS nano*, 9(12):12410–12416, 2015.
- [111] Son-Tung Ha, Rui Su, Jun Xing, Qing Zhang, and Qihua Xiong. Metal halide perovskite nanomaterials: synthesis and applications. *Chemical science*, 8(4):2522–2536, 2017.
- [112] Hendrik Utzat, Katherine E Shulenberger, Odin B Achorn, Michel Nasilowski, Timothy S Sinclair, and Mounqi G Bawendi. Probing linewidths and biexciton quantum yields of single cesium lead halide nanocrystals in solution. *Nano Letters*, 17(11):6838–6846, 2017.
- [113] Feng Zhang, Haizheng Zhong, Cheng Chen, Xian-gang Wu, Xiangmin Hu, Hailong Huang, Junbo Han, Bingsuo Zou, and Yuping Dong. Brightly luminescent and color-tunable colloidal $\text{CH}_3\text{NH}_3\text{PbX}_3$ ($x = \text{Br, I, Cl}$) quantum dots: potential alternatives for display technology. *ACS nano*, 9(4):4533–4542, 2015.
- [114] Jasmina A Sichert, Yu Tong, Niklas Mutz, Mathias Vollmer, Stefan Fischer, Karolina Z Milowska, Ramon García Cortadella, Bert Nickel, Carlos Cardenas-Daw, Jacek K Stolarczyk, et al. Quantum size effect in organometal halide perovskite nanoplatelets. *Nano letters*, 15(10):6521–6527, 2015.

- [115] Qiang Wang, Xiao-Dan Liu, Yun-Hang Qiu, Kai Chen, Li Zhou, and Qu-Quan Wang. Quantum confinement effect and exciton binding energy of layered perovskite nanoplatelets. *AIP Advances*, 8(2):025108, 2018.
- [116] Ziyi Wang, Sijian Yuan, Dahai Li, Feng Jin, Rongjun Zhang, Yiqiang Zhan, Ming Lu, Songyou Wang, Yuxiang Zheng, Junpeng Guo, et al. Influence of hydration water on ch₃nh₃pbi₃ perovskite films prepared through one-step procedure. *Optics Express*, 24(22):A1431–A1443, 2016.
- [117] Giles E Eperon, Erin Jedlicka, and David S Ginger. Biexciton auger recombination differs in hybrid and inorganic halide perovskite quantum dots. *The Journal of Physical Chemistry Letters*, 9(1):104–109, 2018.
- [118] Gautham Nair, Jing Zhao, and Mounqi G Bawendi. Biexciton quantum yield of single semiconductor nanocrystals from photon statistics. *Nano letters*, 11(3):1136–1140, 2011.
- [119] Chunyang Yin, Liyang Chen, Nan Song, Yan Lv, Fengrui Hu, Chun Sun, W Yu William, Chunfeng Zhang, Xiaoyong Wang, Yu Zhang, et al. Bright-exciton fine-structure splittings in single perovskite nanocrystals. *Physical Review Letters*, 119(2):026401, 2017.
- [120] Julien Ramade, Léon Marcel Andriambariarijaona, Violette Steinmetz, Nicolas Goubet, Laurent Legrand, Thierry Barisien, Frédéric Bernardot, Christophe Testelin, Emmanuel Lhuillier, Alberto Bramati, et al. Fine structure of excitons and electron–hole exchange energy in polymorphic cspbbr₃ single nanocrystals. *Nanoscale*, 10(14):6393–6401, 2018.
- [121] Xiaoming Li, Fei Cao, Dejian Yu, Jun Chen, Zhiguo Sun, Yalong Shen, Ying Zhu, Lin Wang, Yi Wei, Ye Wu, et al. All inorganic halide perovskites nanosystem: synthesis, structural features, optical properties and optoelectronic applications. *Small*, 13(9):1603996, 2017.
- [122] Muhammad Imran, Francesco Di Stasio, Zhiya Dang, Claudio Canale, Ali Hossein Khan, Javad Shamsi, Rosaria Brescia, Mirko Prato, and Liberato Manna. Colloidal synthesis of strongly fluorescent cspbbr₃ nanowires with width tunable down to the quantum confinement regime. *Chemistry of Materials*, 28(18):6450–6454, 2016.
- [123] Yehonadav Bekenstein, Brent A Koscher, Samuel W Eaton, Peidong Yang, and A Paul Alivisatos. Highly luminescent colloidal nanoplates of perovskite cesium lead halide and their oriented assemblies. *Journal of the American Chemical Society*, 137(51):16008–16011, 2015.
- [124] Quinten A Akkerman, Silvia Genaro Motti, Ajay Ram Srimath Kandada, Edoardo Mosconi, Valerio D’Innocenzo, Giovanni Bertoni, Sergio Marras, Brett A Kamino, Laura Miranda, Filippo De Angelis, et al. Solution synthesis approach to colloidal cesium lead halide perovskite nanoplatelets with monolayer-level thickness control. *Journal of the American Chemical Society*, 138(3):1010–1016, 2016.

- [125] Caixia Huo, Chee Fai Fong, Mohamed-Raouf Amara, Yuqing Huang, Bo Chen, Hua Zhang, Lingjun Guo, Hejun Li, Wei Huang, Carole Diederichs, et al. Optical spectroscopy of single colloidal CsPbBr_3 perovskite nanoplatelets. *Nano Letters*, 2020.
- [126] Javad Shamsi, Alexander S Urban, Muhammad Imran, Luca De Trizio, and Liberato Manna. Metal halide perovskite nanocrystals: synthesis, post-synthesis modifications, and their optical properties. *Chemical reviews*, 119(5):3296–3348, 2019.
- [127] Shibin Sun, Dan Yuan, Yuan Xu, Aifei Wang, and Zhengtao Deng. Ligand-mediated synthesis of shape-controlled cesium lead halide perovskite nanocrystals via reprecipitation process at room temperature. *ACS nano*, 10(3):3648–3657, 2016.
- [128] Qi Pan, Huicheng Hu, Yatao Zou, Min Chen, Linzhong Wu, Di Yang, Xiaolei Yuan, Jian Fan, Baoquan Sun, and Qiao Zhang. Microwave-assisted synthesis of high-quality “all-inorganic” CsPbX_3 ($x = \text{Cl}, \text{Br}, \text{I}$) perovskite nanocrystals and their application in light emitting diodes. *Journal of Materials Chemistry C*, 5(42):10947–10954, 2017.
- [129] Yu Tong, Eva Bladt, Meltem F Aygüler, Aurora Manzi, Karolina Z Milowska, Verena A Hintermayr, Pablo Docampo, Sara Bals, Alexander S Urban, Lakshminarayana Polavarapu, et al. Highly luminescent cesium lead halide perovskite nanocrystals with tunable composition and thickness by ultrasonication. *Angewandte Chemie International Edition*, 55(44):13887–13892, 2016.
- [130] Min Chen, Yatao Zou, Linzhong Wu, Qi Pan, Di Yang, Huicheng Hu, Yeshe Tan, Qixuan Zhong, Yong Xu, Haiyu Liu, et al. Solvothermal synthesis of high-quality all-inorganic cesium lead halide perovskite nanocrystals: from nanocube to ultrathin nanowire. *Advanced Functional Materials*, 27(23):1701121, 2017.
- [131] Aizhao Pan, Matthew Jurow, Yanrui Zhao, Fen Qiu, Ya Liu, Juan Yang, Jeffrey J Urban, Ling He, and Yi Liu. Templated self-assembly of one-dimensional CsPbX_3 perovskite nanocrystal superlattices. *Nanoscale*, 9(45):17688–17693, 2017.
- [132] Ting Zhao, Hongbin Liu, Mark E Ziffer, Adharsh Rajagopal, Lijian Zuo, David S Ginger, Xiaosong Li, and Alex KY Jen. Realization of a highly oriented MAPbBr_3 perovskite thin film via ion exchange for ultrahigh color purity green light emission. *ACS Energy Letters*, 3(7):1662–1669, 2018.
- [133] Di Yang, Muhan Cao, Qixuan Zhong, Pengli Li, Xiaohong Zhang, and Qiao Zhang. All-inorganic cesium lead halide perovskite nanocrystals: synthesis, surface engineering and applications. *Journal of Materials Chemistry C*, 7(4):757–789, 2019.
- [134] Nicholas Aristidou, Christopher Eames, Irene Sanchez-Molina, Xiangnan Bu, Jan Kosco, M Saiful Islam, and Saif A Haque. Fast oxygen diffusion and iodide defects mediate oxygen-induced degradation of perovskite solar cells. *Nature communications*, 8(1):1–10, 2017.

- [135] Caleb C Boyd, Rongrong Cheacharoen, Tomas Leijtens, and Michael D McGehee. Understanding degradation mechanisms and improving stability of perovskite photovoltaics. *Chemical reviews*, 119(5):3418–3451, 2018.
- [136] WE Moerner and David P Fromm. Methods of single-molecule fluorescence spectroscopy and microscopy. *Review of Scientific instruments*, 74(8):3597–3619, 2003.
- [137] James WM Chon, Xiaosong Gan, and Min Gu. Splitting of the focal spot of a high numerical-aperture objective in free space. *Applied physics letters*, 81(9):1576–1578, 2002.
- [138] M Totzeck. Numerical simulation of high-na quantitative polarization microscopy and corresponding near-fields. *Optik*, 112(9):399–406, 2001.
- [139] H Gordon Berry, G Gabrielse, and AE Livingston. Measurement of the stokes parameters of light. *Applied optics*, 16(12):3200–3205, 1977.
- [140] Beth Schaefer, Edward Collett, Robert Smyth, Daniel Barrett, and Beth Fraher. Measuring the stokes polarization parameters. *American Journal of Physics*, 75(2):163–168, 2007.
- [141] Shilpa N Raja, Yehonadav Bekenstein, Matthew A Koc, Stefan Fischer, Dandan Zhang, Liwei Lin, Robert O Ritchie, Peidong Yang, and A Paul Alivisatos. Encapsulation of perovskite nanocrystals into macroscale polymer matrices: enhanced stability and polarization. *ACS applied materials & interfaces*, 8(51):35523–35533, 2016.
- [142] Brent Fisher, Jean Michel Caruge, Don Zehnder, and Mounji Bawendi. Room-temperature ordered photon emission from multiexciton states in single cdse core-shell nanocrystals. *Physical review letters*, 94(8):087403, 2005.
- [143] Ferruccio Pisanello, Godefroy Leménager, Luigi Martiradonna, Luigi Carbone, Stefano Vezzoli, Pascal Desfonds, Pantaleo Davide Cozzoli, Jean-Pierre Hermier, Elisabeth Giacobino, Roberto Cingolani, et al. Non-blinking single-photon generation with anisotropic colloidal nanocrystals: towards room-temperature, efficient, colloidal quantum sources. *Advanced Materials*, 25(14):1974–1980, 2013.
- [144] Y-S Park, Anton V Malko, Javier Vela, Yongfen Chen, Yagnaseni Ghosh, Florencio García-Santamaría, Jennifer A Hollingsworth, Victor I Klimov, and Han Htoon. Near-unity quantum yields of biexciton emission from cdse/cds nanocrystals measured using single-particle spectroscopy. *Physical review letters*, 106(18):187401, 2011.
- [145] VI Klimov, JA McGuire, RD Schaller, and VI Rupasov. Scaling of multiexciton lifetimes in semiconductor nanocrystals. *Physical Review B*, 77(19):195324, 2008.
- [146] John A McGuire, Jin Joo, Jeffrey M Pietryga, Richard D Schaller, and Victor I Klimov. New aspects of carrier multiplication in semiconductor nanocrystals. *Accounts of chemical research*, 41(12):1810–1819, 2008.

- [147] Stefano Vezzoli, Seyedruhollah Shojaii, Simone Cialdi, Daniele Cipriani, Fabrizio Castelli, Matteo GA Paris, Luigi Carbone, P Davide Cozzoli, Elisabeth Giacobino, and Alberto Bramati. An ensemble-based method to assess the quality of a sample of nanocrystals as single photon emitters. *Optics Communications*, 300:215–219, 2013.
- [148] Jonathan De Roo, Maria Ibáñez, Pieter Geiregat, Georgian Nedelcu, Willem Walravens, Jorick Maes, Jose C Martins, Isabel Van Driessche, Maksym V Kovalenko, and Zeger Hens. Highly dynamic ligand binding and light absorption coefficient of cesium lead bromide perovskite nanocrystals. *ACS nano*, 10(2):2071–2081, 2016.
- [149] Yong Liu, Martin Siron, Dylan Lu, Jingjing Yang, Roberto Dos Reis, Fan Cui, Mengyu Gao, Minliang Lai, Jia Lin, Qiao Kong, et al. Self-assembly of two-dimensional perovskite nanosheet building blocks into ordered ruddlesden–popper perovskite phase. *Journal of the American Chemical Society*, 141(33):13028–13032, 2019.
- [150] He Huang, Maryna I Bodnarchuk, Stephen V Kershaw, Maksym V Kovalenko, and Andrey L Rogach. Lead halide perovskite nanocrystals in the research spotlight: Stability and defect tolerance. *ACS energy letters*, 2(9):2071–2083, 2017.
- [151] Gangcheng Yuan, Cameron Ritchie, Maria Ritter, Sean Murphy, Daniel E Gómez, and Paul Mulvaney. The degradation and blinking of single cs₂pb₂i₂ perovskite quantum dots. *The Journal of Physical Chemistry C*, 122(25):13407–13415, 2017.
- [152] Daniel E Gómez, Joel Van Embden, Paul Mulvaney, Mark J Fernée, and Halina Rubinsztein-Dunlop. Exciton- trion transitions in single cdse–cds core–shell nanocrystals. *ACS nano*, 3(8):2281–2287, 2009.
- [153] Amy A Cordones and Stephen R Leone. Mechanisms for charge trapping in single semiconductor nanocrystals probed by fluorescence blinking. *Chemical Society Reviews*, 42(8):3209–3221, 2013.
- [154] Pavel A Frantsuzov, Sándor Volkán-Kacsó, and Bolizsár Jankó. Model of fluorescence intermittency of single colloidal semiconductor quantum dots using multiple recombination centers. *Physical review letters*, 103(20):207402, 2009.
- [155] Christophe Galland, Yagnaseni Ghosh, Andrea Steinbrück, Milan Sykora, Jennifer A Hollingsworth, Victor I Klimov, and Han Htoon. Two types of luminescence blinking revealed by spectroelectrochemistry of single quantum dots. *Nature*, 479(7372):203–207, 2011.
- [156] Nicholas P Brawand, Márton Vörös, and Giulia Galli. Surface dangling bonds are a cause of b-type blinking in si nanoparticles. *Nanoscale*, 7(8):3737–3744, 2015.

- [157] Kai Zhang, Hauyee Chang, Aihua Fu, A Paul Alivisatos, and Haw Yang. Continuous distribution of emission states from single cdse/zns quantum dots. *Nano letters*, 6(4):843–847, 2006.
- [158] Brent R Fisher, Hans-Jürgen Eisler, Nathan E Stott, and Mounqi G Bawendi. Emission intensity dependence and single-exponential behavior in single colloidal quantum dot fluorescence lifetimes. *The Journal of Physical Chemistry B*, 108(1):143–148, 2004.
- [159] Sudipta Seth, Tasnim Ahmed, and Anunay Samanta. Photoluminescence flickering and blinking of single cspbbr3 perovskite nanocrystals: revealing explicit carrier recombination dynamics. *The journal of physical chemistry letters*, 9(24):7007–7014, 2018.
- [160] Cong Tai Trinh, Duong Nguyen Minh, Kwang Jun Ahn, Youngjong Kang, and Kwang-Geol Lee. Organic–inorganic fapbbr3 perovskite quantum dots as a quantum light source: Single-photon emission and blinking behaviors. *ACS Photonics*, 5(12):4937–4943, 2018.
- [161] Sudipta Seth, Navendu Mondal, Satyajit Patra, and Anunay Samanta. Fluorescence blinking and photoactivation of all-inorganic perovskite nanocrystals cspbbr3 and cspbbr2i. *The journal of physical chemistry letters*, 7(2):266–271, 2016.
- [162] Fengrui Hu, Zengle Cao, Chunfeng Zhang, Xiaoyong Wang, and Min Xiao. Defect-induced photoluminescence blinking of single epitaxial ingaas quantum dots. *Scientific reports*, 5:8898, 2015.
- [163] Dan Wang, Dan Wu, Di Dong, Wei Chen, Junjie Hao, Jing Qin, Bing Xu, Kai Wang, and Xiaowei Sun. Polarized emission from cspbbr3 perovskite quantum dots. *Nanoscale*, 8(22):11565–11570, 2016.
- [164] Dong Myung Jang, Kidong Park, Duk Hwan Kim, Jeunghee Park, Fazel Shojaei, Hong Seok Kang, Jae-Pyung Ahn, Jong Woon Lee, and Jae Kyu Song. Reversible halide exchange reaction of organometal trihalide perovskite colloidal nanocrystals for full-range band gap tuning. *Nano letters*, 15(8):5191–5199, 2015.
- [165] Rifat AM Hikmet, Patrick TK Chin, Dimitri V Talapin, and Horst Weller. Polarized-light-emitting quantum-rod diodes. *Advanced Materials*, 17(11):1436–1439, 2005.
- [166] Stefano Pierini, Maria d’Amato, M Joos, Quentin Glorieux, Elisabeth Giacobino, Emmanuel Lhuillier, Christophe Couteau, and Alberto Bramati. Hybrid device for quantum nanophotonics. *arXiv preprint arXiv:2001.10480*, 2020.
- [167] M Manceau, S Vezzoli, Q Glorieux, F Pisanello, E Giacobino, Luigi Carbone, M De Vittorio, and A Bramati. Effect of charging on cdse/cds dot-in-rods single-photon emission. *Physical Review B*, 90(3):035311, 2014.

- [168] Stefano Pierini, Marianna D’Amato, Mayank Goyal, Quentin Glorieux, Elisabeth Giacobino, Emmanuel Lhuillier, Christophe Couteau, and Alberto Bramati. Highly photostable perovskite nanocubes: Toward integrated single photon sources based on tapered nanofibers. *ACS Photonics*, 7(8):2265–2272, 2020.
- [169] Pablo Solano, Jeffrey A Grover, Jonathan E Hoffman, Sylvain Ravets, Fredrik K Fatemi, Luis A Orozco, and Steven L Rolston. Optical nanofibers: a new platform for quantum optics. In *Advances In Atomic, Molecular, and Optical Physics*, volume 66, pages 439–505. Elsevier, 2017.
- [170] Gilberto Brambilla. Optical fibre nanowires and microwires: a review. *Journal of Optics*, 12(4):043001, 2010.
- [171] E Vetsch, D Reitz, G Sagué, R Schmidt, ST Dawkins, and A Rauschenbeutel. Optical interface created by laser-cooled atoms trapped in the evanescent field surrounding an optical nanofiber. *Physical review letters*, 104(20):203603, 2010.
- [172] JE Hoffman, S Ravets, JA Grover, P Solano, PR Kordell, JD Wong-Campos, LA Orozco, and SL Rolston. Ultrahigh transmission optical nanofibers. *AIP advances*, 4(6):067124, 2014.
- [173] Gershon Kurizki, Patrice Bertet, Yuimaru Kubo, Klaus Mølmer, David Petrosyan, Peter Rabl, and Jörg Schmiedmayer. Quantum technologies with hybrid systems. *Proceedings of the National Academy of Sciences*, 112(13):3866–3873, 2015.
- [174] Ze-Liang Xiang, Sahel Ashhab, JQ You, and Franco Nori. Hybrid quantum circuits: Superconducting circuits interacting with other quantum systems. *Reviews of Modern Physics*, 85(2):623, 2013.
- [175] Bahaa EA Saleh and Malvin Carl Teich. *Fundamentals of photonics*. John Wiley & sons, 2019.
- [176] Allan W Snyder and John Love. *Optical waveguide theory*. Springer Science & Business Media, 2012.
- [177] Maxime Joos. Dispositifs hybrides: nanoparticules couplées à une nanofibre optique. pdh thesis. 2018.
- [178] Detlef Gloge. Weakly guiding fibers. *Applied optics*, 10(10):2252–2258, 1971.
- [179] Jonathan Hoffman. *Optical nanofiber fabrication and analysis towards coupling atoms to superconducting qubits*. PhD thesis, University of Maryland, College Park, 2014.
- [180] Baptiste Gouraud. Optical nanofibers interfacing cold atoms a tool for quantum optics. pdh thesis. 2016.
- [181] Fam Le Kien, JQ Liang, K Hakuta, and VI Balykin. Field intensity distributions and polarization orientations in a vacuum-clad subwavelength-diameter optical fiber. *Optics Communications*, 242(4-6):445–455, 2004.

- [182] Kali P Nayak and K Hakuta. Single atoms on an optical nanofibre. *New Journal of Physics*, 10(5):053003, 2008.
- [183] KP Nayak, PN Melentiev, M Morinaga, Fam Le Kien, VI Balykin, and K Hakuta. Optical nanofiber as an efficient tool for manipulating and probing atomic fluorescence. *Optics express*, 15(9):5431–5438, 2007.
- [184] Jonathan E Hoffman, Sylvain Ravets, Pablo A Solano, Peter R Kordell, Luis A Orozco, and Steven L Rolston. Pulling algorithm and simulation. 2014.
- [185] Gilberto Brambilla, Vittoria Finazzi, and David J Richardson. Ultra-low-loss optical fiber nanotapers. *Optics express*, 12(10):2258–2263, 2004.
- [186] Stefano Vezzoli, Mathieu Manceau, Godefroy Leménager, Quentin Glorieux, Elisabeth Giacobino, Luigi Carbone, Massimo De Vittorio, and Alberto Bramati. Exciton fine structure of cdse/cds nanocrystals determined by polarization microscopy at room temperature. *ACS nano*, 9(8):7992–8003, 2015.
- [187] Wei Geng, Mathieu Manceau, Nancy Rahbany, Vincent Sallet, Massimo De Vittorio, Luigi Carbone, Quentin Glorieux, Alberto Bramati, and Christophe Couteau. Localised excitation of a single photon source by a nanowaveguide. *Scientific reports*, 6:19721, 2016.
- [188] S Removille, R Dubessy, B Dubost, Q Glorieux, T Coudreau, S Guibal, JP Likforman, and L Guidoni. Trapping and cooling of sr+ ions: strings and large clouds. *Journal of Physics B: Atomic, Molecular and Optical Physics*, 42:154014, 2009.
- [189] Imad H Agha, Christina Giarmatzi, Quentin Glorieux, Thomas Coudreau, Philippe Grangier, and Gaétan Messin. Time-resolved detection of relative-intensity squeezed nanosecond pulses in an 87rb vapor. *New Journal of Physics*, 13:043030, 2011.
- [190] Mathieu Manceau, Stefano Vezzoli, Quentin Glorieux, Elisabeth Giacobino, Luigi Carbone, Massimo De Vittorio, J-P Hermier, and Alberto Bramati. Cdse/cds dot-in-rods nanocrystals fast blinking dynamics. *ChemPhysChem*, 19(23):3288–3295, 2018.
- [191] Ivens Saber, Rajiv Boddeda, Fabrice Raineri, Dorian Sanchez, Gregoire Beaudoin, Isabelle Sagnes, Quentin Glorieux, Alberto Bramati, Juan Ariel Levenson, and Kamel Bencheikh. Photonic crystal nanobeam cavities with optical resonances around 800 nm. *JOSA B*, 36(7):1823–1828, 2019.
- [192] Maxime Joos, Alberto Bramati, and Quentin Glorieux. Complete polarization control for a nanofiber waveguide using the scattering properties. *Optics express*, 27(13):18818–18830, 2019.
- [193] Chengjie Ding, Vivien Loo, Simon Pigeon, Maxime Joos, E Wu, Elisabeth Giacobino, Alberto Bramati, and Quentin Glorieux. Fabrication and characterization of optical nanofiber interferometer and resonator for the visible range. *New Journal of Physics*, 2019.

-
- [194] Rajiv Boddeda, Quentin Glorieux, Alberto Bramati, and Simon Pigeon. Generating strong anti-bunching by interfering nonclassical and classical states of light. *Journal of Physics B: Atomic, Molecular and Optical Physics*, 52(21):215401, 2019.
- [195] Stefano Pierini, Mackrine Nahra, Maxime Joos, Muhammad H Muhammad, Viatcheslav Agafonov, Emmanuel Lhuillier, Fabien Geoffray, Valery Davydov, Quentin Glorieux, Elisabeth Giacobino, et al. Nanophotonic approaches for integrated quantum photonics. *arXiv preprint arXiv:1909.10343*, 2019.
- [196] Emmanuel Lhuillier, Quentin Glorieux, Marianna D'Amato, Alberto Bramati, Christophe Couteau, Stefano Pierini, Elisabeth Giacobino, and MAYANK GOYAL. Highly photostable perovskite nanocubes: Toward integrated single photon sources based on tapered nanofibers. 2020.